Measuring amplitude and phase in optical fields with sub-wavelength features

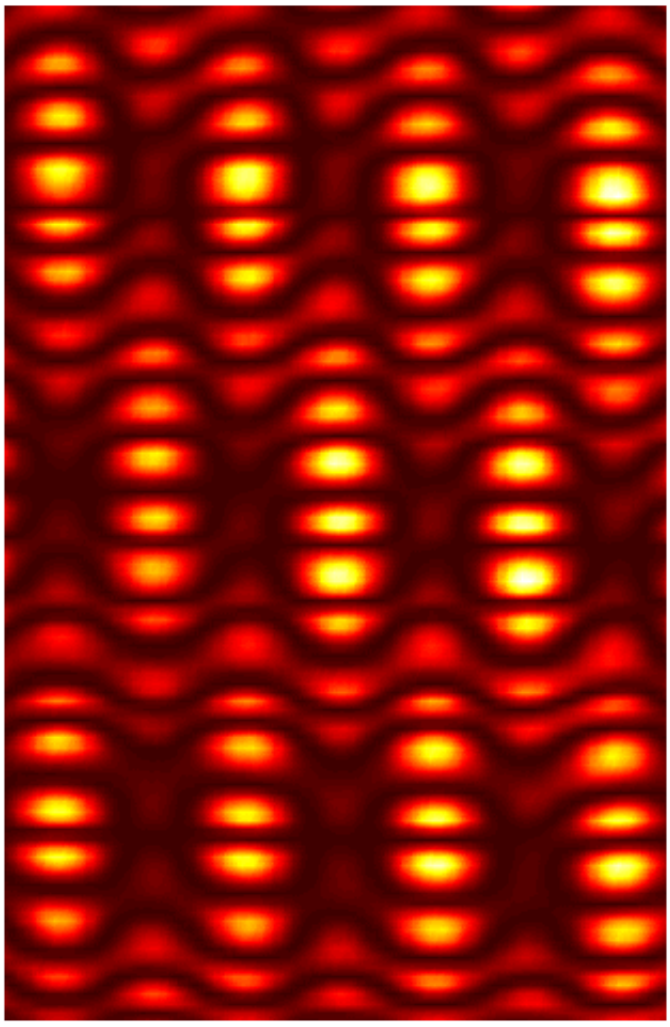

Antonello Nesci

Université de Neuchâtel

Institut de Microtechnique

Measuring amplitude and phase in optical fields with sub-wavelength features

Thèse

Présentée à la Faculté des sciences

pour obtenir le grade de docteur ès sciences

par

Nesci Antonello

Neuchâtel, Novembre 2001

IMPRIMATUR POUR LA THESE

Measuring amplitude and phase in optical fields with subwavelength structures

de M. Antonello Nesci

UNIVERSITE DE NEUCHATEL

FACULTE DES SCIENCES

La Faculté des sciences de l'Université de Neuchâtel sur le rapport des membres du jury,

MM. R. Dändliker (directeur de thèse), H.P. Herzig,
D. Courjon (Besançon) et
N. van Hulst (Entschede NL)

autorise l'impression de la présente thèse.

Neuchâtel, le 20 novembre 2001

Le doyen:

Abstract

In this thesis we present experimental and theoretical studies of optical fields with sub-wavelength features. We intend to gain a better understanding of the interaction of light with microstructures in order to determine their optical properties. An electromagnetic field is characterized by an amplitude, a phase and a polarization state. Therefore, experimental studies require coherent detection methods, in particular heterodyne scanning probe microscope (heterodyne SNOM), which allow the measurement of amplitude and phase of the optical field with sub-wavelength resolution. We discuss some basic properties of phase distributions. Light waves diffracted by microstructures can give birth to phase dislocations, also called phase singularities. Phase singularities are isolated points where the amplitude of the field is zero. Phase dislocations can be observed in the near- and far-field of optical microstructures, such as gratings. The behavior of phase singularities have been localized with a spatial resolution of 10 nm. Comparison of the calculated and measured amplitude and phase for the *TE*- and *TM*-mode with the heterodyne SNOM gives interesting information about the field conversion by the fiber tip probe. A non-trivial conclusion points out that the three vectorial components of the electric field are detected.

Résumé

Dans cette thèse, nous présentons des études expérimentales et théoriques de champs optiques ayant des propriétés sub-longueur d'onde. Notre intérêt se base sur une meilleure compréhension de l'interaction de la lumière avec des microstructures afin de déterminer leurs propriétés optiques. Un champ électromagnétique est caractérisé par une amplitude, une phase et un état de polarisation. Cependant, des études expérimentales requièrent une méthode de détection cohérente, en particulier un microscope hétérodyne optique à balayage en champ proche ("SNOM" hétérodyne) permettant la mesure de l'amplitude et de la phase de champ optiques avec une résolution nanométrique. Nous discutons également des propriétés de base des distributions de phase. En effet, la lumière diffractée par des microstructures peuvent donner naissance à des dislocations de phase, appelées aussi singularités de phase. Les singularités de phase sont des points isolés où l'amplitude est zéro. Ces points peuvent être observés dans le champ proche ou lointain de microstructures, comme des réseaux optiques par exemple. Les singularités de phase ont été localisées avec une résolution spatiale de 10 nm. Une comparaison théorique de l'amplitude et de la phase mesurée en mode *TE* et *TM* avec un SNOM hétérodyne donne des informations intéressantes sur la conversion du champ par un sonde locale en fibre optique. Une conclusion non triviale affirme que les trois composantes vectorielles du champ électrique sont détectées.

Table of contents

1 Introduction

Humans always have dreamt of pushing the limits of their visual perception. They have always been interested in the infinitely big or infinitely small. In the history of science, the invention of the first optical microscopes and telescopes marked the beginning of a new area. The novel instrumentation enabled the observation of phenomena not directly accessible to human senses. A lot of devices have been developed for this purpose. Telescopes allow observation far away while microscopes have been realized in order to see smaller matter. In 1590, magnification of images began to expand visual perception, due to the invention of lens systems. Although optical microscopes are, and have been, crucial in science, their limitations have been rapidly reached because technological progress always required more powerful devices.

1.1 Classical diffraction limit

In a conventional optical microscope, white light is concentrated onto the sample. The object is then imaged and magnified by a lens system. The image is a low pass filtered representation of the original object. The high spatial frequencies are lost during propagation through the objective. Hence, there is always a loss of information during propagation from near- to far-field and only structures with lateral dimensions larger than [1]

$$p_{\min} \approx \frac{\lambda}{2n\sin\theta} \tag{1.1}$$

can be imaged with accuracy. This limit is the smallest resolvable spacing, known as *Abbe's barrier* or *far-field diffraction limit*. It is a function of the wavelength of the probe radiation λ and the aperture angle θ collecting the light with respect to the object normal. If the system is in a medium different than air (e.g. a liquid), the refraction index of the medium n between the object and the objective is considered. According to Abbe's treatment, the limit of resolution for a conventional microscope is only slightly smaller than the wavelength of the probe radiation. In

order to gain sub-wavelength resolution, the optical system has to detect frequencies higher than $f > 1/\lambda$. This information, contained in high spatial frequencies f, is given by evanescent waves, which are non-propagating waves [2].

1.2 Scanning Near-field Optical Microscopy (SNOM)

In order to get sub-wavelength resolution in optical fields, it is crucial to probe high spatial frequencies contained in evanescent waves. To access the evanescent waves, a probe has to be brought close to the surface. "Close" or "near" means smaller than a wavelength (in contrast to "far") because this is the distance where evanescent waves extend. The definition of near-field optics (NFO) can be the following [1]: *"near-field optics is a branch of optics that considers configurations that depend on the passage of light to, from, through, or near an element with sub-wavelength features and the coupling of that light to a second element located a sub-wavelength distance from the first"*.

The idea to bring a probe close to the surface comes from the invention of the scanning tunneling microscope (STM) in the 1980's by G. Binnig and H. Roher [3] and then later, from the atomic force microscope (ATM) [4]. In the former, the Coulombian interaction is used to control the nanometric distance between the probe and the surface, whereas in the latter, van der Waals forces contribute to the approach. Such microscopes allow only topographical knowledge of sample surfaces. Progress in optics science requires the study of optical properties of objects. Thanks to scanning probe techniques (SPM), scanning near-field optical microscopy (SNOM) [5] allowed the diffraction barrier to be broken in optical microscopy. In 1982, first reports of near-field imaging at visible wavelengths came from the Zürich IBM laboratory where the STM was developed [6, 7].

The SNOM uses AFM techniques for the approach of a probe close to a surface of a sample in order to investigate the optical near-field. The SNOM probe, which detects the light (and/or illuminates the sample) has been the subject of a lot of technological effort. It is a crucial part of the SNOM because it is the principal sensor of the detection or the main source for the illumination. Its design can range from a tapered optical fiber to a silicon/quartz micro-machined tip mounted on an AFM cantilever. A metal coating can be deposited at the apex in order to better define a small aperture. In this work, we will use pulled dielectric and entirely metal coated fiber probes (chapter 3).

Many different configurations (Fig. 1.1) of optical near-field microscopes have been proposed over the last twenty years [8]. The denomination "SNOM" groups all these techniques, which have their own characteristic names. In collection mode (Fig. 1.1a), monochromatic light is collected through the probe while the sample is illuminated in far-field (in opposition to near-

field definition). In illumination mode (Fig. 1.1b), the sample is illuminated with light from the probe apex and collected in the far-field. In illumination/collection SNOM mode (Fig. 1.1c), the sample is illuminated by the light coming from the probe and the light emanating from the sample is collected equally by the probe. In oblique illumination mode (Fig. 1.1d), the sample is illuminated obliquely with a far-field device and the light is collected by the tip. In the opposite case, oblique collection (Fig. 1.1e), the light goes through the aperture of the probe, illuminating the sample. The light is collected obliquely with a far-field device. In dark-field SNOM (Fig. 1.1f), also called photon scanning tunneling microscopy (PSTM), the sample is illuminated by total internal reflection. The fiber probe (not necessarily coated), is placed in the near-field of the sample, collects the light via the tunneling effect of the light (chapter 4). In this work, the configurations of Figs. 1.1a and 1.1.f have been used.

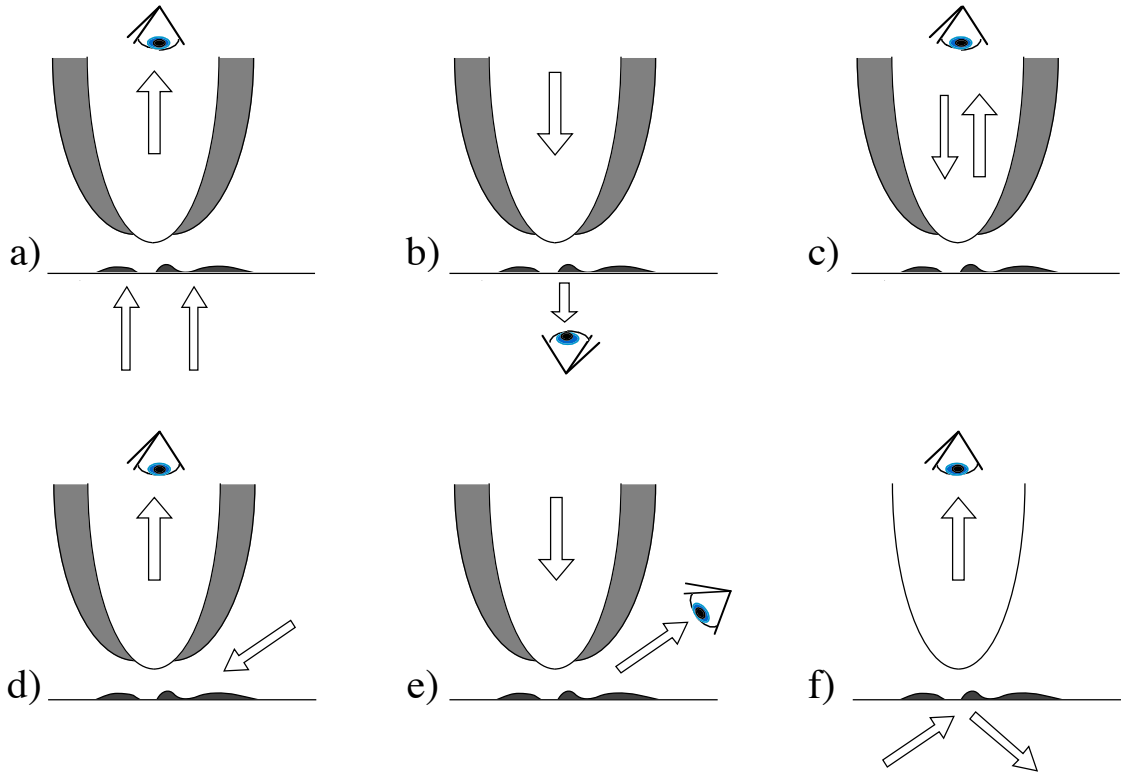

***Figure 1.1**: Scheme of different SNOM configurations [1]. The specific configurations are called **a)** collection-, **b)** illumination-, **c)** collection/illumination-, **d)** oblique illumination-, **e)** oblique collection- and **f)** dark field-mode.*

The SNOM became an important tool for many research domains in Optics, Micro-Optics and then for Nano-Optics. The development of the SNOM gives birth to large number of applications in biology, material science, surface chemistry and information storage, for instance. SNOM application in telecommunication optics is also required for fabrication of new devices.

1.3 Motivation and thesis outline

The goals of this work are several. The first is the contribution to the understanding of optical fields. In scanning near-field optical microscopy, the field generated by an object, especially by sub-wavelength objects, is different from the object itself. In general, rigorous diffraction theory is needed to estimate the geometrical parameters of the object under investigation. To characterize exactly an electromagnetic field, intensity alone is not sufficient; one has to know its amplitude, its phase and its polarization state. The main task in this work was to build a set-up in order to be able to measure the amplitude and the phase of optical fields with sub-wavelength resolution. We are positively convinced that in the future, optical amplitude and phase measurement can bring many solutions in micro- and nano-fabrication, e.g. in photonic bandgap structures for optical telecommunication devices.

The second aim is to better understand the SNOM itself. What is possible to measure with such an instrument and what does the tip really detect? This is a crucial question. In fact, one must be careful about tip-field interaction in order to avoid artifacts. We will present a few basic measurements in order to answer to these fundamental questions and also to know the limitation of our novel device.

This thesis is structured in five main chapters. ***Chapter 2*** introduces the basic concept of heterodyne detection. Photodetectors are sensitive to photon flux (i.e. intensity) only and therefore not to the optical phase. However, heterodyne detection offers an elegant way to measure the complex amplitude of an optical signal. This chapter will give the theoretical basis on which amplitude and phase measurements have been measured with high accuracy. Some theoretical noise aspects will be introduced in order to know the limitation of this interferometric method.

In ***chapter 3***, we will present a detailed description of the complete optical heterodyne probe system. We will show how a heterodyne interferometer has been combined with a scanning probe optical microscope in order to measure amplitude and phase of optical near- and far-fields. A complete description of all the components and devices will be given. The entire set-up this work has been built within the framework of a project supported by the *Swiss National Science Foundation*. The signal to noise ratio of the system will be presented so as to establish correctly the basis of the optical detection for all further measurements. As a first test, we shall study the amplitude and the phase of an optical plane wave.

Chapter 4 is a fundamental part of this work. In fact, we will study an important optical wave: the evanescent wave. Photon Scanning Tunneling Microscopy is essentially based on evanescent fields. Indeed, the finite extension of about one wavelength from the investigating surface, gives the establishment of this important device. Frustration of the evanescent field explains why and how the diffraction limit of a conventional optical microscope can be

surpassed. 2-D measurements of an evanescent wave will be shown, revealing interesting phenomena in the near-field region, such as optical scattering from surface defects or dust.

After plane wave and evanescent wave detection, another test will be a source of interest: the evanescent standing wave, presented in ***chapter 5***. In fact, the interference of two evanescent waves, with opposite directions, allows our instrument to be characterized. Evanescent standing waves are a useful test "structure" because no topographical defect perturbs the detection. Amplitude and phase measurement of the sinusoidal modulation of the field enables investigation of the possible limitations of the device. Optical phase changes with a resolution of 1.6 nm will be presented.

In ***chapter 6***, the main interest of this work is reported. In fact, one important goal of this project was the understanding of the interaction of light with microstructures. Even if the structures range in micrometric scale (with structure features $\Lambda > \lambda$), the diffracted fields have sub-wavelength features. In fact, sub-wavelength resolution measurements of the amplitude and phase of the optical fields generated by a micrometer pitch grating will be shown in this chapter. We will especially pay attention to the phase distribution behind the grating. Indeed, the interaction of light with microstructures gives birth to phase singularities. These special point phase defects, where the intensity vanishes, are a lake of interest. In fact, their position in space can give information on the original structure. The position of phase singularities has been measured with high resolution, even in the far-field, within 10 nm. In this chapter, we will also contribute to the knowledge of the field conversion into an optical fiber probe. This domain is still not well established and is often a source of confusion. In fact, the understanding of this phenomenon will bring us to a better knowledge of image interpretation, preventing from possible artifacts in the measurements.

2 Optical heterodyne detection

Since the development of the first lasers in the 1960's [9], laser interferometry has become an important technique to provide high accuracy measurement systems for scientific and industrial applications. One crucial issue for interferometry is related to the electronic treatment and analysis of the signal. In fact, the measurement accuracy depends mainly on the signal processing (hardware and software) employed to get the phase information from the interference signal. Interferometric measurement techniques can be placed into two categories: static and dynamic methods [10]. Static techniques, or homodyne, work only with one optical frequency for the interfering beams. Dynamic techniques are based on phase shifting (with two or more frequencies) between the interfering waves.

Photodetectors are only sensitive to the energy (photon flux) and therefore not to the optical phase. However, it is possible to measure the complex amplitude (real amplitude and phase) of an optical signal by mixing it with a coherent reference wave of stable phase, and by detecting the superposition with a photodetector. By shifting the frequency of the interfering waves, we get a so called optical heterodyne detection. This technique belongs to the category of dynamic interferometry.

2.1 Principle

The concept of optical heterodyne detection is to introduce a small frequency shift Δf between two interfering waves [11]. As a result of this shift, the interference of the two waves produces an intensity modulation at the beat frequency, $\Delta f = f_1 - f_2$, which is then detected. A typical set-up for heterodyne detection is shown in Fig. 2.1. After separation of the laser light (of frequency ν) by a beam splitter (BS), the frequency of object wave O and reference wave R is shifted by the use of two acousto-optic modulators (AOM1 and AOM2), driven at f_1 and f_2, respectively. The two modulators can also be placed in the same arm (serial) of the interferometer. In both

cases, the resulting interference is exactly the same. The heterodyne frequency can be modified by changing the operating frequency of the acousto-optic modulator driver.

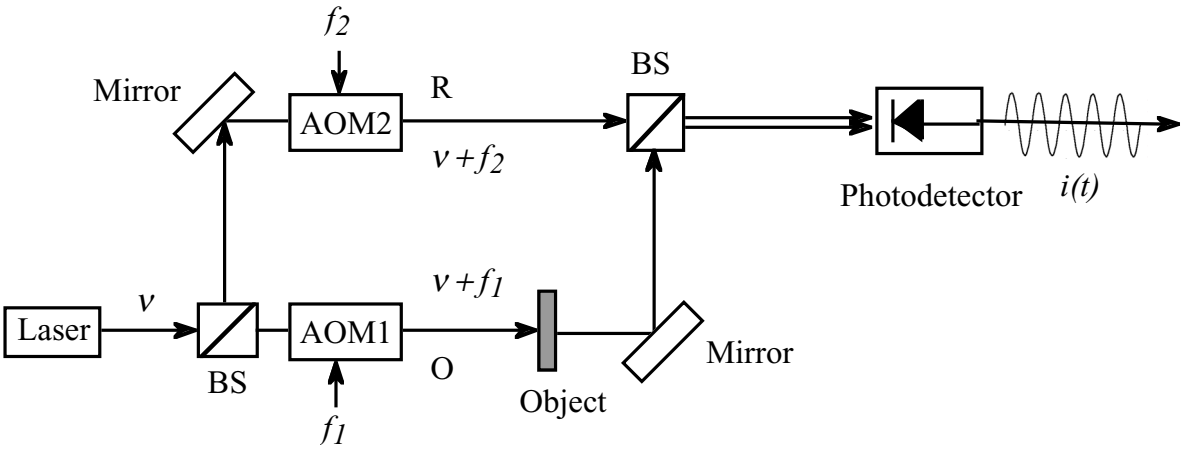

***Figure 2.1**: Heterodyne interferometer set-up.*

The interference of the two monochromatic waves R and O produces a beat signal at Δf, which is then detected by a photodetector. The resulting interference contains the information about both the amplitude and the phase of the optical field.

The object and reference waves can be described by the complex signals

$$V_o = \mathrm{Re}\left\{\hat{A}_o \cdot \exp\left(i2\pi(\nu + f_1)t\right)\right\} \tag{2.1}$$

$$\text{and}\, V_r = \mathrm{Re}\left\{\hat{A}_r \cdot \exp\left(i2\pi(\nu + f_2)t\right)\right\}, \tag{2.2}$$

with the complex amplitudes

$$\hat{A}_o = A_o \exp(i\varphi_o) \tag{2.3}$$

$$\text{and}\ \hat{A}_r = A_r \exp(i\varphi_r). \tag{2.4}$$

The total complex signal of the interference is given by $V = V_o + V_r$. The total intensity then becomes

$$I = |V|^2 = A_o^2 + A_r^2 + 2A_oA_r \cos\left[2\pi(f_1 - f_2)t + (\varphi_o - \varphi_r)\right]. \tag{2.5}$$

After introducing $I_o = A_o^2$, $I_r = A_r^2$, $\Delta f = f_1 - f_2$ and $\varphi = \varphi_o - \varphi_r$, the intensity becomes

$$I = I_o + I_r + 2\sqrt{I_oI_r}\cos\left[2\pi\Delta ft + \varphi\right]. \tag{2.6}$$

The interference between the reference wave R and the object wave O produces a sinusoidal intensity modulation at the beat frequency Δf with the amplitude $A_o A_r$ and the dc level $I_o + I_r$. The information of the object is given by the amplitude and the relative phase φ_o at the beat frequency Δf and can be measured electronically by comparing it with a reference signal at the same frequency.

2.2 Noise in photodetection

The noise of detection is mainly generated in the photodetector. The photodetector is composed of a photodiode and an electronic circuit. Several sources of noise are present in the process of photodetection, but the most significant are Johnson noise (or thermal noise) and shot noise.

2.2.1 Johnson noise

The photodetector circuit is shown in Fig. 2.2. A photodiode PD converts the incoming photons (with energy $h\nu$) into photoelectrons which are then collected in a capacitor *C* of the photodiode. A resistor R_0 is introduced into the circuit (Fig. 2.2) in order to get a current *i*. The RC circuit (electronic filter) introduces a limited bandwidth *B* for the detection. The photodiode is supplied by a bias *U* and the output voltage produced by the incoming light is U_{out}.

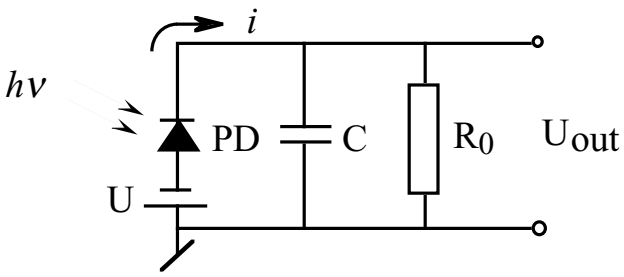

***Figure 2.2**: Detector circuit consisting of a photodiode PD (with a bias voltage U), a capacitor C and a resistor R_0. The output voltage is U_{out}.*

Johnson noise (or thermal noise) is caused by the statistical behavior of the electrons (fluctuations produced by thermal motion) in the electronic circuit. It is independent of the detected optical power. The electrical power of the thermal noise at the output of the detector is given by [12-14]

$$P_{TN} = 4kTB, \tag{2.7}$$

where $k = 1.38 \cdot 10^{-23}$ J/K is the Boltzmann constant and T is the absolute temperature (in Kelvin).

2.2.2 Shot noise

Shot noise, or quantum noise, is a fundamental limit of the nature of light and is characterized by the fluctuation of the photons arriving at the detector. The resulting photoelectrons, produced by the conversion of photons (with an energy $h\nu$) into electrons, can be described by Poisson's statistics [15]. The variance of the shot noise is therefore equal to the mean number n_e of the collected photoelectrons during a characteristic time interval, called integration time $\tau = 1/(2B)$, where B is the detection bandwidth [15]. The ratio of the number of photoelectrons n_e created to the number of incoming photons n_p is called the *quantum efficiency* $\eta = n_e/n_p$ ($\eta_{\max} = 1$). The ratio of the current i (proportional to the photoelectrons produced per unit time) and the optical power P_{opt} gives the *spectral sensitivity*

$$S = \frac{i}{P_{opt}} = \frac{\eta e}{h\nu}, \tag{2.8}$$

where $e = 1.602 \cdot 10^{-19}$ As is the electron charge, $h = 6.626 \cdot 10^{-34}$ Js Planck's constant and ν is the light frequency. The variance $\langle i_{SN}^2 \rangle$ of the shot noise current is given by the number of electrons n_e generated in the photodiode and the bandwidth B through $\langle i_{SN}^2 \rangle = 2eBn_e$. These electrons are produced by the conversion of photons and by the dark-current i_d, which is the remaining current when the photodetector is not exposed to light (in the dark). It contributes to the fluctuations of the detected number of electrons, and thus to the shot noise current. Considering the photodetector circuit of Fig. 2.2, the electric power corresponding to the shot noise, for frequencies within the detection bandwidth B, is [12]

$$P_{SN} = \langle i_{SN}^2 \rangle R_0 = 2eB(SP_{tot} + i_d)R_0, \tag{2.9}$$

where $P_{tot} = P_r + P_o$ is the sum of the reference and the object power. Therefore, if the reference power is large, the photocurrent SP_{opt} dominates the dark current i_d. In this case, the electrical power corresponding to the shot noise at the output detector becomes

$$P_{SN} = 2eBSP_{tot}R_0. \tag{2.10}$$

2.3 Signal to noise ratio of the heterodyne detection

The *signal to noise ratio* (SNR) of the heterodyne signal is defined by the ratio of the heterodyne signal power (ac power) to the total noise power. From Eq. (2.6), we get for the optical power seen by the photodiode

$$P(t) = P_o + P_r + 2\sqrt{P_o P_r}\cos(2\pi\Delta f t + \varphi), \tag{2.11}$$

where P_o is the optical power of the object and P_r the optical power of the reference. This equation expresses the signal produced in the ideal case. In reality, the amplitude of the signal is reduced by a factor *m*, called the *relative interference amplitude*. The factor *m* ($0 \le m \le 1$) is a characteristic of the interference quality, i.e. temporal and spatial coherence, polarization and wave superposition. The optical power of the interference is therefore given by

$$P(t) = P_{tot} + 2m\sqrt{P_o P_r}\cos(2\pi\Delta f t + \varphi), \tag{2.12}$$

and the resulting output current *i(t)* of the photodiode becomes

$$i(t) = S\left[P_{tot} + 2m\sqrt{P_0 P_r}\cos(2\pi\Delta f t + \varphi)\right] = i_{dc} + i_{ac}\cos(2\pi\Delta f t + \varphi), \tag{2.13}$$

where $i_{dc} = SP_{tot}$ is the dc current and $i_{ac} = 2mS\sqrt{P_o P_r}$ is the amplitude of the ac current $i_{AC}(t) = i_{ac}\cos(2\pi\Delta f t + \varphi)$. The electrical power of the heterodyne signal is found to be

$$P_{AC} = \left\langle i_{AC}^2 \right\rangle R_0 = \frac{1}{2} i_{ac}^2 R_0 = 2m^2 S^2 P_o P_r R_0. \tag{2.14}$$

According to the definition, we get for the electronic signal to noise ratio

$$\text{SNR} = \frac{\left\langle i_{AC}^2 \right\rangle}{\left\langle i_N^2 \right\rangle} = \frac{P_{AC}}{P_{SN} + P_{TN}}. \tag{2.15}$$

Heterodyne detection offers an elegant way to increase the electronic signal for a given object power P_o (or more precisely the signal to noise ratio) up to a point where shot noise dominates Johnson noise. In this case, we have *shot noise limited detection*. To get P_{SN} larger than P_{TN} (and thus to be shot noise limited), the power of P_{tot} has to be enhanced by increasing the reference power P_r for fixed P_o.

To make sure of being limited by shot noise only, the reference power has to be larger than the minimum reference optical power $P_r^{\min}$. This lower limit is derived from Eqs. (2.7) and (2.10). In fact, for $P_{SN}^{\min} = P_{TN}$ and assuming that $P_r >> P_o$, we get

$$P_r^{\min} = \frac{2kT}{eR_0S}. \tag{2.16}$$

By increasing P_r so that $P_r > P_r^{\min}$, $P_{SN} >> P_{TN}$ and the SNR reaches a constant value of

$$\text{SNR} = \frac{P_{AC}}{P_{SN}} = m^2\left(\frac{\eta}{h\nu B}\right)\left(\frac{P_oP_r}{P_o+P_r}\right). \tag{2.17}$$

Assuming that $m = 1$ (ideal case) and $P_r >> P_o$ (which is always possible), the signal to noise ratio is given by the relation

$$\text{SNR} = \frac{\eta}{h\nu B}P_o. \tag{2.18}$$

Let us introduce n_e^o, the number of photoelectrons and n_p^o the number of photons corresponding to the power P_o. The number of photons received during the integration time $\tau = 1/(2B)$ is $n_p^o = \tau P_o/h\nu$ and Eq. (2.18) can be expressed by

$$\text{SNR} = \frac{2\tau\eta}{h\nu}P_o = 2n_e^o. \tag{2.19}$$

This equation demonstrates that the signal to noise ratio is only limited by the shot noise of the object power P_o. The factor of 2 with respect to direct detection is known as *heterodyne gain*. To get the best SNR, η has to be as large as possible ($\eta_{\max} = 1$). This is the main reason why we use a standard silicon photodiode (PD) rather than a photomultiplier (PM). The quantum efficiency of a PD is larger than that of a PM ($\eta_{Si} \approx 70\%$, $\eta_{PM} \approx 10\%$).

The bandwidth B considered so far is the bandwidth of the photodetector circuit. However, after the detection, the bandwidth can be decreased by means of the integration time of a spectrum analyzer or a lock-in amplifier. It is this post-detection bandwidth which is relevant for the final SNR of the measurement. An example of measured SNR from an optical heterodyne system with a spectrum analyzer for B = 62.5 Hz will be presented in section 3.3.

The accuracy of the amplitude and phase of the optical field can be expressed via the measured SNR. From Eq. (2.15), the amplitude $A = 2m\sqrt{P_oP_r} \propto \sqrt{P_o}$ of the heterodyne signal, which is proportional to the amplitude of the optical field under investigation, is proportional to the square root of the SNR. Thus, the relative standard deviation of the amplitude is given by

$$\frac{\delta A}{A} = \sqrt{\frac{\langle i_N^2\rangle}{\langle i_{AC}^2\rangle}} = \frac{1}{\sqrt{SNR}} \tag{2.20}$$

and the accuracy of the phase measurement by [16]

$$\delta\varphi = \frac{1}{\sqrt{SNR}}. \tag{2.21}$$

For example, in case of shot noise limited detection, for an object power P_o = 1 pW, a bandwidth B = 62.5 Hz, a quantum efficiency η = 70% and a wavelength of $\lambda = 532$ nm, we get from Eq. (2.19) $n_e^o = 15'000$ and a SNR of about 45 dB (Eq. (2.18)). The accuracy for the measured amplitude is then $\delta A/A = 6 \cdot 10^{-3}$ and for the measured phase $\delta\varphi = 6$ mrad ($\cong 2\pi/10^3$ or 0.33°).

It is interesting to know the limit of the optical heterodyne detection. Theoretically, the lower limit of detection is given by SNR = 1 for the heterodyne signal. Following Eq. (2.19) this corresponds to one half photoelectron ($n_e^o = 1/2$) contributed by the object power P_o. Then, the minimum detectable optical power becomes

$$P_o^{\min} = \frac{h\nu B}{\eta}. \tag{2.22}$$

With the previous values B = 62.5 Hz, η = 0.7, λ = 532 nm, the minimum detectable optical power with heterodyne detection is found to be $P_o^{\min} = 3.3 \cdot 10^{-17}$ W. As the photon energy is $h\nu = 3.7 \cdot 10^{-19}$ J, this power corresponds to about 90 photons per second. An example of low level signal detection is presented in chapter 4.2.2.

2.4 Conclusion

Heterodyne detection is a powerful method to measure the amplitude and the phase of an optical field. The advantages of heterodyne detection compared with homodyne techniques [10, 15] are several. We can always choose a sufficiently large reference power to allow shot noise limited detection. We gain a factor 2 with respect to direct detection. Low optical signal can be detected (down to 10^{-17} W) and the optical phase can be measured with high accuracy (down to 0.33° for an optical power P_o = 1 pW). However, measuring the phase with high accuracy requires good optical and mechanical stability.

3 Optical heterodyne probe system

In this chapter, we describe the optical heterodyne probe system. A complete description of the basic elements and devices constituting the set-up will be given. The principle of optical heterodyne detection has been introduced in chapter 2. The main concept of the heterodyne probe system is to combine a heterodyne dynamic interferometer with a scanning near-field optical microscope (SNOM) in order to measure the amplitude and phase of optical fields in the near- and far-field region. The concept of a pseudo-heterodyne scanning microscope was introduced few years ago [17] and an attempt at making a heterodyne photon scanning tunneling microscopy had been made [18]. However, intense activity to obtain phase measurements with heterodyne techniques [19-21] or with other interferometric methods [22-24] has arisen only recently. The instrument presented in detail in this chapter has been entirely developed within the framework of this thesis. A signal to noise ratio measurement will be shown in order to verify the characteristics of the system and the heterodyne relations of chapter 2. As a first test of optical field measurement, we will study the amplitude and phase of a plane wave.

3.1 Description of the set-up

The complete optical heterodyne probe set-up is shown in Fig. 3.1. After separation of the Nd:YAG laser beam (of frequency $\nu = 5.6\ 10^{14}$ Hz) by a beam splitter (BS, ratio 96/4%), the object beam is shifted in frequency by two acousto-optic modulators AOM1 and AOM2 *(IntraAction-corp, Model AOM-40 series).* The two frequencies ($f_1 =$ 40.07 MHz and $f_2 =$ 40.00 MHz) are produced by two frequency generators *(Wavetek, Synthesized signal generator, Model 2510).* The electrical power of both signals is amplified up to 2 W in order to drive the AOM. Both illumination and reference beams are injected into a single-mode fiber. The polarization state can be controlled by a fiber polarization controller *(General Photonics Corp., Model PolaRITE PLC-003).* The object beam illuminates the sample by means of different

configurations, presented in Fig. 3.4. The optical information is collected by a commercial bent fiber probe, which is brought close to the sample by a commercial atomic force microscope. The reference and object beams are combined in the fiber coupler *(Wave Optics Inc., Single mode coupler)*, producing a beat signal at 70 kHz, detected by a standard silicon photodiode. Since the object power P_o is small compared with the reference power P_r, the coupling ratio of the fiber coupler is chosen to be 90% P_o to 10% P_r. The fiber polarization controller 1 is used to get maximum interference contrast between the object and the reference waves. During the measurement, the polarization is stable. The photodetector is isolated electrically from the optical table to avoid electrical noise. All ends of the fibers are cleaved at an angle of 12° to avoid back-reflections. The optical path difference of the two arms of the interferometer should be as small as possible to reduce the effects of limited temporal coherence. The length of each arm can be large (geometrical path length of about 5 meters). Therefore, good mechanical stability is required. The entire system is mounted on an optical table with vibration control. The amplitude and phase are extracted from the output signals ($R\cos\phi$ and $R\sin\phi$) of a lock-in amplifier *(Stanford Research Systems, Model SR530)*. The lock-in amplifier works with an electronic reference signal (given by an electronic frequency mixer) at the beat frequency, coherent with the measured signal. The lock-in amplifier has a narrow bandwidth (which is chosen to be B = 16.7 Hz). Only the signal at 70 kHz ± 16.7 Hz is demodulated.

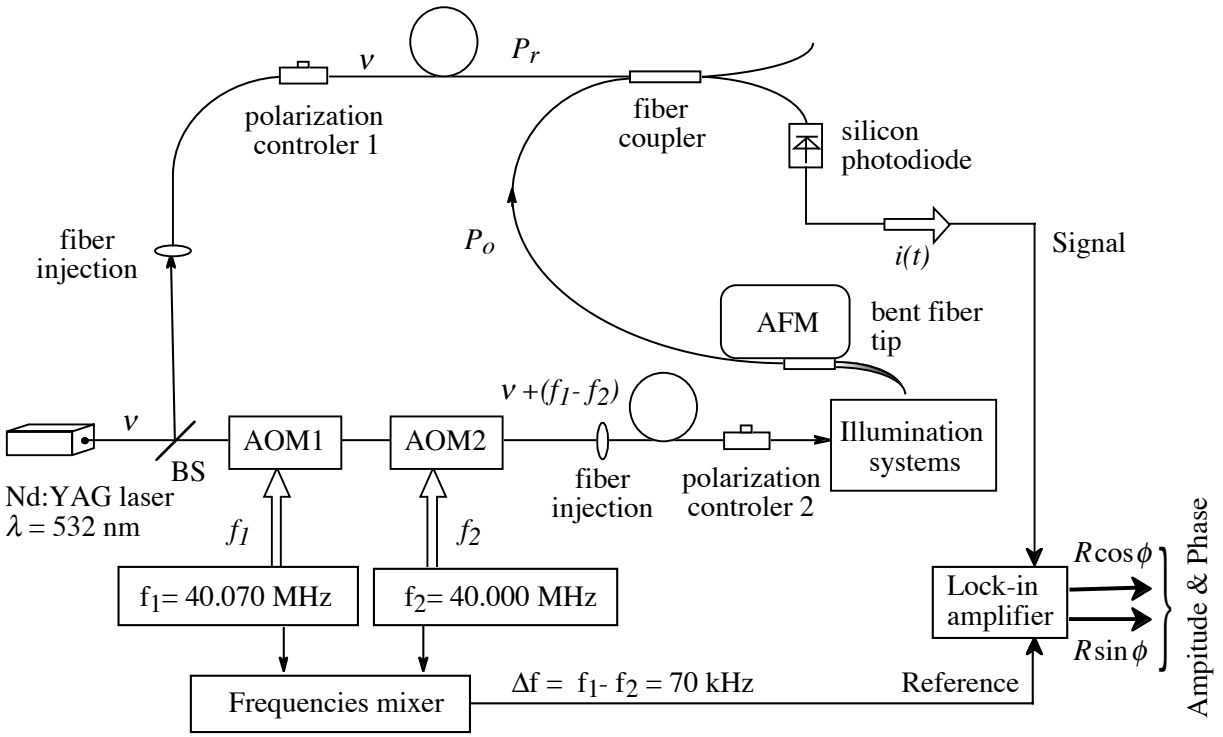

***Figure 3.1**: Photon scanning tunneling microscope with heterodyne detection.*

We can separate the system of Fig. 3.1 into two sections: the interferometer part, including the laser, AOMs, fiber injections (Fig. 3.2); and the SNOM section, including the atomic force

microscope (AFM), tip, fiber coupler, illumination and scanning system, the sample and the detector (Fig. 3.3).

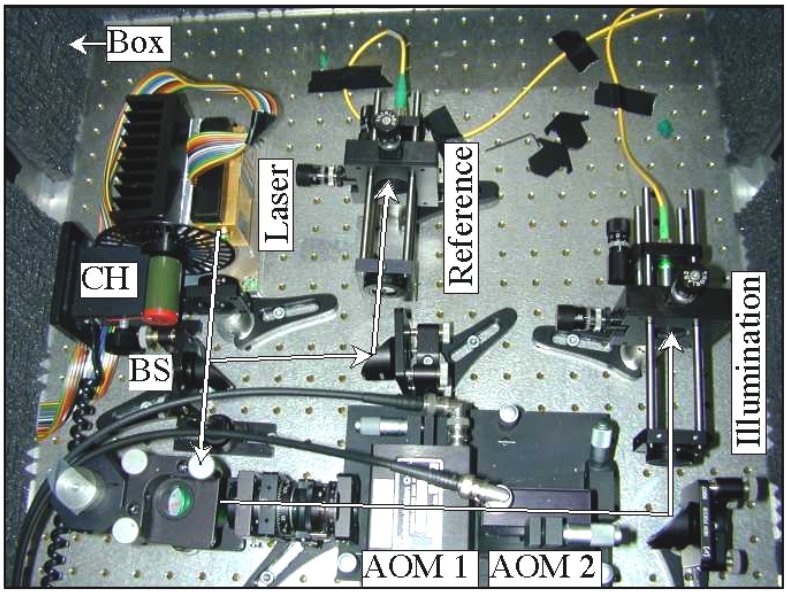

***Figure 3.2**: Photograph of the first part of the set-up (heterodyne interferometer) including the laser, the beam splitter (BS), a chopper (CH), the acousto-optic modulators (AOM 1 and 2) and the fiber injections for the reference and illumination beams. The system is enclosed in a plexiglas box.*

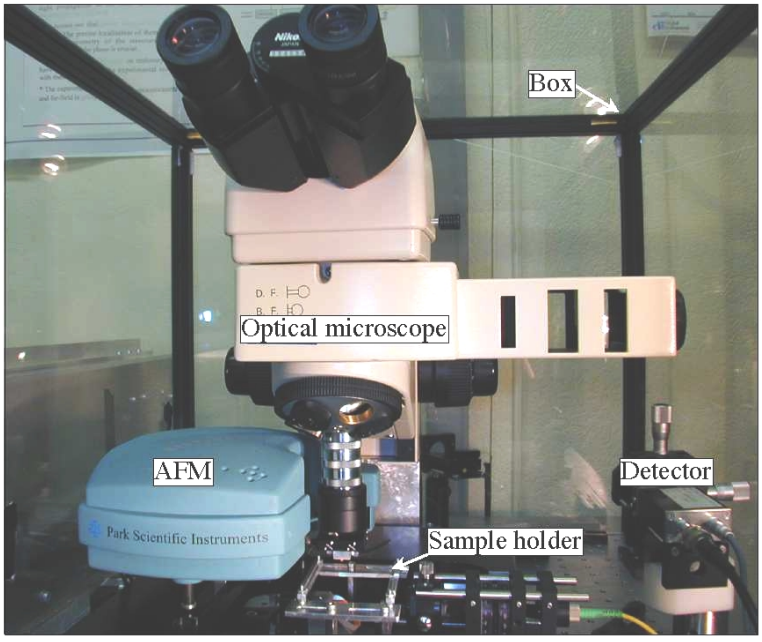

***Figure 3.3**: Photograph of the second part of the set-up including the AFM, the optical microscope, the sample holder on the XYZ scanner, the detector and another isolating plexiglas box.*

Two separate plexiglas boxes enclose each part of the system (Figs 3.2 and 3.3). In fact, air currents, local temperature fluctuations and acoustic noise induce fluctuations in the interferometer. The phase accuracy, for measurement over a long time (minutes), depends critically on the interferometer stability and has been substantially improved thanks to this shielding. Two separate boxes have been chosen for the two sections of the set-up in order to minimize air volumes. Silica gel plates can be introduced into the box surrounding the sample to reduce humidity for particular applications (e.g. in section 4.2.4).

Two different configurations for the sample illumination are available in the final set-up (Fig. 3.4). The illumination fiber output (F) is collimated to become a plane wave and the polarization is controlled by the polarization fiber controller 2 (Fig. 3.1), a half-wavelength plate (H) and a Glan-Thomson polarizer (P) to get the desired illumination mode. A collimating lens (CL) focuses the beam to increase the intensity of the illumination. However, the focus plane is placed about 2-3 cm in front of the sample; in this case, the curvature of the spherical wave illumination is negligible. We can expose the sample by normal illumination (Fig. 3.4 top) or by total internal reflection (TIR) (Fig. 3.4 bottom) illumination. More detailed schemes will be shown later. For normal illumination, the beam is directed to the sample by a 45°-mirror. For TIR illumination, the sample is placed on a prism by means of index matching oil. Bringing the cantilever bent fiber probe as an atomic-force microscope (AFM) [25] close to the surface, we perturb the evanescent field (created by TIR), resulting in propagation of light in the fiber. This process is called frustrated total internal reflection and the device working in this regime is called a PSTM (photon scanning tunneling microscope) [26-32].

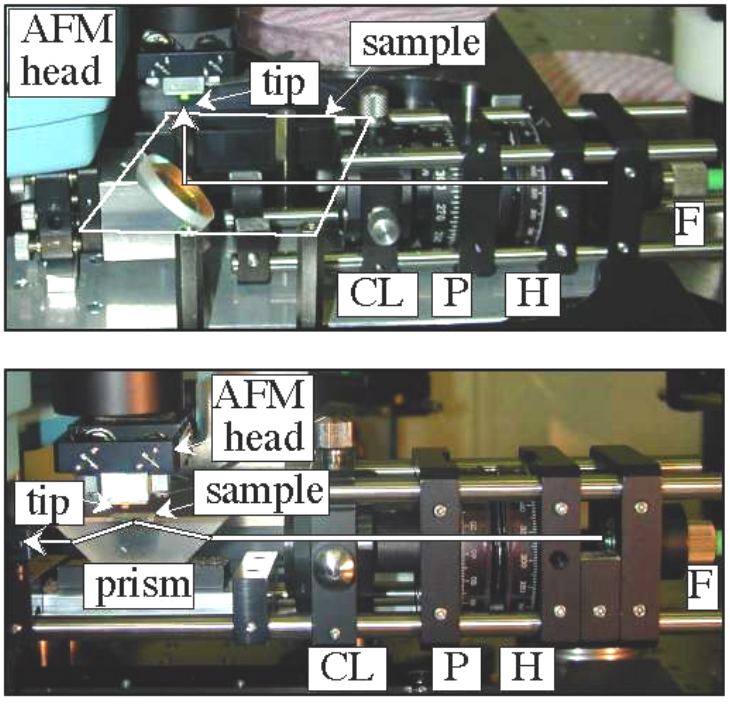

***Figure 3.4**: Two different set-ups for normal incidence illumination **(top)** and for total internal reflection illumination **(bottom)** with a small prism. P is the Glan-Thomson polarizer, CL the collimating lens, H the half-wavelength plate, F the illumination fiber output.*

The scanning is realized by a separate *x-y-z* piezoelectric closed loop translation stage *(Physik Instrumente GmbH, Model P-517-3CL)*. The sample with the illumination optics is mounted on this translation stage and is moved relative to the fixed position of the tip. The scanner is a solid-state (ceramic) actuator allowing nano-metric displacements. Since the displacement of a piezo actuator is based on the orientation of electrical dipoles in the elementary piezo-material cells, the resolution depends on the electrical field applied and is theoretically unlimited. In practice, the resolution can be limited mainly by piezo amplifier noise. The resolution of the step displacement in the *z*-direction is 0.1 nm and 1 nm in the *x*- and *y*-directions.

3.2 Instrumentation

3.2.1 Laser

The laser which has been mainly used is a 150 mW single mode (TEM00) frequency-doubled Nd:YAG diode-pumped solid-state laser ($\lambda =$ 532 nm) *(Coherent Inc., Model COLCOMPASS 315M-150)*. A 1 mW single mode frequency-stabilized He-Ne laser ($\lambda =$ 633 nm) *(ReniShaw, Model* SL10*)* laser has also been used. Both of these lasers have a long coherence length ($l_{\mathrm{Nd:YAG}} >$ 60 m and $l_{\mathrm{He-Ne}} >$ 300 m) and are stable in intensity.

3.2.2 Detector

The detector of Fig. 3.5 consists of a silicon photodiode *(Vishay Telefunken, Model BPW 34)* followed by a transimpedance amplifier circuit, using a high-speed and low current noise operational amplifier (*Burr-Brown, Model OPA 602*).

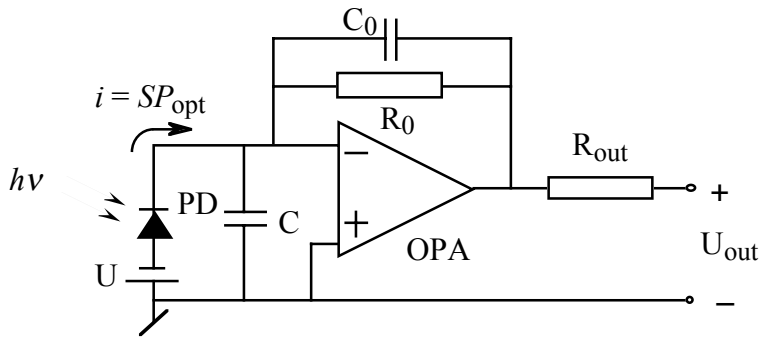

Figure 3.5*: Detector circuit consisting of a standard PIN photo-diode (PD) followed by a transimpedance amplifier (operational amplifier OPA).*

The photodiode is supplied by a bias $U = 15$ V. The capacitor C takes into account the photodiode capacitance $C_d = 15$ pF and the amplifier input capacitance $C_a = 3$ pF ($C = C_d + C_a$). A serial resistor ($R_{out} = 50\ \Omega$) is added at the output of the detector to adapt its impedance to the 50 Ω impedance of the coaxial-cables used. If the input impedance R_{in} of the measuring devices (oscilloscope, lock-in amplifier or spectrum analyzer) is large compared with R_{out}, the input voltage measured by the device is the same as the voltage at the output of the detector. The total resistance $R_L = R_{in} + R_{out}$ is called the *load resistance*.

The photocurrent of the photodiode is given by

$$i = SP_{opt}, \tag{3.1}$$

where P_{opt} is the incident optical power and S the response (spectral sensitivity) of the silicon photodiode; $S = 0.4$ A/W at $\lambda = 633$ nm and $S = 0.33$ A/W at $\lambda = 532$ nm. Since the photocurrent i is small, an amplifier circuit is needed to detect the signal in a convenient way. The operational amplifier also controls the voltage at the photodiode boundary and regulates the current flux through the feedback resistance $R_0 = 4.7 \cdot 10^5\ \Omega$. The contribution of the noise by the amplifier can be neglected because it is smaller than the thermal noise of the feedback resistor R_0 at T = 300 K. In this case, the SNR at the amplifier output is the same as at the photo-diode output. A feedback capacitor $C_0 = 1.5$ pF is added to minimize phase distortion of the frequency response at the cut-off frequency.

The relation between the measured dc voltage at the output of the detector and the incident optical power is given by

$$U_{out} = SR_0P_{opt}. \tag{3.2}$$

The output voltage ranges from 0 to 10 V. If the optical power is modulated at a frequency ω/2π, the output voltage of the transimpedance amplifier can be expressed by [10]

$$V_{out}(\omega) = \Re(\omega) \cdot S \cdot P_{opt}(\omega), \tag{3.3}$$

where $\Re(\omega)$ is the transfer function of the detection circuit. The frequency response $|\Re(\omega)|$ of the specific detector (of Fig. 3.5) was measured using a modulated light emitting diode (LED). By varying the frequency of the LED current between 10^4 Hz and 10^7 Hz, we acquired the frequency response of the detection circuit with a spectrum analyzer *(Hewlet Packard, Model 4195A)*. The result is shown in Fig. 3.6. The detector pass-band (at –3 dB) is 300 kHz. The beat frequency has been chosen at 70 kHz which is well below the cut-off frequency. The response U_{out} to an optical input power P_{opt} is then given by $U_{out} = R_0SP_{opt}$. Calculation of the amplification gain of the detector with the given parameters agrees with the measurement.

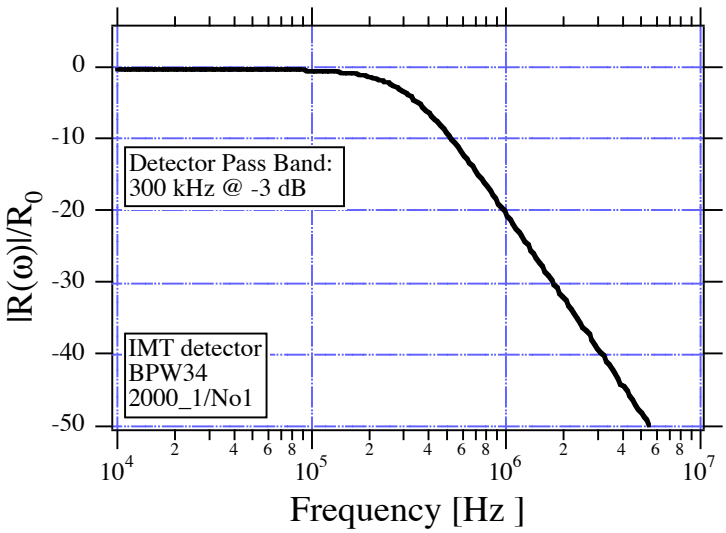

***Figure 3.6**: Measured detector normalized frequency response. The detector pass-band (at –3 dB) is 300 kHz.*

Taking into account the feedback resistor R_0 and the load resistor R_L, Eq. (2.7) for thermal noise becomes

$$P_{TN} = 4 \cdot k \cdot T \cdot B \cdot \frac{R_0}{R_L} \tag{3.4}$$

In Fig. 3.7, we measured the noise level of the detector in the dark with a FFT spectrum analyzer *(Stanford Research Systems, Model SR770 FFT Network Analyzer)*, with an input impedance of $R_{in} = 1$ MΩ and working in the frequency range of 0 to 100 kHz). With $R_0 = 470$ kΩ, $R_L \cong 1$ MΩ ($R_{out} = 50$ Ω), $B = 62.5$ Hz and T = 300 K, the calculated electric power corresponding to the thermal noise is $P_{TN} = 5 \cdot 10^{-19}$ W.

The FFT analyzer measures the spectrum in dBV units ($U_{dBV} = 20\log\left(U_V / U_{ref}\right)$), where U_V is the input voltage of the signal and $U_{ref} = 1$ V is the reference voltage. The corresponding electric power is obtained through

$$P = \left[10^{\left(U_{dBV}/10\right)} \right] \cdot U_{ref}^2 \Big/ R_L . \tag{3.5}$$

The measured electric power corresponding to the thermal noise of the detector is $P_{TN} = 1 \cdot 10^{-18}$ W (Fig. 3.7). The measured noise power is a factor 2 larger than the calculated thermal noise power, which is quite satisfactory.

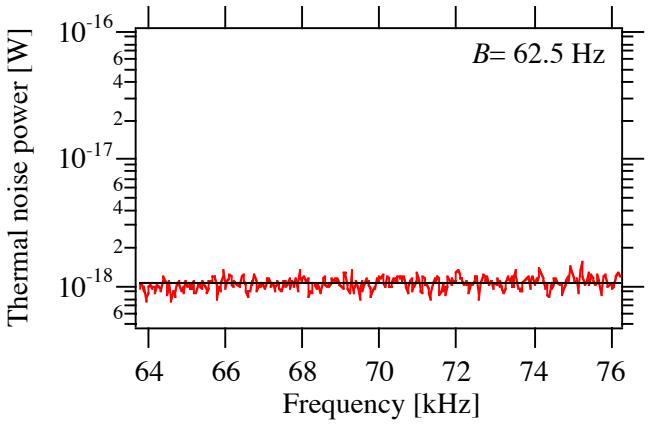

***Figure 3.7**: Measured electric noise power (around 70 kHz) of the detector without optical input (analyzer bandwidth of B = 62.5 Hz).*

3.2.3 AFM/PSTM microscope and fiber probes

Approach of the probe to the sample is controlled by a commercial atomic force microscope (AFM) *(Park Scientific Instruments, Model BioProbe)* (Fig. 3.3). A laser diode beam is deflected by a mirror (M1) and focused on the top of the fiber cantilever. Then, the beam is deflected by the cantilever and directed by a second mirror (M2) onto a four-quadrant position-sensitive photodetector (PSPD) (Fig. 3.8). The PSPD can measure displacements of light as small as 1 nm. Usually, flat silicon cantilevers with pyramidal tips are used. Due to the cylindrical shape of the fiber, the beam reflected from the fiber cantilever spreads out in a line perpendicular to the fiber. The displacement of this line light is measured with good accuracy by the detector. As the tip approaches the surface, inter-atomic forces (van der Waals repulsion forces [33]) between the tip apex and the surface cause the cantilever to bend, deflecting the laser beam. The position of the deflected signal is sent to computer feedback to control the approach before touching the surface.

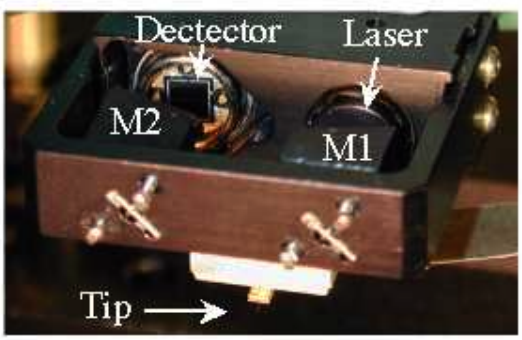

a)

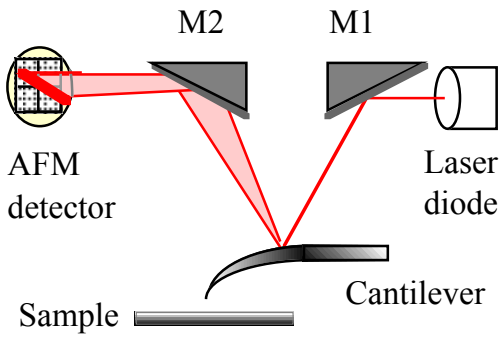

b)

***Figure 3.8**: **a)** Atomic-force microscope (AFM) head and **b)** AFM regulation mechanism.*

In general, atomic-force microscopes are used to image the surface topography on an atomic scale by scanning a sample area. However, we did not use the fiber cantilever for this purpose. In

fact, fiber cantilevers are quite bad AFM tips, because of their rigidity. The force constant is about 4 N/m compared with 0.02 N/m for a typical silicon cantilever. However, the AFM regulation allows control of the approach of the fiber probe to the surface. Once the approach done, the feedback control of the AFM is switched off and scanning is carried out at constant height above the surface.

In conventional photon scanning tunneling microscopes (PSTMs), the sample is illuminated by total internal reflection. The tip-sample distance approach is controlled by the optical measurement of the exponential rise of the evanescent wave above the sample. By combining the AFM approach system with the PSTM optical detection (of the evanescent field), the resulting device gives birth to the AFM/PSTM microscope [34-36].

The probes used in this work are bent fiber tips, made from single-mode fibers (3.4 µm mode diameter), with a Germanium doped core of 3 µm diameter and a pure silica cladding of 125 µm diameter [37]. The working wavelength is 515 nm and the cut-off wavelength is 460 nm (± 40 nm). The fiber end is bent by laser heating in order to be used as a conventional AFM cantilever. The cantilever is 400 to 500 µm long and the curved part is 120 to 200 µm (Fig. 3.9a). The fiber apex is heated and pulled to produce sharp tips (Fig. 3.9b). A thin metal layer is then deposited on the fiber probe and covers the apex of the tip entirely.

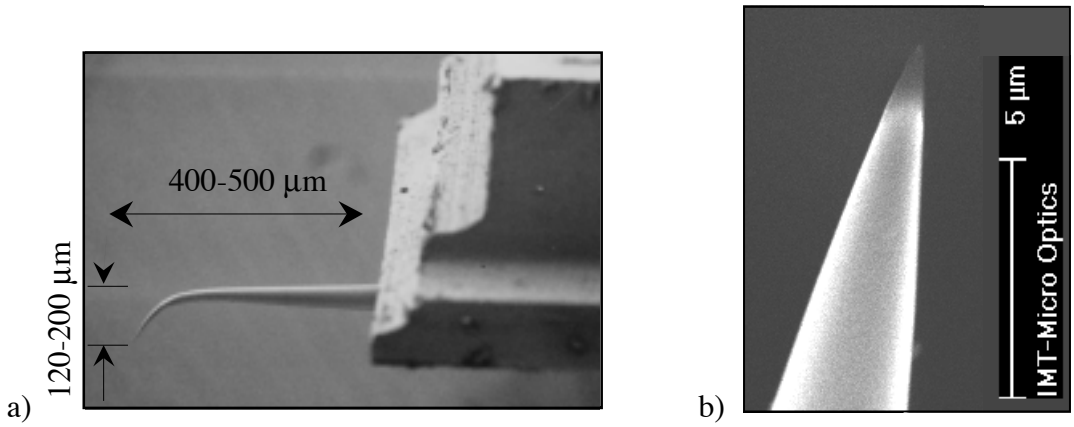

Figure 3.9*: Aperture less bent fiber tip.* ***a)*** *Image of the bent fiber cantilever glued to a silicon plate.* ***b)*** *SEM image of the tip apex.*

The metal thickness (about 20-50 nm) determines the aperture at the apex. In Fig. 3.10a, we present a 2-D model of the tip apex using commercial software *MAFIA4* [38, 39]. The apex has been modeled by a hemispherical shape. The core of the probe is a dielectric material (glass of dielectric constant $\varepsilon_{diel} = 2.25$) and the apex has an internal curvature radius of $r = 50$ nm. The dielectric apex is coated with Chromium ($\varepsilon_{Cr} = -12.3 + i \cdot 24.5$ at $\lambda = 516.6$ nm [40]). The apex has an external curvature radius of $R = 70$ nm so that the metal thickness is 20 nm at the end of the tip. Chromium is preferred to Aluminum because *Al* forms large aggregates of particles and the apex is not always well defined. In this model, we see that the light tunnels

through the metal layer and determines a well-defined light localization. In Fig. 3.10b, a cross-section of the electric field (indicated by "b" in Fig. 3.10a) is shown. We can see the extension of the field at the apex. The full-width at half maximum (FWHM) gives the "aperture" of the tip, which is about 16 nm.

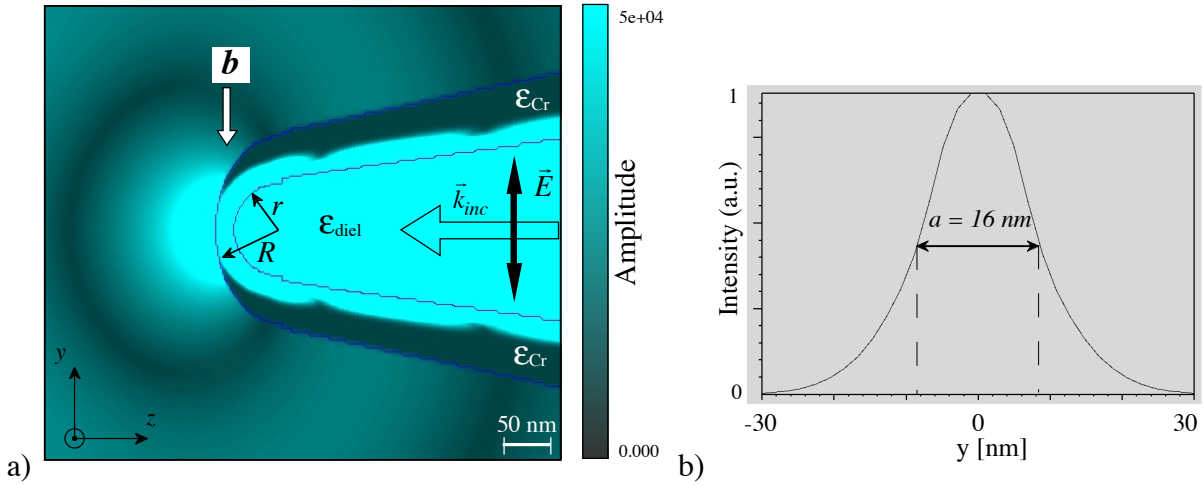

***Figure 3.10**: 2-D modeling of a fiber tip entirely coated with Chromium using MAFIA4 software. **a)** Amplitude of the electric field (y-polarized) is shown (in gray scale). **b)** Cross-section of the intensity (indicated by "b" in Fig. 3.10a). The FWHM defines an aperture of 16 nm.*

In Fig. 3.11, we present a fiber tip model (with the same properties as before) with an aperture. The apex has been cut in order to make a physical hole of 80 nm. We observe that the field is not better defined than in the previous case. In fact, we can see two halos at each part of the metal extremity.

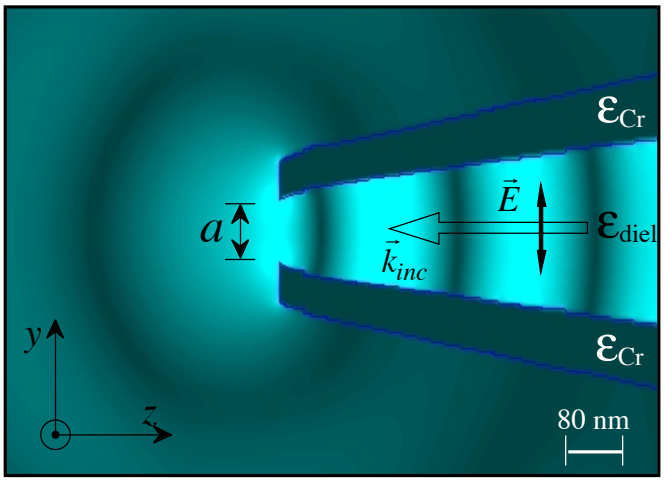

***Figure 3.11**: 2-D modeling of a fiber tip coated with Chromium metal using MAFIA4 software. Amplitude of the electric field (y-polarized) is plotted (in gray scale). A hole has been opened at the apex (with an aperture of a = 80 nm).*

These tip models demonstrate clearly that *no physical hole* is required in near-field fiber probes.

3.2.4 Signal processing and acquisition

The signal processing is mainly performed with a lock-in amplifier *(Stanford Research Systems, Model SR530)*. The two quadrature signals of the electrical input signal (proportional to the optical beat signal) with respect to the reference signal (at the beat frequency of 70 kHz) are obtained from the analog outputs ($R\cos\phi$ and $R\sin\phi$) of the lock-in amplifier. The amplitude and the phase are then extracted from these two signals by numerical calculation (Eqs. (3.13) and (3.14)). The range of the output signals is 0-10 V. The full-scale sensitivity ranges from 100 nV to 500 mV. The input impedance of the signal is $R_{in} =$ 100 MΩ with a frequency range from 0.5 Hz to 100 kHz. The noise voltage specification for the SR530 model is 7 nV/$\sqrt{\text{Hz}}$ at 1 kHz. The measured thermal noise (Eq. (3.4) and Fig. 3.7) of the detector is $P_{TN} = 10^{-18}$ W with $R_L = 1$ MΩ and $B = 62.5$ Hz. The corresponding voltage noise density is then

$$\sqrt{\frac{\langle U_N^2 \rangle}{B}} = \sqrt{\frac{R_L P_{TN}}{B}}. \tag{3.6}$$

With the same R_L and B we get 0.1 $\mu\text{V}/\sqrt{\text{Hz}}$, which is much larger than the voltage noise density of the lock-in amplifier. Thus, the noise of the lock-in amplifier is negligible.

The signal acquisition can be accomplished in different ways. If the scan is controlled by the AFM commercial software, the two signal outputs of the lock-in amplifier are sent to the AFM electronics through a signal access module (SAM). The driving AFM software ("Dp.exe" software of *Park Scientific Instruments*) saves the two inputs (channels Raw1AM2 and Raw1AM3) into non-standard "hdf" (hierarchical data format) files. These files are converted into simple text format files (using "ScanActiveX"). Then, with e.g. Matlab, an image is built from the data.

In the final set-up configuration, where the scanning is done by an external *x-y-z* piezoelectric translation stage, the signal is acquired with software written in Labview (cf. chapter 8.1). The tip approach is done by means of the AFM software. Then, the AFM electronics feedback is switched off and the raster scan, as well as the image acquisition, is accomplished by the software. A linear voltage ramp is applied to the piezo-stage to scan in one direction and the data acquisition is performed simultaneously. The number of samples N_s, the scan dimension D_s and the integration time τ of the lock-in amplifier are chosen. For each sampling point, the signal is acquired during τ, which is typically 10-30 ms. Thus, the time needed to scan one line is

$$T = \tau \cdot N_s. \tag{3.7}$$

The scanner displacement D_s in one direction (e.g. in the *x*-direction) is synchronized with the scan time *T*. For instance, for a number N_s of 128 pixels, scanning on one line will take 3.8 seconds. For a 2–D image (128 x 128 pixels), the acquisition will take about 8 minutes.

3.3 Signal to noise ratio of the heterodyne detection

We will show a measurement of the signal to noise ratio with the system of Fig. 3.1. As an example, we send the object beam (without sample) directly to the fiber tip and measure the SNR. The laser is a 1 mW He-Ne frequency stabilized laser ($\lambda = 633$ nm). The photodetector is the same as described in section 3.2.2 ($R_0 = 470$ kΩ, $\eta = 70\%$, $S = 0.4$ A/W at $\lambda = 633$ nm).

From Eq. (3.4), we have calculated for these parameters the thermal noise to be $P_{TN} = 5 \cdot 10^{-19}$ W (at $R_L = 1$ MΩ given by the input impedance of the spectrum analyzer). From Eq. (2.16), the minimum required power for the reference to get shot noise limited detection is $P_r^{\min} = 0.275$ μW (at $T = 300$ K). We have chosen $P_r = 1$ μW.

The object power has been determined independently to be $P_o = 15$ pW. It has been measured by blocking the reference beam and using the lock-in amplifier with a chopper (Fig. 3.2) *(Stanford Research Systems, Model SR540)* to modulate the laser intensity.

Taking into account the load resistor R_L, we get with Eq. (2.10) for the electric noise power corresponding to the shot noise

$$P_{SN} = 2eBSP_{tot} R_0^2 / R_L. \tag{3.8}$$

With $P_{tot} \cong P_r = 1$ μW, $B = 62.5$ Hz and $R_L = 1$ MΩ, the shot noise power is $P_{SN} = 1.8 \cdot 10^{-18}$ W. The ac signal power of Eq. (2.14) at R_L becomes

$$P_{AC} = 2m^2 S^2 P_r P_o R_0^2 / R_L. \tag{3.9}$$

By assuming $m = 1$, the expected ac signal power is found to be $P_{AC} = 1 \cdot 10^{-12}$ W. By dividing Eq. (3.9) by Eq. (3.8), the theoretical signal to noise ratio is 57.5 dB.

The measured spectrum of the heterodyne signal corresponding to $P_o = 15$ pW is presented in Fig. 3.12. The measured electrical power corresponding to the heterodyne (AC) power and the shot noise power are $P_{AC} = 3.3 \cdot 10^{-12}$ W and $P_{SN} = 5.3 \cdot 10^{-18}$ W, respectively. The corresponding measured signal to noise ratio is then 57.9 dB and agrees well with the theory. In

fact, the difference of 0.4 dB corresponds to a factor 1.1 between the measured and the calculated P_{AC}/P_{SN} ratio. The difference probably comes from the error in measuring the absolute power of the object power P_o. The difference corresponds to an object power of about 17 pW. It is difficult to measure a low optical power with a precision of better than 10%.

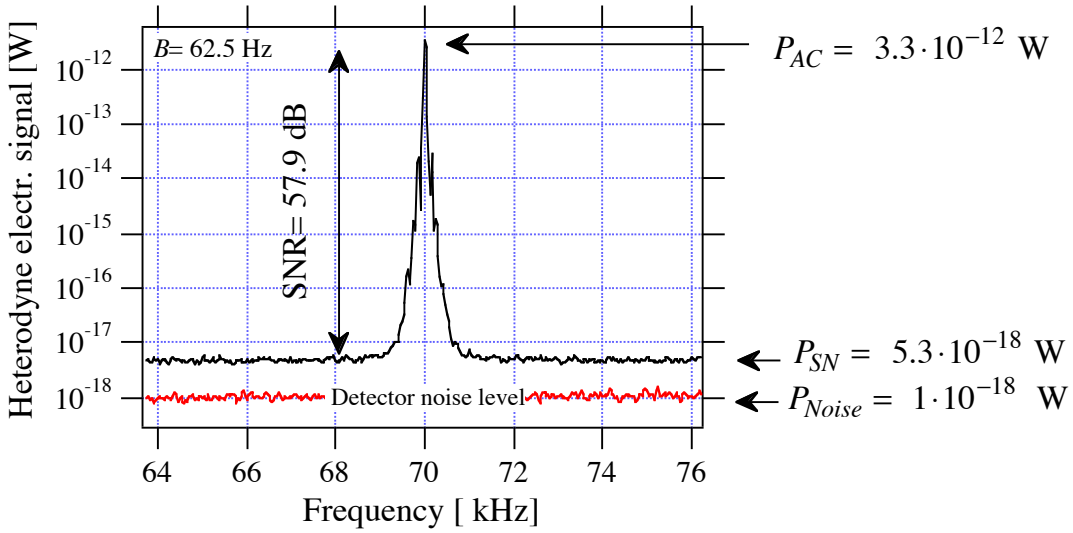

***Figure 3.12**: Measured heterodyne spectrum at the center frequency of 70 kHz. The measured signal to noise ratio of 57.9 dB agrees well with the theoretical value of 57.5 dB.*

From Eq. (2.21), we get that the measured signal to noise ratio of 58 dB for an optical power of 15 pW allows a phase resolution of 0.07°. This result expresses the extreme quality of phase measurements obtainable using heterodyne interferometry.

3.4 Amplitude and phase measurements

The complex amplitude of the optical field sampled by the fiber tip is given by

$$V(\mathbf{x},t) = A(\mathbf{x})\ \exp\left[i\phi(\mathbf{x})\right]\ \exp(i\omega t). \tag{3.10}$$

where $A(\mathbf{x})$ is the amplitude and $\phi(\mathbf{x})$ is the phase. In most photon scanning tunneling microscopes, only the intensity $I = |A|^2$ is measured. However, because we use heterodyne detection, direct measurement of the amplitude and the phase is possible. Using synchronous detection of the heterodyne signal with a lock-in amplifier, we get the two electronic output signals

$$S(\mathbf{x}) = a(\mathbf{x})\ \sin\phi(\mathbf{x}) \text{ and} \tag{3.11}$$

$$C(\mathbf{x}) = a(\mathbf{x})\ \cos\phi(\mathbf{x}). \tag{3.12}$$

where $a(\mathbf{x})$ is proportional to the optical amplitude $A(\mathbf{x})$. From $S(\mathbf{x})$ and $C(\mathbf{x})$, $a(\mathbf{x})$ and $\phi(\mathbf{x})$ can be calculated. The amplitude is obtained through

$$a(\mathbf{x}) = \sqrt{C^2(\mathbf{x}) + S^2(\mathbf{x})}, \tag{3.13}$$

and the phase through

$$\phi(\mathbf{x}) = \text{atan2}\left[S(\mathbf{x}) \big/ C(\mathbf{x})\right], \tag{3.14}$$

where the function atan2 is the four quadrant arctangent of the real parts of the elements of $S(\mathbf{x})$ and $C(\mathbf{x})$, delimited by $[-\pi, +\pi]$.

Besides the fact that coherent detection allows the phase of the optical field to be determined, we also get an increased dynamic range. This increase is due to the fact that the amplitude $a(\mathbf{x})$ of the electrical signal is proportional to the amplitude $A(\mathbf{x})$ of the optical field, rather than to the intensity $|A|^2$. In addition, we can always get shot-noise-limited detection, even with a photodiode, if P_r is chosen to be sufficiently large to overcome the electronic noise (section 2.3).

3.4.1 Amplitude and phase measurement of a plane wave

As a test of the heterodyne scanning probe microscope we measured the amplitude and the phase of a plane wave. By sending the object beam directly to the fiber tip with an incident angle θ (compared to the z-direction), we measured the optical amplitude and phase by varying the position of the tip in the z-direction.

A plane wave propagating in air is described by

$$E(z,t) = E_o \exp\left[-i\left(kz\cos\theta + kx\sin\theta + \varphi_0\right)\right]\exp(i\omega t), \tag{3.15}$$

where E_0 is the amplitude, k the wave number and φ_0 the phase shift. As a function of z, the amplitude is constant (E_0) and the phase is

$$\phi(z) = kz\cos\theta + \varphi_0. \tag{3.16}$$

The measured amplitude and phase as a function of z are presented in Fig. 3.13. In the ideal case, when the incoming beam is perfectly parallel to the tip movement (i.e. $\theta = 0$), the period for the phase is λ. In our measurement we had $\theta = 25°$, which gives a period of $\Lambda = \lambda/\cos\theta = 586$ nm (Fig. 3.13b).

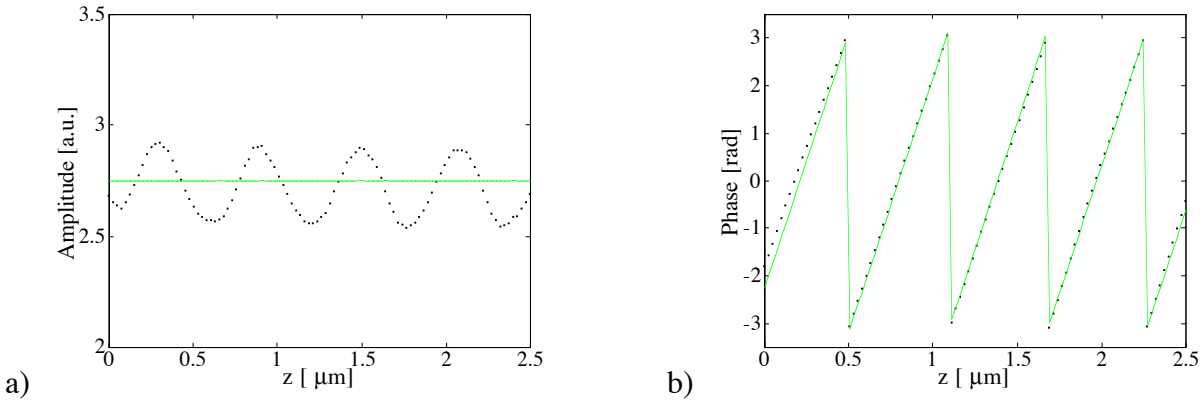

a) b)

Figure 3.13*: 1-D measured plane wave* ***a)*** *amplitude and* ***b)*** *phase. Doted curves are experimental measurements and the solid lines are the calculated functions.*

The measured phase fits very well the theoretical curve (Eq. (3.16)), but the measured amplitude shows an unexpected periodic modulation. This can be explained by an interference phenomenon in the system. During the measurement, another beam is reflected (or scattered) and the tip detects the interference.

The interference of two plane waves of same frequency and with intensities I_1 and I_2, respectively, can be described as Eq. (2.6), but in the space domain instead of the time domain. The total intensity of the interference can be expressed by

$$I = I_1 + I_2 + 2\sqrt{I_1 I_2}\cos(2\pi z/\Lambda + \Delta\varphi) \tag{3.17}$$

where $I_1 + I_2 = I_{dc}$ is the dc level, $2\sqrt{I_1 I_2} = I_{ac}$ the amplitude of the intensity modulation, Λ the interference modulation period and $\Delta\varphi$ is the phase difference.

From the measured amplitude (Fig. 3.13a), we get the dc level $I_{dc} = I_1 + I_2 = 7.45$ (a.u.) and $I_{ac} = 2\sqrt{I_1 I_2} = 0.94$ (a.u.) amplitude of the optical signal (Fig. 3.14a). We can thus calculate the respective intensities to be $I_1 = 7.42$ (a.u.) and $I_2 = 0.03$ (a.u.). The intensity ratio of the two interfering waves is $I_2/I_1 = 0.4\%$. The visibility of the interference, defined by

$$\Gamma = \frac{2\sqrt{I_1 I_2}}{I_1 + I_2} \tag{3.18}$$

is then 3%. We can thus conclude that even with a small visibility, the interference is well detected thanks to heterodyne detection.

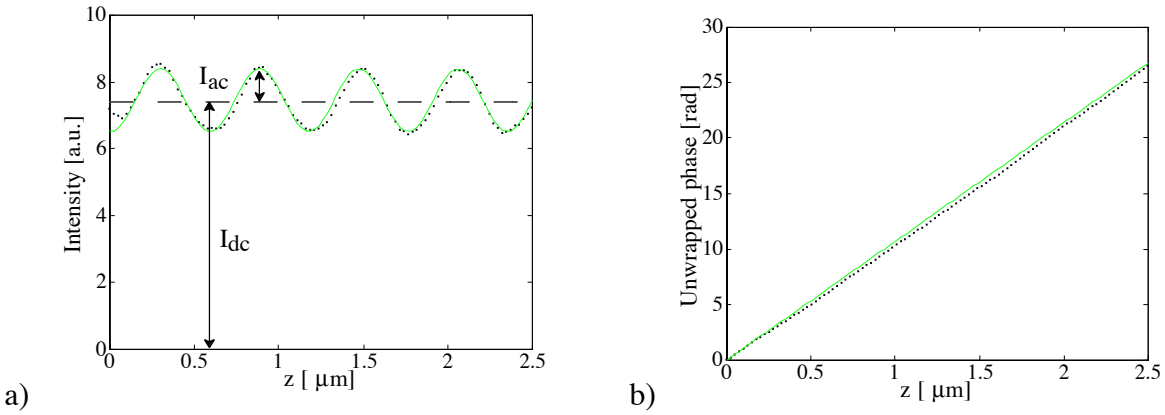

Figure 3.14: *Plane wave measurement. The plain curve is the calculated interference and the dotted curve is the measured* ***a)*** *intensity modulation with the ac and dc levels,* I_{dc} *and* I_{ac}*, respectively.* ***b)*** *Unwrapped phase.*

A two-dimensional scan (in the X-Z plane) is presented in Fig. 3.15. This type of 2-D scans are often used throughout this work. We will show in chapters 4 and 6 such 2-D measurements in more detail. The propagation of a plane wave, given by the phase, becomes more clearly visible in this representation.

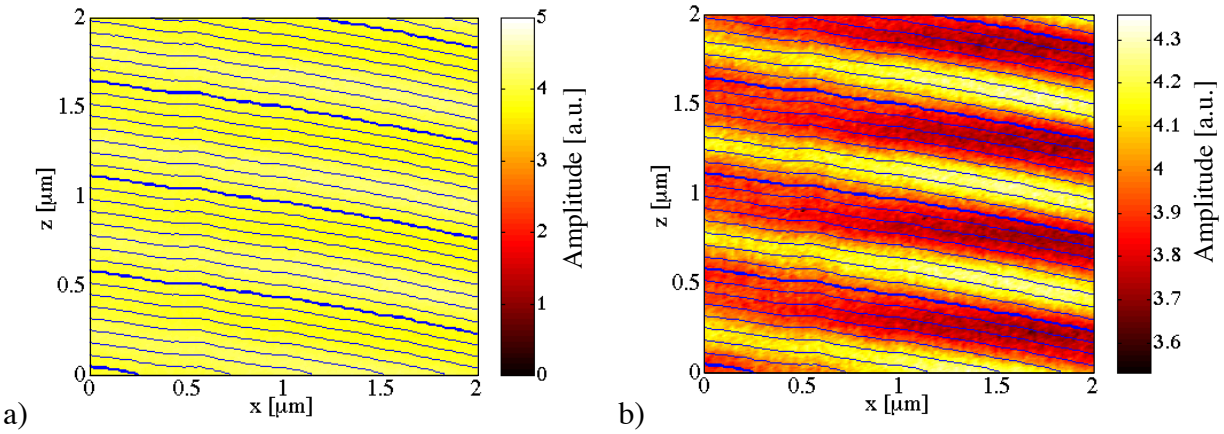

Figure 3.15*: Two-dimensional scan 2 by 2 µm (X-Z plane) of a plane wave amplitude (gray-scale) and iso-phase lines. The gray scale for the amplitude of* ***a)*** *is expanded in* ***b)*** *to emphasize the intensity variations.*

The iso-phase lines in Fig. 3.15 allow to see the phase fronts of the wave field. In fact, the tilt angle θ becomes more evident in this representation. Besides this, we can also observe a small curvature of the wave fronts due to the collimating lens (section 3.1 and Fig. 3.4).

3.5 Conclusion

In this chapter, the complete optical heterodyne probe system has been presented. This system allows amplitude and phase measurements of propagating or non-propagating optical fields. The main concept of the heterodyne probe system is based on the combination of a heterodyne interferometer with a scanning near-field optical microscope. All main components of the set-up have been presented. Comparison of the calculated and the measured noise of the detector proved that the heterodyne detection is shot noise limited. We have measured a signal to noise ratio of 58 dB for an optical signal power picked up by the fiber tip of only 15 pW, allowing a phase resolution of 0.07° (B = 62.5 Hz). As a first test, we measured the amplitude and the phase of a plane wave, which is the simplest optical field. We have also demonstrated that a physical hole is not necessary to build working near-field probes. The light can tunnel at the tip through a thin (about 20-50 nm) metallic coating.

4 Evanescent optical field

For many years, information transfer analysis by conventional optical microscopes has been based on the propagating wave concept. However, evanescent waves can give a new dimension to microscopy because of the increase in the resolution power [41] available to investigate structures which are becoming more and more miniaturized. A better understanding and consequently a better utilization of optical components is a consequence of the knowledge of the near-field of these optical components. The optical near-field is essentially characterized by evanescent waves, because of their non propagating behavior. We can speak of “near”-field when the field penetration in a medium is smaller than the wavelength, which is the case with evanescent waves. A slight perturbation in the near-field region can produce notable consequences for the field that propagates far from the object. This is a reason why we investigate the field near the object and in particular, in this chapter, the evanescent field. We can produce such waves by total internal reflection, diffraction by a small aperture, diffraction by a grating and diffraction in a waveguide for instance. Before analyzing the near-field of complex optical systems, it is necessary to study one simple configuration. In this chapter, we will mainly discuss evanescent waves caused by total internal reflection, because this is one of the easiest ways to produce them.

4.1 Photon tunneling

In this chapter, we will explain the concept of photon tunneling introduced in section 3.2.3 with the Photon Scanning Tunneling Microscope. This concept is rigorously bound with total internal reflection and, more precisely, with the frustration of total internal reflection.

4.1.1 Total internal reflection

Let us consider two media of refractive index n_1 and n_2. A plane wave illuminates the interface of the two media with an incident angle θ_1. If $n_1 < n_2$, there is always a refraction of the light (Fig. 4.1a). This means that the incoming beam will be split into a reflected beam, and a refracted (transmitted) beam in the second medium with a direction of propagation given by the *Snell-Descartes law* [42], or also called *refraction law* [43]:

$$n_1 \sin\theta_1 = n_2 \sin\theta_2, \tag{4.1}$$

where θ_2 is the angle between the refracted wave and the normal at the interface.

Let us now consider the opposite case where $n_1 > n_2$. The Snell-Descartes law allows a refracted wave only as long as the angle of incidence is smaller than a critical angle (Fig. 4.1b)

$$\sin\theta_c = n_2 / n_1 . \tag{4.2}$$

If this limit is exceeded, propagation of the transmitted wave is no longer possible and all the light is reflected (Fig. 4.1c). This phenomenon is called *total internal reflection*.

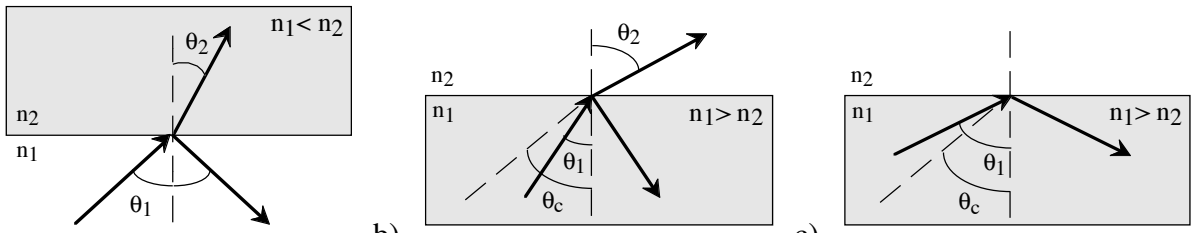

***Figure 4.1**: **a)** Refraction of a plane wave from a refringent medium to a more refringent medium. Refraction of a plane wave from a refringent medium to a less refringent medium **b)** in normal refraction ($\theta_1 < \theta_c$) and **c)** in total internal reflection ($\theta_1 > \theta_c$).*

We usually speak of *TE* (transverse electric), or *s*-polarization, when the electric vector $\vec{E}$ of the incident plane wave is normal to the incident plane and *TM* (transverse magnetic), or *p*-polarization, when $\vec{E}$ is parallel to the incident plane. Let us describe the system in Fig. 4.2 with $\vec{k}_i$, $\vec{k}_r$, $\vec{k}_t$ the incident, the reflected and the transmitted wave vectors, respectively. The refractive index n_1 is higher than n_2 and the angle of incidence θ is larger than θ_c.

In total internal reflection, the refracted wave vector has a real component in the *x*-direction and a purely imaginary *z*-component. Thus, the transmitted wave propagates parallel to the surface (i.e. along the *x*-axis) and is attenuated in the *z*-direction. In this case, we get an inhomogeneous plane wave or an *evanescent wave*.

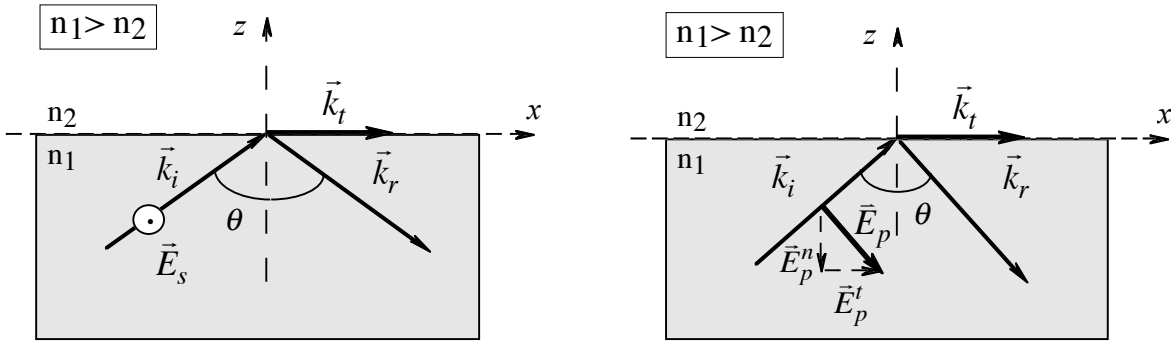

a) b)

***Figure 4.2**: Total internal reflection scheme **a)** in TE-mode and **b)** in TM-mode illumination. In TM-mode, the electric field $\vec{E}$ is decomposed in two components in the plane of incidence: $\vec{E}_p^n$ normal component, parallel to the x-direction and $\vec{E}_p^t$ the tangential component, parallel to the z-direction.*

Let us now consider the evanescent field in medium n_2 ($z \geq 0$). The boundary conditions associated with Maxwell's equations at the interface between the two homogeneous media with refractive indices n_1 and n_2 (in the $z = 0$ plane) have to be preserved [44]. Taking the boundary conditions into consideration, we get for the z-variation of the evanescent electric field in medium n_2 for *s*-polarization [45]

$$\vec{E}_s(z) = E_s^i \frac{2\cos\theta}{\cos\theta + i\sqrt{\sin^2\theta - n^2}} \exp\left(-z/d_p\right) \vec{e}_y \tag{4.3}$$

where $n = n_2/n_1$ is the relative refraction index and for *p*-polarization,

$$\vec{E}_p(z) = E_p^i \frac{2\cos\theta \left[-i\sqrt{\sin^2\theta - n^2}\vec{e}_x + \vec{e}_z \sin\theta\right]}{n^2\cos\theta + i\sqrt{\sin^2\theta - n^2}} \exp\left(-z/d_p\right). \tag{4.4}$$

where θ is the incident angle, $E_{s,p}^i$ the amplitude of the electric field at $z = 0$ and $\left(\vec{e}_x, \vec{e}_y, \vec{e}_z\right)$ are the normalized vectors of the x-y-z-direction. Equations (4.3) and (4.4) describe an exponential decrease of the evanescent amplitude in the media n_2 with a *penetration depth* of

$$d_p = \frac{\lambda}{2\pi\sqrt{n_1^2\sin^2\theta - n_2^2}}. \tag{4.5}$$

The penetration depth expresses the values of z where the amplitude of the electric field E^i has reduced by a factor $1/e$. The variable d_p is independent of the polarization of the incident light and decreases with increasing θ. For instance, if $\lambda = 532$ nm, $n_1 = 1.5$ (glass), $n_2 = 1$ (air), the critical angle is $\theta_c = 41.8°$. By taking an angle of incidence of $\theta = 45°$, the penetration depth is $d_p = 239$ nm. For an incident angle of $\theta = 80°$, the penetration depth is $d_p = 78$ nm.

Figure 4.3 shows the amplitude of the exponentially decreasing evanescent electric field with increasing distance from the interface (in *TE*-mode and *TM*-mode).

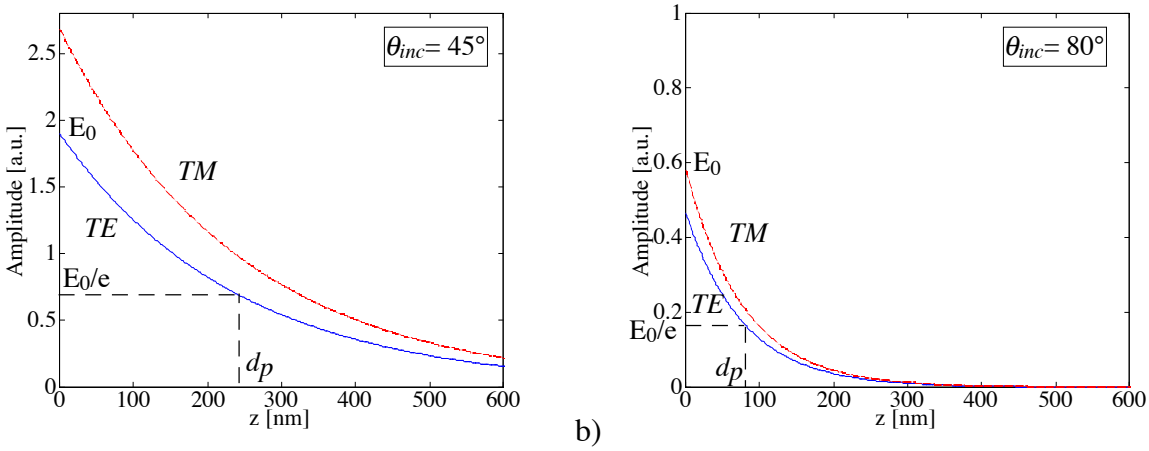

a) b)

***Figure 4.3**: TE-mode (plain curves) and TM-mode (dashed curves) of the amplitude of an evanescent wave for $\lambda = 532$ nm and $n = n_2/n_1 = 0.68$. **a)** $\theta = 45°$, $d_p = 239$ nm. **b)** $\theta = 80°$, $d_p = 78$ nm.*

4.1.2 Frustrated total reflection

The mean energy associated with an evanescent wave is given by the Poynting vector $\vec{S} = \vec{E} \times \vec{H}$. Energy flows in the x-direction, parallel to the surface, but not in the z-direction because the Poynting vector in z is imaginary [44]. To access this energy, it is necessary to transform one part of this evanescent wave into a propagating wave ($\vec{k}_t$) which is then detectable. Let us look at Fig. 4.4 to understand the transfer of the light to a third medium. The incident wave ($\vec{k}_i$) is totally internal reflected ($\vec{k}_r$) at the interface between the media n_1 and n_2. By approaching a third medium n_3 close to the surface, the evanescent wave is frustrated and a wave propagates into the third medium with a wave vector $\vec{k}_t$. This process is called *frustrated total reflection*. Newton made such an experiment by approaching a lens close to a prism. He observed that the area where the light was transmitted into the lens was larger than a simple contact point [46].

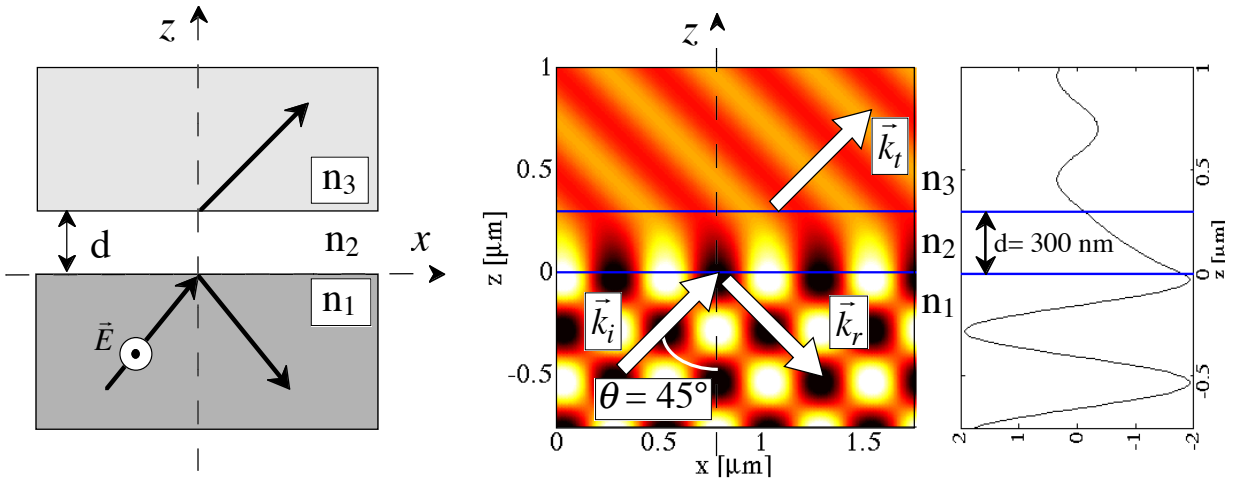

***Figure 4.4**: Total electric field of the frustrated total reflection process in TE-polarization. On the right, the profile in the z-direction is plotted. These calculations were carried out using the FMM (see chapter 6.1.3) method for $\lambda = 532$ nm , $\theta = 45°$, $n_1 = n_3 = 1.5$ and $n_2 = 1$.*

If we assume $n_1 = n_3$, the complex amplitudes E_3^s and E_3^p of the electric fields in the third medium at $z \geq d$ for *s*- and *p*-polarization respectively, are given by [46]

$$E_3^{s,p}(d) = \frac{\exp(in_1 k \cos\theta)}{\cosh \kappa d + iA_{s,p} \sinh \kappa d} E_1^{s,p}, \tag{4.6}$$

where $E_1^{s,p}$ are the incident amplitudes of the electric field, θ is the incident angle, $\kappa = 1/d_p$ and d is the distance between media 1 and 3. The factors $A_{s,p}$ are

$$A_s = \operatorname{cotan} 2\phi \tag{4.7}$$

for *s*-polarization, with

$$\tan\phi = \frac{\sqrt{n_1^2 \sin^2\theta - n_2^2}}{n_1 \cos\theta} \tag{4.8}$$

and

$$A_p = \operatorname{cotan} 2\Phi, \tag{4.9}$$

for *p*-polarization, where

$$\tan\Phi = \frac{n_1 \sqrt{n_1^2 \sin^2\theta - n_2^2}}{n_2^2 \cos\theta}. \tag{4.10}$$

From Eq. (4.6), the normalized electric field amplitudes in medium 3 are then given, for both polarizations, by

$$\left|E_3^{s,p}\right| \Big/ \left|E_1^{s,p}\right| = \frac{1}{\sqrt{\cosh^2 \kappa d + A_{s,p}^2 \sinh^2 \kappa d}}. \tag{4.11}$$

From Eq. (4.6) we also get

$$E_3^{s,p}(d) = \frac{\left[\cos\alpha\cosh\beta + A_s \sin\alpha \sinh\beta\right] + i\left[\sin\alpha\cosh\beta - A_s\cos\alpha\sinh\beta\right]}{\cosh^2\beta + A_{s,p}^2 \sinh^2\beta} E_1^{s,p}, \tag{4.12}$$

where $\alpha = n_1 k \cos\theta$ and $\beta = \kappa d$. From this equation, we can deduce the phase as

$$\tan\phi(d) = \mathrm{Im}\left\{E_3^{s,p}(d)\right\} \Big/ \mathrm{Re}\left\{E_3^{s,p}(d)\right\} = \frac{\sin\alpha\cosh\beta - A_s\cos\alpha\sinh\beta}{\cos\alpha\cosh\beta + A_s\sin\alpha\sinh\beta}. \tag{4.13}$$

The amplitude of the electric field at the interface between the air and the third medium depends on the wavelength λ, the thickness d of the second medium and the incident angle θ. The variation of the field with distance is no longer exponential as in the total internal reflection case (Fig. 4.5). This is due to coupling between the two media at small distances. The slope at the interface ($z = 0$) is zero.

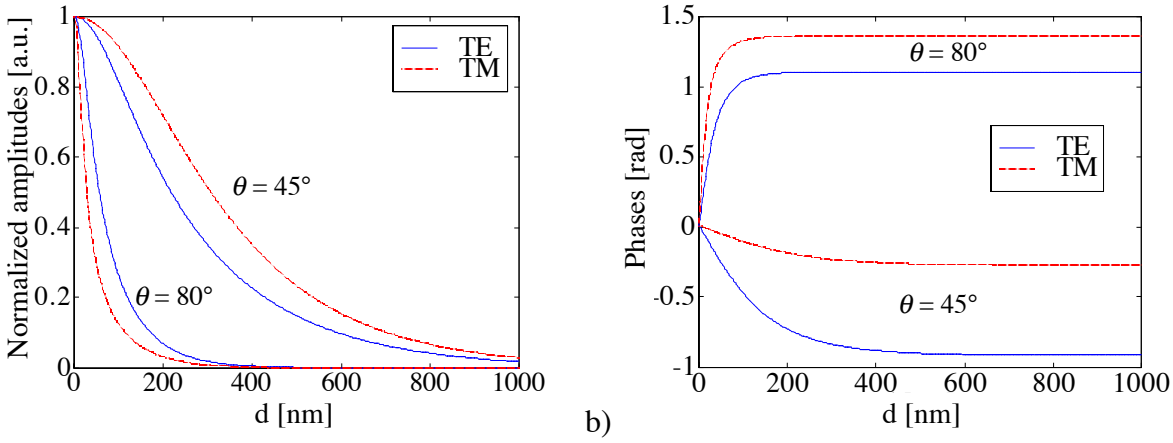

***Figure 4.5**: Frustrated total internal reflection **a)** amplitude and **b)** phase of TE-mode (plain curves) and TM-mode (dashed curves) for different incident angles ($\theta = 45°$ and $\theta = 80°$) and with $\lambda = 532$ nm, $n_1 = n_3 = 1.5$ and $n_2 = 1$.*

4.1.3 Frustrated total reflection in more complex systems

The most basic form of frustrated total reflection is based on three media only. Study of more complicated systems generally has to consider more media. In frustrated total reflection, the

frustrated light intensity in the third medium decreases with the distance between the media 1 and 3. If we put a fourth medium in the system, the behavior can be strongly perturbed. It has been shown that the frustrated intensity is a periodic function of the thickness of the second media [47].

If we consider a metallic layer (e.g. Chromium layer of 30 nm thickness, with a complex refractive index of $n_{Cr} = -12.3 + i24.5$ at $\lambda = 516.6$ nm [40]) at the surface of the third medium, a system with up to four different refractive indices is created. Figure 4.6 shows the frustration of the total internal reflection with four different media.

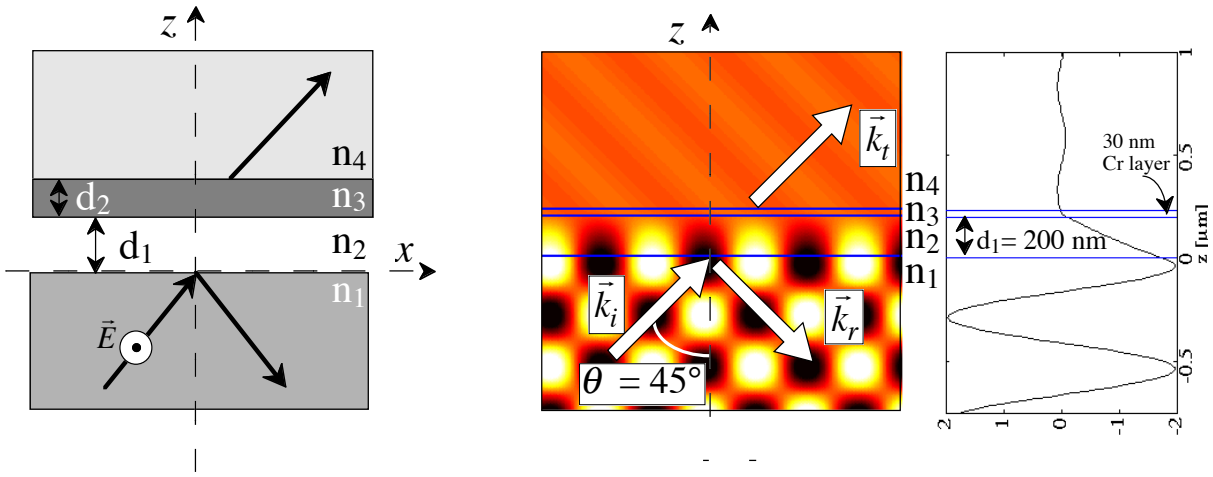

***Figure 4.6**: Optical tunneling effect in a four media system. Calculations have been made using the FMM model for $\lambda = 532$ nm, $\theta = 45°$, $n_1 = n_4 = 1.5$, $n_2 = 1$ and $n_3 = (-12.3 + i\,24.5)$.*

Even if the amplitude of the transmitted field in the fourth medium is weak, the evanescent wave is transmitted into a propagating wave in the last medium and becomes then detectable at large distances. The system can be extended to five media by coating the surface of the medium n_1 with another metal layer for instance.

In the special case where media 2 and 4 are the same, the maximum of the transmission in the last medium can be equal to 1 and does not necessarily correspond to a zero thickness of air (medium 2). The maximum of the transmission is a periodic function of the thickness of medium 2 and describes the system resonance [48].

4.2 Measurement of frustrated evanescent waves

In this section, we will present 1-D and 2-D measurements of the amplitude and phase of an evanescent wave produced by total internal reflection. Thanks to these measurements, we will

see the physical limitations of heterodyne detection. The amplitude of an evanescent wave decreases (quasi-) exponentially with increasing distance from the surface where the total internal reflection is produced. At large distances, the amplitude is very low (nearly zero). The limit to the detection of this low amplitude will give us the sensitivity of our detection system. The minimum detectable optical power is limited by the shot noise power (section 2.3), i.e. when the signal to noise ratio is equal to 1.

4.2.1 Set-up and measurements

The set-up for evanescent wave measurements is presented in Fig. 4.7a. From the illumination fiber, the light is collimated to a plane wave. The polarization of the light is controlled by a fiber polarization controller, a quarter waveplate and a Glan-Thomson polarizer. The evanescent wave is created by total internal reflection (TIR) in the prism. The entire optical system is mounted on a *x*-*y*-*z* translation stage (section 3.1). We illuminate the internal surface of a prism at an angle $\theta_1 > \theta_c = 41.5°$. The refractive index of the prism is $n_1 = 1.5$; $n_2 = 1$ is the refractive index of the air and n_3 is the refractive index of the tip ($n_3 = 1.5$ if the probe is a dielectric fiber tip).

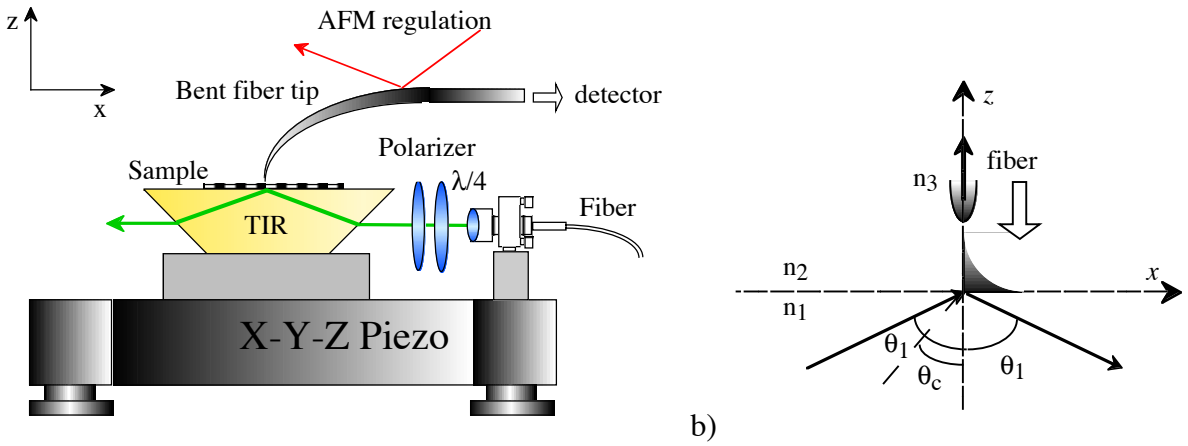

***Figure 4.7**: **a)** Set-up for evanescent wave measurements using total internal reflection in a prism. **b)** The fiber tip converts the evanescent wave into a propagating wave by photon tunneling.*

By approaching a fiber tip to the surface (Fig. 4.7b), the evanescent field is converted into a propagating wave in the fiber. Frustrated total internal reflection is concerned with a change of refractive index and occurs in PSTM by the introduction of a probe tip (medium n_3) close to the boundary. The distance dependence of the measured amplitude reveals the expected quasi-exponential decay of the evanescent wave (Fig. 4.8). Although the tip is modeled here by a semi-infinite plane (Figs 4.4 and 4.6), it yields, in spite of its simplicity, information on the distance effect of the evanescent field frustration. Thus, if the perturbation of the tip is week, the measured field is the evanescent field itself. The exponential curve agrees well with the theory.

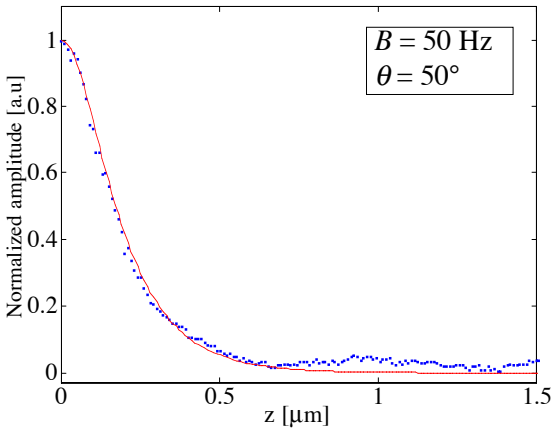

***Figure 4.8**: TE-polarized measured (dotted curve) and calculated (solid curve) amplitude of an optical evanescent wave versus the tip-surface distance (λ = 532 nm, θ_{inc} = 50°) on a linear scale.*

The situation in Fig. 4.7b is system with three media (Fig. 4.4) composed of a prism, air and fiber probe. By coating the tip with a metal layer for instance, it becomes a four media system (Fig. 4.6).

In order to have an idea of light magnitude detected, it is necessary to calibrate the voltage coming from the detector U_{in} into an absolute optical power P_o. In this case, we will see the quantitative limitation of optical power detection. In section 3.2.4, we presented the properties of the lock-in amplifier. We will show how the signal from the detector is processed through the lock-in amplifier (Fig. 4.9).

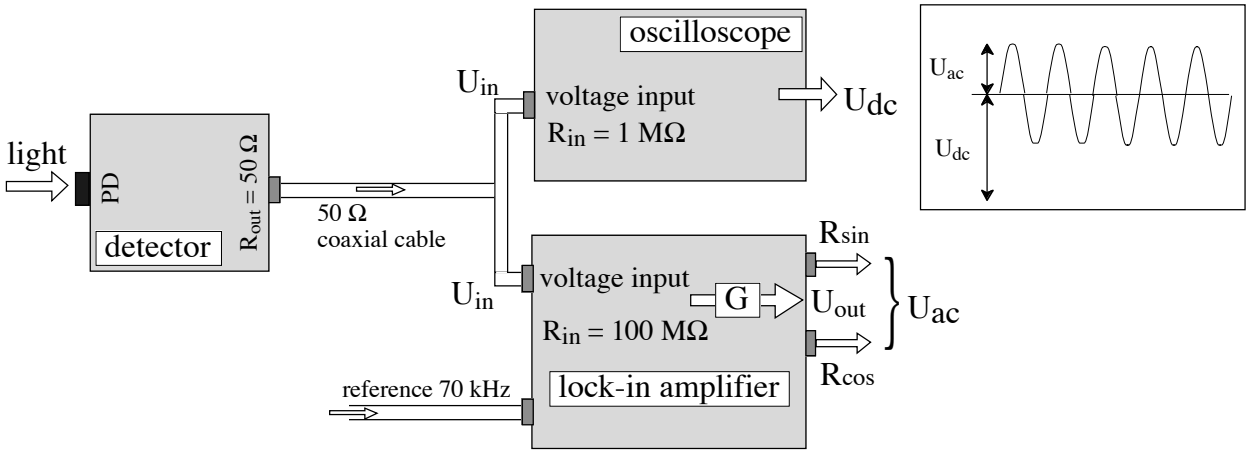

***Figure 4.9**: Detection scheme for the heterodyne signal from the detector, which is processed by the lock-in amplifier. The oscilloscope is used to measure the dc level.*

The signal at the output of the detector, as obtained from Eqs. (2.12) and (3.2), is a sinusoidal voltage

$$U(t) = U_{dc} + U_{ac}\cos(2\pi\Delta f t + \varphi) \tag{4.14}$$

composed of a dc offset

$$U_{dc} = SR_0\left(P_r + P_o\right) \tag{4.15}$$

and of an ac part with amplitude

$$U_{ac} = 2mSR_0\sqrt{P_r P_o}\,. \tag{4.16}$$

Since $P_r >> P_o$, the optical power P_r corresponding to the reference can be obtained from U_{dc}, measured with an oscilloscope (*Hewlet Packard, Model 54600A,* input impedance R_{in} = 1 MΩ).

The lock-in amplifier processes only the ac part of the signal. The two output signals of the lock-in amplifier ($R\cos\phi$ and $R\sin\phi$ of Fig. 4.9), measure directly the two quadrature components $U_{ac}\cos\varphi$ and $U_{ac}\sin\varphi$ in Eq. (4.14). These components contain all the information of the measured optical field.

From Eq. (4.16), we get the optical power corresponding to the field detected by the probe,

$$P_o = \frac{U_{ac}^2}{2m^2S^2R_0^2P_r} = \frac{U_{ac}^2}{2m^2SR_0U_r}, \tag{4.17}$$

where U_r is the dc voltage of the detector output measured for the optical power P_r of the reference and U_{ac}^2 is obtained from $\left(R\cos\phi\right)^2 + \left(R\sin\phi\right)^2$. As R_0 and S are known, assuming that m = 1 and measuring the voltage of the reference U_r, we get the conversion of the measured ac voltage amplitude into an optical power. It is interesting to see that Eq. (4.17) is independent of the load impedance R_L and the post-detection bandwidth B. For the following experiments, the measured U_{ac} has been converted into the optical power collected by the tip using Eq. (4.17) with $U_r = 1.3$ V, $R_0 = 470$ kΩ, $S = 0.33$ A/W and $m = 1$. The integration time τ of the lock-in amplifier has been chosen to be $\tau = 10$ ms. The corresponding post-detection bandwidth is therefore $B = (2\tau)^{-1} = 50$ Hz.

The theoretical prediction of the frustrated total reflection (Eq. (4.11)) and the measurements are shown in Fig. 4.8 on a linear scale. In Fig. 4.10, the corresponding optical power of the measured amplitude is plotted on a logarithmic scale to view better the variations at low level. The theoretical limit of detection, given by the shot noise of P_o, (Eq. (2.22)), is $P_o^{\min} = 2.7\cdot10^{-17}$ W (for $\lambda = 532$ nm, $B = 50$ Hz, $\eta = 0.7$).

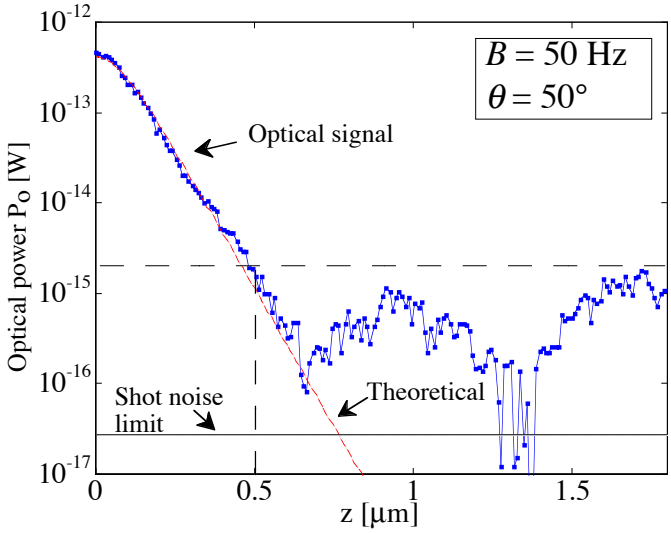

***Figure 4.10**: TE-polarized measured (dotted curve) and calculated (dashed curve) power (P_o) of an optical evanescent wave versus the tip-surface distance (λ = 532 nm, θ_{inc} = 50°) on a logarithmic scale.*

The angle of incidence is $\theta = 50°$ and thus the penetration depth is $d_p =$ 150 nm. We can see the very good agreement of the measurement with the theory up to a distance of about 600 nm from the surface. Theoretically, the distance limit (intersection of the theoretical curve and the shot noise limit), where the evanescent would be detectable, is 700 nm. The signal after this limit should be at the noise level. However, the detected signal beyond this distance does not only result from the evanescent wave. In fact, there is an optical background due to another light source. This undesirable background signal arises from scattered light at the surface (surface defects, dust, etc). This optical background is superposed on the evanescent wave. The maximal level of the scattered light seems to be at about $P_o = 2 \cdot 10^{-15}$ W, which corresponds to the power of evanescent field at z = 500 nm. However, it should be noted that the dynamic range of the measured optical power is about 10^4. From Eq. (2.18), the corresponding SNR is about 19 dB (for $B = 50$ Hz).

The phase of the frustrated evanescent wave is shown in Fig. 4.11. The incident angle is $\theta_{inc} = 50°$. For an angle of incidence of $\theta_{inc} = 57.8°$ the slope of the phase would be constant. We can see a good agreement of the experimental data with the theoretical curve given by Eq. (4.13). The absolute value of z and the measured phase offset have been adapted to fit best the theoretical and the experimental results.

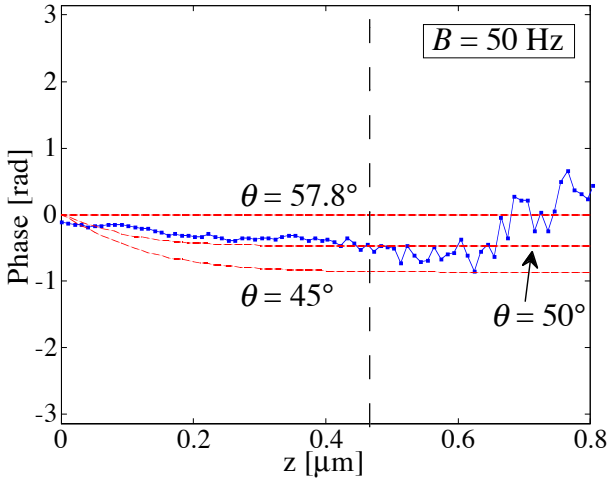

***Figure 4.11**: TE-mode measured (dotted curve) and calculated (dashed curves) phase of an evanescent frustrated wave versus the tip-surface distance (λ = 532 nm, θ_{inc} = 50°).*

First, we showed that the measured signal from the evanescent field is corrupted by scattered light beyond a distance of 500 nm. We can see in Fig. 4.11 that the phase accuracy decreases also beyond 500 nm. From Eq. (2.21), the standard deviation of the phase is $\delta\varphi = 1/\sqrt{SNR}$, which yields $\delta\varphi = 6.6°$ for SNR = 19 dB at this point. The SNR of the maximum detected power of $P_o = 4.6 \cdot 10^{-13}$ W is 42 dB, yielding $\delta\varphi = 0.4°$.

4.2.2 Lower limit of signal detection

The aim of this section is to demonstrate the sensitivity of heterodyne detection. Figure 4.12 shows the results for evanescent waves measured with two different illumination intensities, with a ratio of 20 dB. The angle of incidence is $\theta_{inc} = 59°$. The curve for the lower intensity is obtained by inserting a ND (neutral density) filter in the illumination beam. The relation between the object power and the signal to noise ratio is given by Eq. (2.18). Theoretically, the minimum detectable optical power is $P_o^{\min} = 2.7 \cdot 10^{-17}$ W for B = 50 Hz (Eq. (2.22)), in both cases.

The experimental data of the evanescent wave amplitude follows the theoretical curves, taken from Eq. (4.11). At distances larger than 400 nm for the higher power and 180 nm for the lower power, an undesirable background signal is detected because of scattered light at the surface. This background noise is clearly optical. Indeed, for the lower power, the background is also reduced, disappearing into the shot noise.

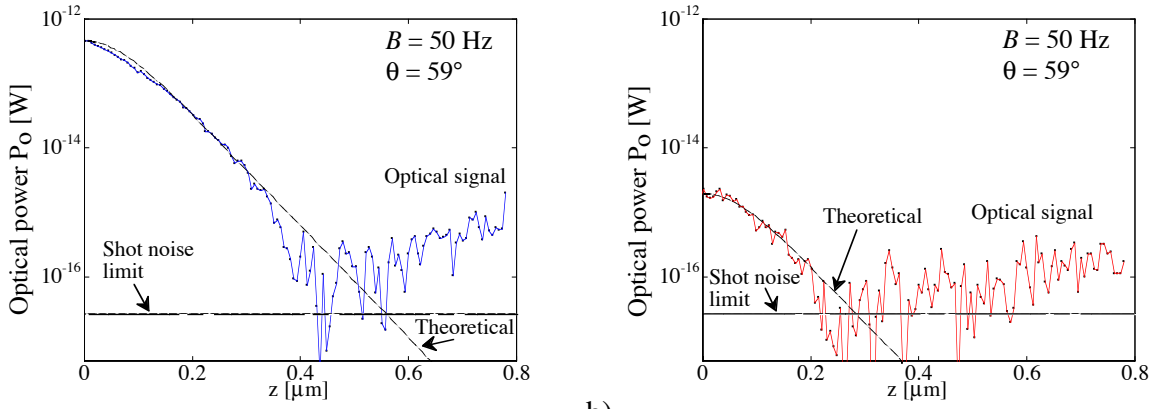

***Figure 4.12**: Two (TE-mode) evanescent wave measurements with different incoming light intensities (ratio about 20 dB). The angle of incidence is $\theta_{inc} = 59°$ and the bandwidth is B = 50 Hz.*

For comparison, in the case of direct detection (without reference), the signal to noise ratio is limited by the Johnson noise. The minimum detectable optical power (SNR = 1 in Eq. (4.18)), with the same detector of Fig. 3.5, would be

$$P_o^{\min} = \frac{i_o^{\min}}{S} = \frac{\sqrt{4kTB/R_0}}{S}. \tag{4.18}$$

With $B = 50$ Hz, $R_0 = 470$ kΩ, $S = 0.33$ A/W and T = 300 K, the minimum optical power detectable without heterodyne detection is thus only $P_o^{\min} = 4 \cdot 10^{-12}$ W, instead of $P_o^{\min} = 2.7 \cdot 10^{-17}$ W with heterodyne detection. In a direct measurement, a photomultiplier or an avalanche photodetector would therefore be more suitable, even with a smaller quantum efficiency η.

4.2.3 2-D evanescent field measurement

We have presented one-dimensional curves of the evanescent field. It is interesting to investigate now two-dimensional plots of such fields by using the same set-up as in Fig. 4.7a. Indeed, we will demonstrate that the low-level background noise is really optical and is due to scattering points at the surface. We can eliminate the field due to the scattering effects from the evanescent field [49] for better image interpretation. By scanning the surface in the X-Z plane we get a mapping of the field above the surface. The angle of incidence, $\theta = 43°$ (close to the critical angle $\theta_c = 41.8°$), is smaller than in the previous measurements of Figs 4.10 and 4.11. The penetration depth, $d_p = 392$ nm, is therefore larger, allowing the evanescent field to be detected up to large distances. Figure 4.13a shows the 2-D amplitude, and Fig. 4.13b a 1-D phase

cross-section measurement of the evanescent wave amplitude and power, respectively. In this case, background light perturbation is not observed.

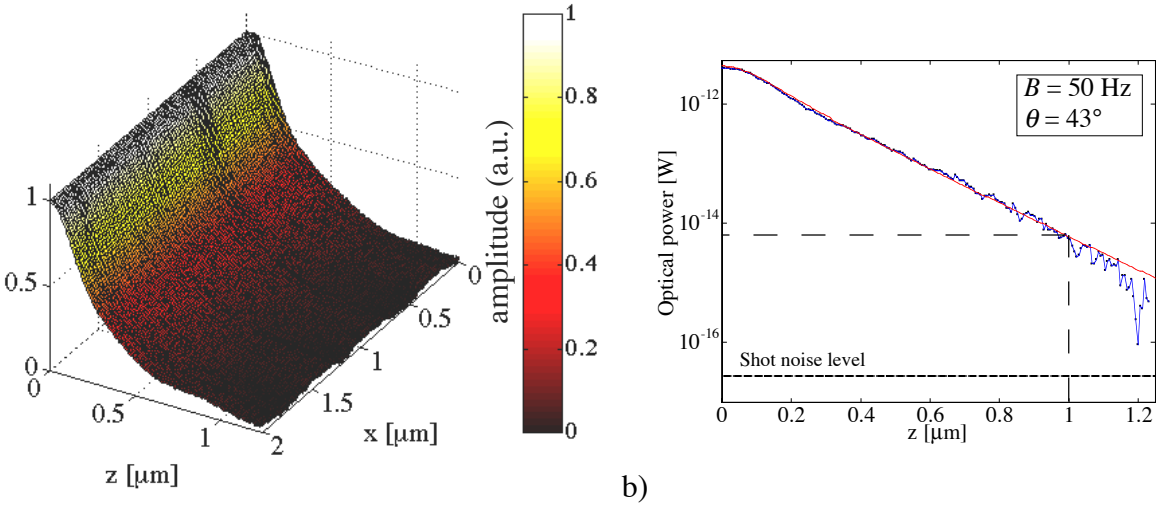

a) b)

***Figure 4.13**: **a)** 2-D amplitude measurement of the evanescent wave. **b)** Corresponding 1-D optical power (dotted curve) and calculated power (solid curve) with λ = 532 nm and θ_{inc} = 43° in logarithmic scale.*

The measured phase is presented in Fig. 4.14a as an iso-phase contour plot. The wavevector $\vec{k}$ only has a component $\vec{k}_x$ in the *x*-direction. Thus, the measured phase is the evanescent component of the field. Two "bold" lines of the phase contour plot are separated by 2π, corresponding to $\Lambda = \lambda/n\sin(\theta) \cong 520$ nm. However, the measurement accuracy in the *x*-direction is not very high, because the scans with the probe were done in the *z*-direction in order to get precise measurements of the optical power as a function of *z*. The steps in *x* are 20 nm and displacement errors may be accumulated after each step. At 1 µm above the surface, the evanescent wave can still be measured with an SNR of 23 dB (corresponding to an optical power of 6 fW for *B* = 50 Hz) and thus with a phase resolution of 3.8°. Beyond this limit, the phase is strongly perturbed because of noise; the limit of signal detection is reached.

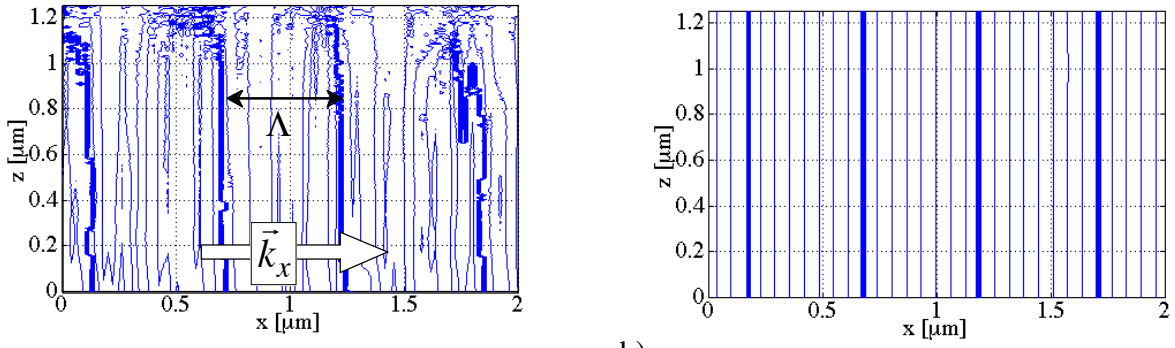

a) b)

***Figure 4.14**: Iso-phase contour plot of an evanescent phase **a)** measured and **b)** calculated with FMM. Two "bold" lines are separated by 2π, corresponding to $\Lambda \approx 520$ nm. The wavevector $\vec{k}$ has only one component, in the x-direction.*

A measurement revealing otherwise well-distinguished scattering points is presented in Fig. 4.15. The surface of the glass sample had been made deliberately dirty. We can see the evanescent field (with a wavevector $\vec{k}_x$) mixed with a propagating field ($\vec{k}_t$), produced by scattering points. Detection is possible up to 3 µm above the surface. The influence of the scattered light becomes visible at about 500 nm above the surface. Above 1 µm it completely obscures the evanescent wave field.

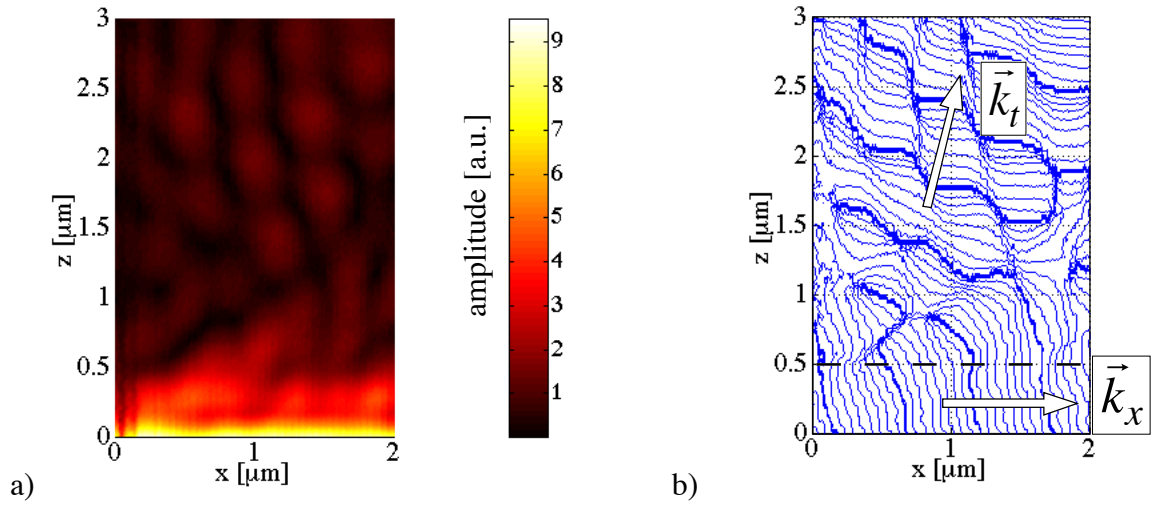

***Figure 4.15**: **a)** Amplitude and **b)** phase (iso-phase contour plot) of an evanescent wave field mixed with scattered light.*

Another measurement of scattered light is shown in Fig. 4.16. Here the scattering is due to surface defects and not by dust. The evanescent wave field is already completely disturbed at the surface of the prism.

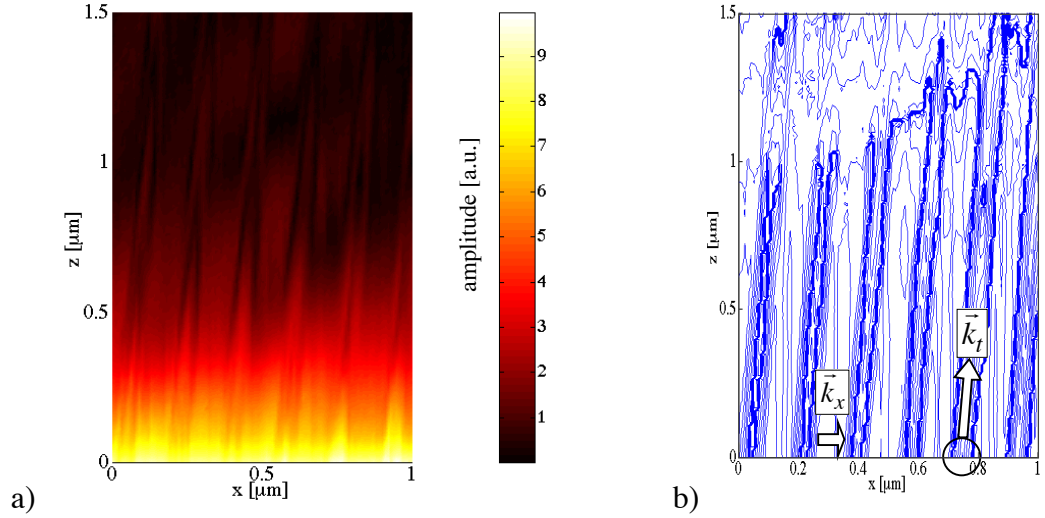

***Figure 4.16**: **a)** Amplitude and **b)** phase (iso-phase contour plot) of an evanescent field mixed with scattered light (surface defects, as indicated by the circle).*

4.2.4 Water meniscus formation between the tip and the sample surface

When the tip is brought close to the sample surface, some interactions have to be taken into consideration. In addition to van der Waals interaction between the tip and the sample at nanometric distances, one can be confronted with other forces such as Coulombian or capillary forces [33]. When contact between the tip and sample is made, a friction force results. If we work in a liquid medium, viscosity forces have also to be considered. The van der Vaals forces are useful for the AFM approach mechanism. Coulombian forces are pure electromagnetic interactions. As we have not worked in a liquid medium, the viscosity forces are negligible. One interaction that has been observed is the formation of a water meniscus between the tip and the surface, caused by capillary forces. Experimental measurement reveals this effect.

In a relatively humid ambient environment, water condensation leads to the formation of a thin water layer both on the tip and the sample surfaces [50, 51]. A water meniscus is formed when the tip is close to the sample. The capillary force arises by decreasing the tip-surface distance and can apply strong attractive forces that hold the tip in contact with the surface. This effect is demonstrated in the following by experimental observations.

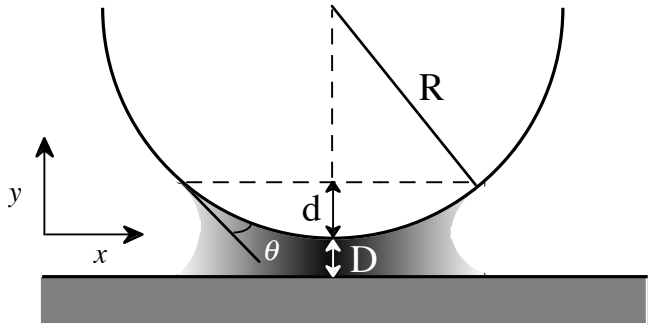

***Figure 4.17**: Water meniscus formation. The tip apex is modeled by a sphere.*

In addition to relative humidity, the meniscus formation depends strongly on the hydrophility of the tip as well as the sample. For the geometrical considerations of Fig. 4.17 (i.e. by approximating the tip apex by a sphere), the attractive capillary force between the sphere and the surface due to the liquid is given by [33]:

$$\left|F_{cap}\right| = \frac{4\pi R\gamma_L \cos\theta}{1+D/d}, \tag{4.19}$$

where γ_L is the specific surface energy of the liquid, θ is the contact angle between the tangent to the sphere and the meniscus, d is the sphere penetration depth into the water layer and D is the sphere-surface distance. The capillary force is vertical.

The strength of the capillary force has been estimated taking into account the corresponding values for surface energy of water $\gamma_L = 72$ mJ/m^2 [33], a tip apex radius of $R = 50$ nm and tip-sample distances of $D = 10$ nm and 50 nm. The penetration depth of the sphere into the liquid has been estimated to be $d = 15$ nm ($d \approx R - R/\sqrt{2}$) and the contact angle equal to $\theta = 10°$. The contribution of the capillary force in air, when the tip approaches a glass substrate can be thus estimated to $|F_{cap}| = 10^{-8}$ N for $D = 50$ nm and $|F_{cap}| = 2.7 \cdot 10^{-8}$ N for $D = 10$ nm.

With the same set-up as in section 4.2, we measure an evanescent wave by frustrated total internal reflection (Fig. 4.7) in a prism ($n_{prism} = 1.5$). The incident angle is $\theta = 73°$. The mechanical movement of the tip and the optical signal are shown in Fig. 4.18.

As the tip is far from the surface, the optical signal is low (Fig. 4.18/1). When the tip is moved towards the surface, light is coupled into the fiber by photon tunneling and the optical signal begins rising exponentially (Fig. 4.18/2). The medium between the prism and the probe is air. When the surface-tip distance becomes smaller ($z = 50$ nm from the surface), the humidity produces a water particle aggregation around the tip, forming a meniscus between the tip and the surface (Fig. 4.18/3). This causes an abrupt attraction of the tip and a corresponding cantilever deformation. In fact, at $D = 50$ nm, the capillary force is about 10^{-8} N. With a fiber cantilever force constant of about 4 N/m (section 3.2.3), the deformation (in the z-direction) of the cantilever is about 25 nm. As the tip-surface distance becomes smaller, because of this deformation, the optical signal increases (Fig. 4.18/3). However, this is not the only explanation. In fact, the water meniscus causes a change of refractive index of the medium between the prism and the probe. The refractive index of air ($n_{air} = 1$) is replaced by the refractive index of water ($n_{water} = 1.3$) in Eq. (4.11) for the frustrated total internal reflection. The change of refractive index from 1 (air) to 1.3 (water) results in a modification of the coupling into the fiber probe. The theoretical consequence of the refractive index change is shown in Fig. 4.18 (dashed curve). Due to the water meniscus, the optical signal increases then drastically (Fig. 4.18/3). It is interesting to observe that the theoretical curve (Eq. (4.11) for $n_{water} = 1.3$) passes through the maximum of the discontinuity at $z = 50$ nm. This strengthens the theory of water meniscus formation.

By continuing the approach, the tip makes the meniscus break up (Fig. 4.18/4) because of pressure and the signal decreases abruptly. Indeed, the medium between the surface and the tip is air again. Then, the coupled light follows again the theoretical curve (Eq. (4.11)) for $n_{air} = 1$.

In order to avoid this perturbation of the measurements, we have to control the humidity. We have built a plexiglas box around our experimental set-up (Fig. 3.3), enclosing the SNOM (tip and sample). Silica gel is placed inside the box to reduce the humidity.

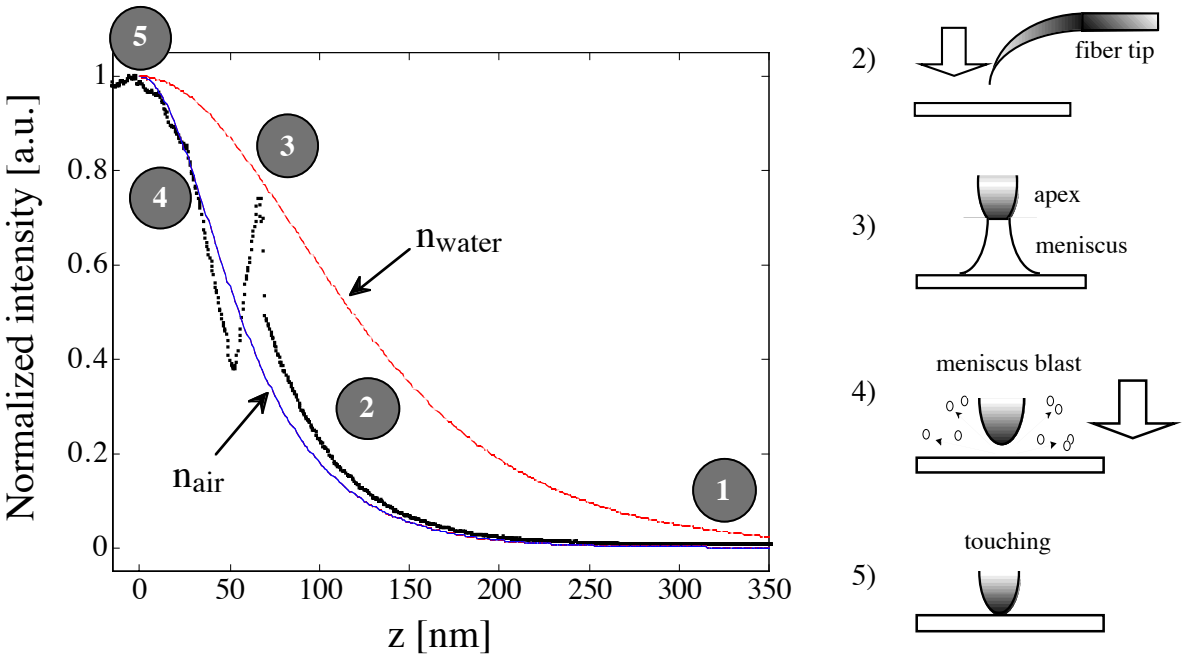

***Figure 4.18**: Measured optical intensity (dotted curve) of an evanescent wave with the formation of a discontinuity (z = 50 nm) due to a water meniscus. The curves show the calculated values of Eq. (4.11) with $\theta = 73°$, $n_1 = 1.5$, $n_2 = 1$ (solid line) and $n_2 = 1.3$ (dashed line), respectively.*

4.3 Conclusion

Total internal reflection of a plane wave at the interface of two materials with different refractive indices has been investigated. By total internal reflection at the prism interface, we produced an evanescent wave. To get information about the evanescent field, the system has to be perturbed. The easiest way to perturb the evanescent field is to approach a third medium in order to frustrate the total reflection. Frustrated total internal reflection induces coupling between the different media. A simple model, replacing the probe tip by a homogeneous plane, describes the behavior of the frustration of total internal reflection by the probe quite well. Frustrated total internal reflection mechanism is equivalent to photon tunneling. Indeed, this process is similar to electron tunneling in a STM (Scanning Tunneling Microscope). The concept is the same, except that we are confronted with photons instead of electrons. Photon tunneling is the key to understanding the concept of the PSTM.

We have measured amplitude and phase of an evanescent field using heterodyne detection. We have obtained very good agreement with theory by simple semi-infinite plane model for the tip coupling. The evanescent wave measurements allow also demonstration of the large dynamic range of heterodyne detection. In fact, the ratio between the maximum and the minimum detected optical power was in the presented measurements about 10^4. The minimum detectable

optical power (shot noise level) is $P_o^{\min} = 2.7 \cdot 10^{-17}$ W ($B = 50$ Hz) for heterodyne detection, compared to $4 \cdot 10^{-12}$ W for direct detection with the same photodiode as detector. Heterodyne detection also allows measurement of the phase with sub-wavelength resolution. For an optical power of $P_o = 4.6 \cdot 10^{-13}$ W, we get a noise limit for the phase resolution of $\delta\varphi = 0.4°$.

However, it has been shown that the detection of evanescent fields may be corrupted by light scattered at the surface from defects or dust. 2-D scans allow us to better observe this phenomenon and to determine the position of the sources of the scatters.

It has also been shown, that humidity may cause the formation of a water meniscus between the tip and the surface, which perturbs the measurements of evanescent fields drastically.

5 Amplitude and phase of an evanescent standing wave

After the study of an evanescent wave, we are now interested in another simple case: the evanescent standing wave. This phenomenon has already been studied [52], but only by intensity measurements. However, the phase measurements which we are presenting here allow us to experimentally determine more features of the optical field [19, 53]. At the surface of a prism, we create an evanescent standing wave by the interference of two total internally reflected plane waves traveling in opposite directions. The evanescent standing wave is simply a standing wave with a sinusoidal intensity variation in the x-direction and with an exponential decay in the z-direction. The study of this wave is interesting, because it is one of the easiest non-topographical "structures" we can measure. So, no artifact due to the surface shape occurs during the measurement, because the prism surface is flat. The shape of the measured amplitude and phase of the evanescent standing wave give us information about features such as the power loss of the back-reflected wave and the angle of the incident beams. We report amplitude and phase measurements with very high spatial resolution, showing that the resolution is not limited by the finite dimensions of the tip.

5.1 Two-wave interference at an interface

Near-field amplitude and phase measurements of a standing evanescent wave field on a prism have been made and are presented in this chapter. After a first total internal reflection in a prism (with an angle θ_1), the beam is reflected back by an external mirror, creating a standing wave. The illumination system of Fig. 5.1 is combined with the set-up of Fig. 3.1. In this set-up, the prism and the mirror are in a fixed position whereas the tip scans in the XY plane (parallel to the surface). The approach of the tip is done by use of atomic force microscope regulation (see section 3.2.3). When the tip is close to the surface, the feedback of the AFM is switched off and the scan at constant height can be executed.

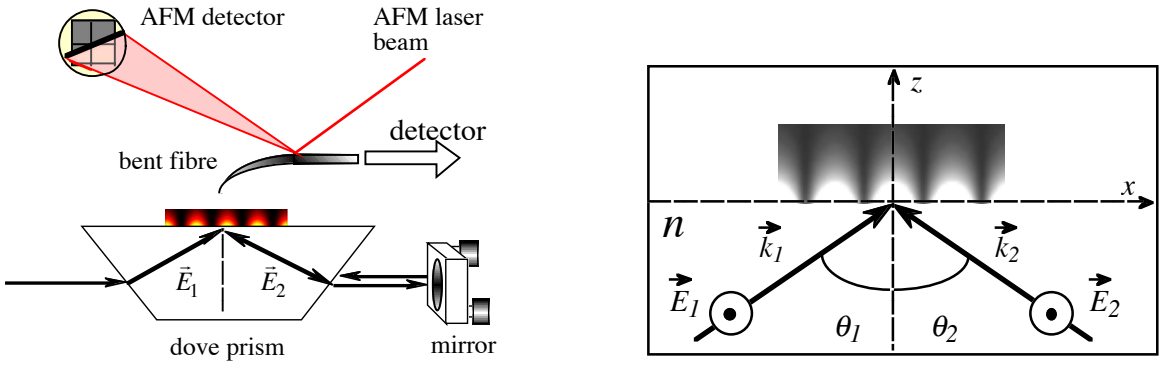

***Figure 5.1**: Standing evanescent wave **a)** set-up for SNOM measurement, **b)** creation by total internal reflection at the interface of the prism.*

The total electric field of the interfering beams in Fig. 5.1a is

$$\vec{E} = \vec{E}_1 + \vec{E}_2. \tag{5.1}$$

In the case of TE polarization, the evanescent standing wave field is given by

$$E_y(x,z) = E_1 \exp[-inkx\sin\theta_1]\exp(-z/z_1) + E_2 \exp[inkx\sin\theta_2 + i\varphi]\exp(-z/z_2), \tag{5.2}$$

where $k = 2\pi/\lambda$ is the wavenumber, n is the refractive index of the prism, E_1 and E_2 are the electric field amplitudes of the two incident waves, φ is the phase shift of $\vec{E}_2$, and $z_1(\theta_1)$ and $z_2(\theta_2)$ are the penetration depths (Eq. 4.5) of the corresponding evanescent waves. By introducing the ratio $m = E_2/E_1$ (with $m \le 1$) of the incident-field amplitudes and $\alpha_{1,2} = nk\sin(\theta_{1,2})$, we get from Eq. (5.2):

$$\begin{aligned} E_y(x,z)/E_1 &= \exp[-i\alpha_1 x]\exp(-z/z_1) + m\exp[i\alpha_2 x + i\varphi]\exp(-z/z_2) \\ &= A(x,z)\exp[i\phi(x,z)] \end{aligned}, \tag{5.3}$$

where $A(x,z)$ is the real amplitude and $\phi(x,z)$ the phase, with

$$\begin{aligned} A(x,z) = \{&[\exp(-i\alpha_1 x)\exp(-z/z_1) + m\exp(i\alpha_2 x + i\varphi)\exp(-z/z_2)] \\ &\cdot [\exp(i\alpha_1 x)\exp(-z/z_1) + m\exp(-i\alpha_2 x - i\varphi)\exp(-z/z_2)]\}^{1/2}. \end{aligned} \tag{5.4}$$

Finally, in the general case (where m < 1 and $\theta_1 \neq \theta_2$) the amplitude becomes

$$\begin{aligned} A(x,z) = &[\exp(-2z/z_1) + m^2\exp(-2z/z_2) \\ &+ 2m\exp[-z(1/z_1 + 1/z_2)]\cos((\alpha_1 + \alpha_2)x + \varphi)]^{1/2} \end{aligned} \tag{5.5}$$

and the phase

$$\phi(\mathrm{x},\mathrm{z}) = \arctan\left[\frac{m\exp(-z/z_2)\sin(\alpha_2 x + \varphi) - \exp(-z/z_1)\sin(\alpha_1 x)}{\exp(-z/z_1)\cos(\alpha_1 x) + m\exp(-z/z_2)\cos(\alpha_2 x + \varphi)}\right] . \qquad (5.6)$$

From Eqs. (5.5) and (5.6), we distinguish four cases (Fig. 5.2):

Fig. 5.2a) m = 1 and $\theta_1 = \theta_2 = \theta$,

Fig. 5.2b) m = 1 and $\theta_1 \neq \theta_2$,

Fig. 5.2c) m ≠ 1 and $\theta_1 = \theta_2 = \theta$,

Fig. 5.2d) m ≠ 1 and $\theta_1 \neq \theta_2$.

Numerical examples for amplitude and phase at constant height (z = const) are shown in Fig. 5.2.

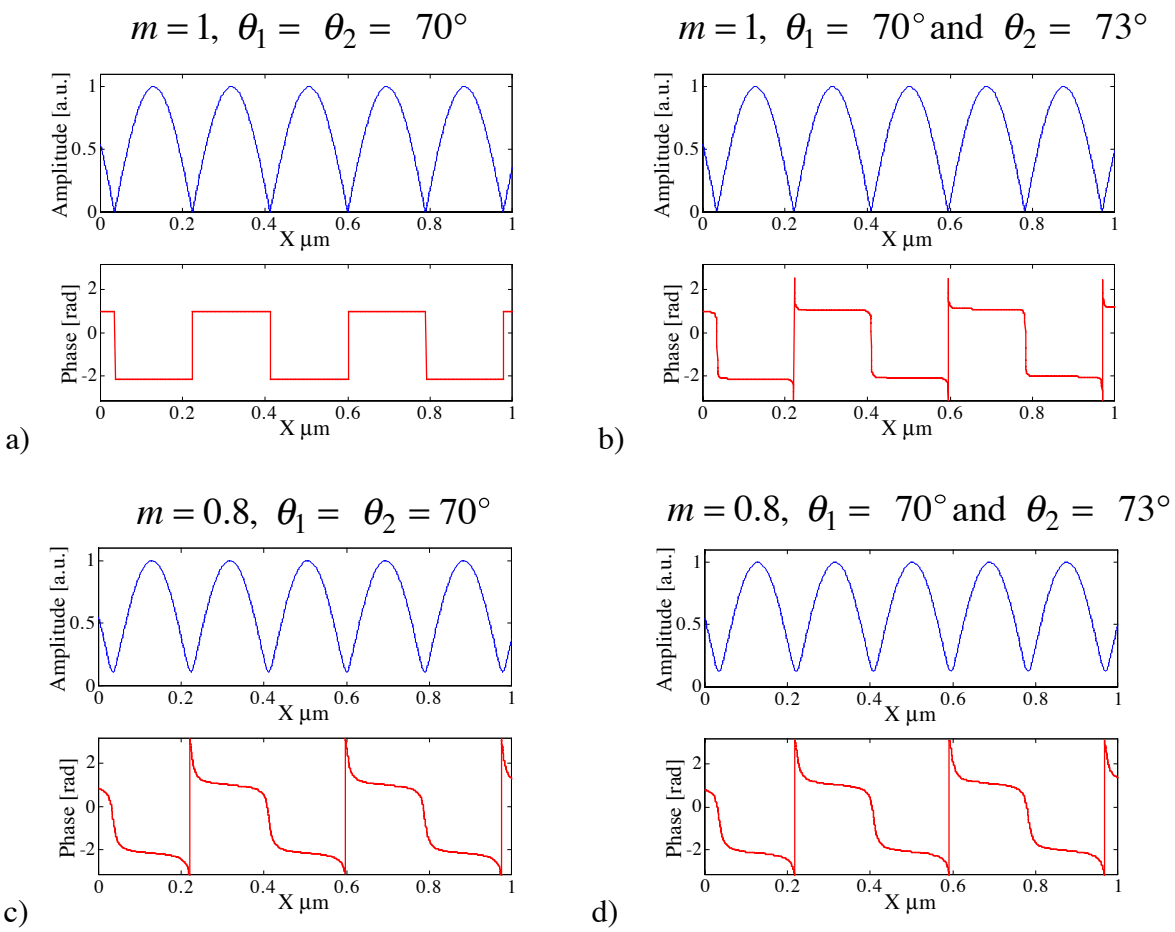

Figure 5.2*: Numerical examples for amplitude and phase of evanescent standing waves at constant height (z = const).*

The cases of Figs. 5.2a and 5.2b are impossible in practice, because we always have less than 100% of reflectivity for the back-reflected wave E_2, so that $E_2 < E_1$.

Let us examine the case of Fig. 5.2c, where m < 1 and $\theta_1 = \theta_2 = \theta$ ($\Rightarrow z_1 = z_2 = z_0$). We get from Eq. (5.5) and from $\alpha_1 = \alpha_2 = \alpha = nk\sin\theta$ the period of the standing wave

$$\Lambda = \frac{\lambda}{2n\sin\theta}. \tag{5.7}$$

In this case, the amplitude $A(\mathbf{x})$ and the phase $\phi(\mathbf{x})$ of the sampled field become

$$A(\mathbf{x}) = A_0 e^{-z/z_0}\sqrt{1+m^2+2m\cos(2\pi/\Lambda\, x+\ \varphi)}\,, \text{ and} \tag{5.8}$$

$$\phi(\mathbf{x}) = \arctan\left[\frac{m\sin(nkx\sin\theta\ +\varphi)-\sin(nkx\sin\theta)}{\cos(nkx\sin\theta)+m\cos(nkx\sin\theta\ +\varphi)}\right]. \tag{5.9}$$

For a phase shift of $\varphi = 0$, the phase becomes

$$\phi(\mathbf{x}) = \arctan\left[\frac{m-1}{m+1}\tan(nkx\sin\theta)\right]. \tag{5.10}$$

5.2 Amplitude and phase measurement of an evanescent standing wave

After approaching the fiber with a conventional atomic-force microscope regulated approach, we scanned across the prism surface at constant height (z = const). By scanning across the prism surface on an area of 1 µm by 1 µm in the X-Y plane, we acquired the amplitude and the phase of the optical field (in *TE*-illumination), as shown in Fig. 5.3. The period was found to be Λ = 185 nm. With λ = 532 nm and n = 1.5 we get from Eq. (5.5) an incident angle of θ = 73°, which corresponds with the experimental setup.

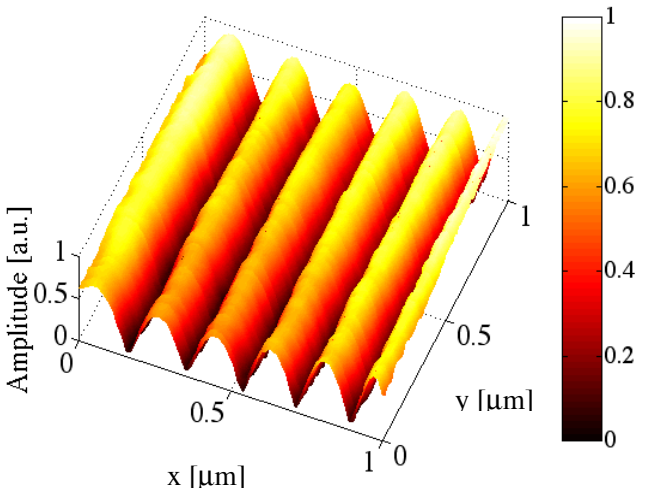

a)

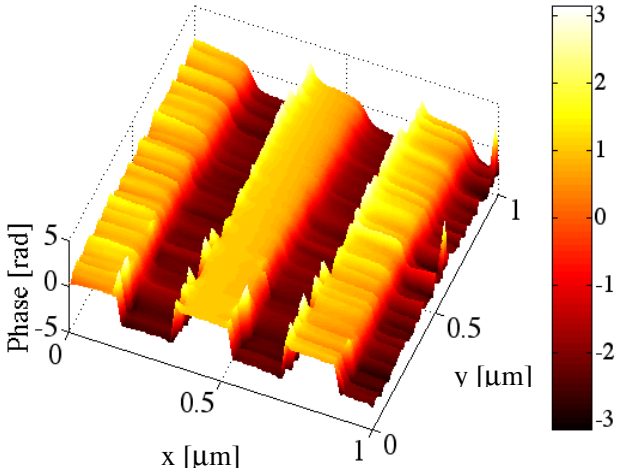

b)

***Figure 5.3**: Measured **a)** amplitude and **b)** phase of a standing evanescent wave at constant height (z = const). The scan area is 1 µm by 1 µm.*

A cross section of another separate measurement in the *x*-direction is shown in Fig. 5.4. The phase shows the expected π-phase changes for each period of the standing wave, with a spatial resolution of 7.8 nm between sample points. The 2π-phase jumps are due to phase wrapping. We found a good agreement with theoretical values obtained from Eqs. (5.5) and (5.6) with $m = 0.7$ and $\theta_1 = \theta_2 = 73°$.

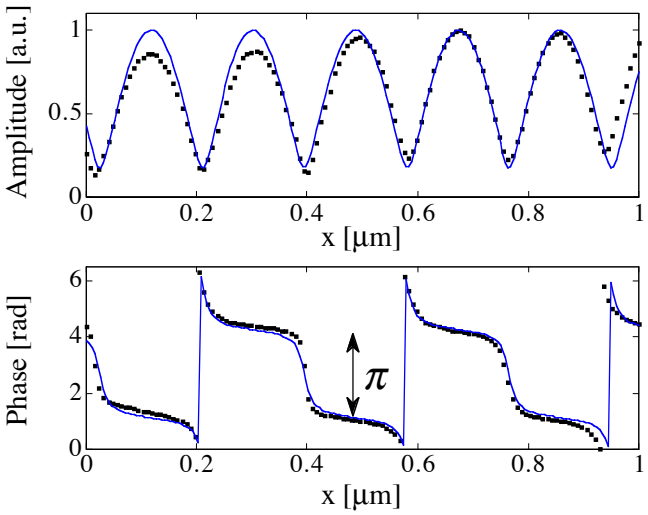

***Figure 5.4**: Cross-section of the measured (upper) amplitude and (lower) phase of the standing evanescent wave. The step is 7.8 nm between sampling points. The solid curves are theoretical calculations ($m = 0.7$, $\theta_1 = \theta_2 = 73°$).*

Figure 5.5 shows another separate measurement with a step of 1.6 nm between sampling points. We can see that the spatial resolution for amplitude and phase is given by the sampling steps of 1.6 nm. The measured values correspond very well to the calculations obtained from Eqs. (5.5) and (5.6) with $\theta_1 = \theta_2 = 73°$ and $m = 0.78$, which means that the intensity of the

backward wave is only about ~60% of that of the forward wave. Although the intensity does not go to zero at the nodes of the standing wave, the transition of the phase is very steep (~0.13 rad/nm) around these points, as expected from Eq. (5.6). Unlike intensity measurements, in coherent detection, the finite width of the fiber tip (~30 nm in our case) averages the field amplitude rather than the intensity, and therefore for $m = 1$ the measured amplitude would go to zero even for a finite tip size.

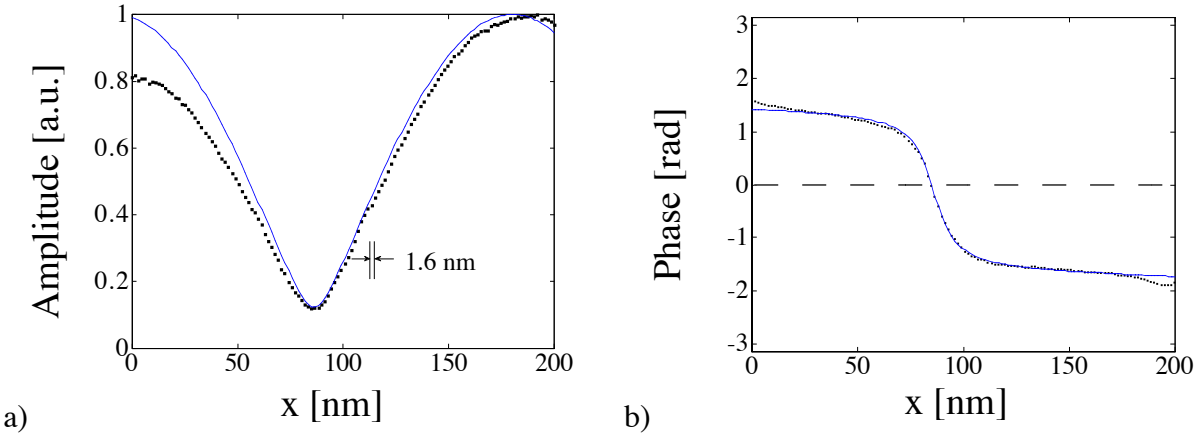

***Figure 5.5**: Measured standing evanescent wave with a step of 1.6 nm between sampling points. The scan length is 200 nm. The solid curves are theoretical calculations with $\theta_1 = \theta_2 = 73°$ and $m = 0.78$. **a)** Normalized amplitude and **b)** phase (in rad).*

By zooming into the region (from 50 to 120 nm) where the amplitude is a minimum, we get the Fig. 5.6. Moreover, in Fig. 5.6a, we have changed the scale from the amplitude into the absolute optical power (on a logarithmic scale) using Eq. (4.17) (with $U_r = 1.1$ V, $S = 0.33$ A/W, $R_0 = 470$ kΩ and assuming that $m = 1$). The measured minimum power is $P_o^{\min} = 2 \cdot 10^{-13}$ W. From Eq. (2.18), the signal to noise ratio, corresponding to this optical power, is about 43 dB (with $\lambda = 532$ nm, $\eta = 0.7$ and $B = 16.67$ Hz for an integration time of $\tau_{in} = 30$ ms). Figure 5.6 reveals the high-resolution of the amplitude and phase measurement. At $x = 85$ nm, the normalized intensity is reduced by 99% and the visibility is only $\Gamma = 1\%$ (Eq. 3.18). At the nodes of the standing wave, we do not have a crossing through zero but the intensity is considerably reduced. From Eq. (2.21), the phase accuracy at the minimum amplitude is still $\Delta\varphi = 0.4°$.

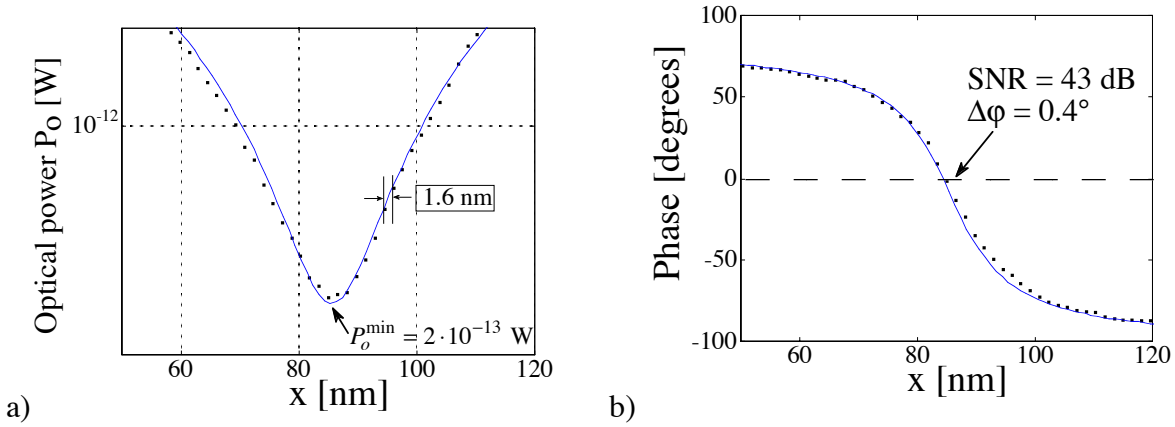

***Figure 5.6**: Measured **a)** optical power (on a logarithmic scale) and **b)** phase (in degrees) of the standing evanescent wave (zoom of Fig. 5.5). The minimum corresponds to a power of $P_o = 2 \cdot 10^{-13}$ W. The SNR at this point is 43 dB and the phase accuracy is 0.4°.*

5.3 Conclusion

We have demonstrated that scanning near-field optical microscopy with coherent (heterodyne) detection is a powerful method for measuring both the amplitude and the phase of an optical field on the nanometer scale. We have presented amplitude and phase measurements of a standing evanescent wave, with a resolution of 1.6 nm between sample points. The results are in very good agreement with the theory. These test measurements are very useful because the prism surface is flat, assuring that topography perturbs neither the motion of the probe nor the optical signal. Changes of amplitude and phase around transition points can be observed with high resolution, since the finite width of the fiber tip averages the field amplitude rather than the intensity. At the nodes of the standing waves, the intensity is reduced but does not go down to zero. Thanks to the calculations and to this minimum level, we can predict the ratio of the intensities of the interfering waves. Although the intensity is low at these transition points, the resolution of the phase is high (0.4°) because the SNR is still significant (43 dB). The transition of the phase at these points is steep (7.5°/nm).

6 Fields generated by gratings

In this chapter, we intend to gain an understanding of the interaction of light with microstructures in order to determine their optical properties. Measurements of the amplitude and phase close to gratings are presented using a heterodyne scanning probe microscope [54, 55]. We discuss some basic properties of phase distributions. Indeed, coherent light diffracted by microstructures can give birth to phase dislocations, also called phase singularities. Phase singularities are isolated points where the amplitude of the field is zero. The position of these special points can lead us to information about the structure (shape, surface defects, etc), by comparing with rigorous diffraction calculation using e.g. the Fourier Modal Method (FMM). We present high-resolution measurements of such phase singularities and compare them with theoretical results. Polarization effects have also been studied in order to understand better the field conversion by the fiber tip.

Measurements of amplitude $A(\vec{x})$ and phase $\phi(\vec{x})$ with a heterodyne scanning probe microscope have been made in the optical field diffracted by periodic microstructures, in particular a holographically recorded 1 µm pitch grating. In fact, well-known diffractive structures with well-defined transmitted fields are useful to characterize the instrument. Most SNOM measurements are done at constant height (or constant intensity) in the X-Y plane (parallel to the surface) above the samples. However the optical field diffracted by a structure depends strongly on the *z*-position, normal to the surface. Therefore, we have performed scans above the structures in the X-Z plane, perpendicular to the surface.

By illuminating the sample at normal incidence, we observe the transmitted diffracted field. In this case, we can investigate the propagation (in the *z*-direction) of the light after the periodic modulation, in both *TE*- and *TM*-polarization. The periodic reproduction of the optical features far above the grating is explained by the *Talbot effect* [56, 57]. The *TM*-mode contains *x*- and *z*-components (E_x and E_z) of the total electric field. The separation of the measured components of well-known fields can help us to understand the coupling of the field into the fiber tip and thus

lead us to a better interpretation of the image. Comparison with theoretical calculations using the Fourier Modal Method (FMM) shows good agreement with the amplitude and phase measurements.

We will show sub-wavelength measurements from a scanning probe optical microscope working at micrometer distances from a periodic grating. One has to differentiate the material object and the optical field. In general, the produced optical field is not equal to the geometrical shape of the object. Even if the size of the structure is larger than the wavelength, the optical features that are engendered are often smaller than the wavelength. A 10 nm lateral variation of the phase field can be achieved even without the contribution of evanescent waves. Using coherent detection (heterodyne), the optical field rather than the intensity is averaged by the tip, allowing phase singularity detection. We are able to observe the change in the sign of the complex amplitude passing through a phase dislocation. High accuracy measurements of phase singularities demonstrate high spatial resolution. Phase measurements with the heterodyne scanning probe have been compared with a high-resolution interference microscope (HRIM). It turns out that we have two complementary instruments to investigate the same structures in order to understand polarization effects and also optical field conversion into the fiber by the tip.

6.1 Diffraction problem

In order to characterize the instrument we have developed, we must verify the measurements obtained by comparing with theory. Well-known samples, producing well-defined fields, will help us to know what we really measure. In this section, we will briefly present the diffraction problem of a grating. Rigorous methods are required to model periodic structures in order to compare the measured diffracted field with theory.

6.1.1 Theoretical background of grating theory

It is well-known that a periodic scatterer illuminated by a plane wave generates a discrete set of propagating plane waves. The main goal of grating theory is to predict the complex amplitudes of these plane waves if the grating structure is known. The opposite case is presented here: by measuring the diffracted field, we would like to know the structure.

The property of a grating to diffract an incident beam into clearly distinguished directions is given by the grating equation [58]:

$$n_2 \sin\theta_m = n_1 \sin\theta_i + m\frac{\lambda}{\Lambda},\ m = 0,\ \pm 1,\ \pm 2,\ \ldots, \tag{6.1}$$

where θ_i and θ_m are the angles between the incident (and the diffracted) wave directions and the normal to the grating, λ is the wavelength, n_1 and n_2 are the refractive indices of the media, Λ is the grating period and $m = 0, \pm 1, \pm 2, \ldots$ is an integer numbering the diffracted orders, so that the specular one is numbered as 0 (Fig. 6.1). If $m = 0$, Eq. (6.1) is equivalent to the Snell-Descartes law of Eq. (4.1). Two grating configurations are possible: *reflection* and *transmission gratings*. Equation (6.1) is the transmission grating equation (Fig. 6.1).

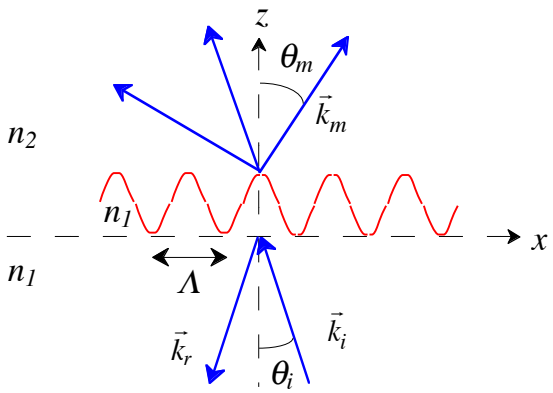

***Figure 6.1**: Diffraction m orders (with an angle θ_m) by a transmission grating*

Another notation uses $\alpha = k_x/|\mathrm{k}|$ and $\beta = k_z/|\mathrm{k}|$, where $k = 2\pi/\lambda$ is the wavenumber ($k_y = 0$). The propagating diffraction orders are thus expressed by $\alpha = n\sin\theta$ and $\beta = n\cos\theta$. The quantity $K = 2\pi/\Lambda$ is called the *grating wavenumber*. The corresponding grating vector $\vec{K}$ has the components $K_x = 2\pi/\Lambda$ and $K_y = K_z = 0$.

A solution of Eq. (6.1) is possible only when

$$|\sin\theta_m| < 1. \tag{6.2}$$

Diffraction orders with number m fulfilling Eq. (6.4) are called *propagating orders*. The vertical (z-direction) wavevector component can be found from [59]:

$$k_x^2 + k_z^2 = \left(\frac{2\pi}{\lambda}n\right)^2, \tag{6.3}$$

so that

$$k_{m_z} = \sqrt{\left(\frac{2\pi}{\lambda}n\right)^2 - k_{m_x}^2} = \frac{2\pi}{\lambda}n\cos\theta_m. \tag{6.4}$$

The x and z variation of the propagating orders

$$\exp\left(ik_{m_x}x + ik_{m_z}z\right) = \exp\left\{in\frac{2\pi}{\lambda}\left(x\sin\theta_m + z\cos\theta_m\right)\right\} \tag{6.5}$$

represents a plane wave which propagates in the direction of $\vec{k}_m$.

In the opposite case where $|\sin\theta_m| > 1$, Eq. (6.6) implies that the vertical component of the wavevector is imaginary and these orders decrease exponentially with the distance from the grating surface. Their amplitudes are given by

$$\exp\left(ik_{m_x}x - k_{m_z}z\right), \tag{6.6}$$

with

$$k_z = \sqrt{k_x^2 - \left(\frac{2\pi}{\lambda}n\right)^2}. \tag{6.7}$$

These orders are called *evanescent orders*. They can not be detected at a distance greater than a few wavelenghts from the grating surface. Fig. 6.2 represents the directions of the diffracted orders formed by adding or substracting a multiple of the grating wavevector *K* from the zeroth order. The wavevectors of the propagating orders have moduli equal to $2\pi/\lambda$. Evanescent orders lie outside of this area. The representation of Fig. 6.2 is called *Ewald-sphere* [60].

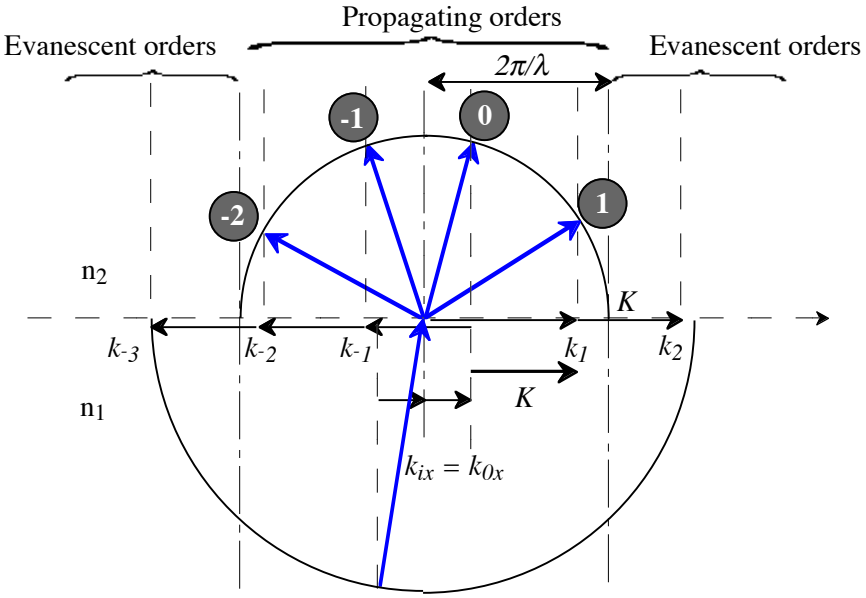

***Figure 6.2**: Schematic representation of grating orders wavevectors, using Ewald-spheres. $k_i = k_0$. A grating vector K is added or substracted from k_0 to form the diffracted order horizontal wavevector component. In this case, the orders –2, -1, 0, 1 are propagating and the others are evanescent.*

The grating equation determines the direction of propagation of the different diffracted orders but says nothing about the amount of light which is distributed in each order. The ratio of the optical power of a particular order (parallel to the *z*-axis) to the incident optical power is called *diffraction efficiency*.

6.1.2 Interference of three diffracted waves from a grating

In this sub-section, we are interested in the special case of a 1 µm pitch surface relief grating. With a wavelength of $\lambda = 0.532\ \mu\text{m}$, which is smaller than the pitch of $\Lambda = 1\ \mu\text{m}$, we get for normal incidence (Fig. 6.3) 3 propagating wavevectors $\vec{k}_0$, $\vec{k}_{+1}$ and $\vec{k}_{-1}$. The diffraction angles (given by $\sin\theta = \lambda/\Lambda$) are $\theta_0 = 0°$ and $\theta_{\pm1} = 32.1°$. The orders $\vec{k}_{\pm m}$ for $m \geq 2$ are evanescent.

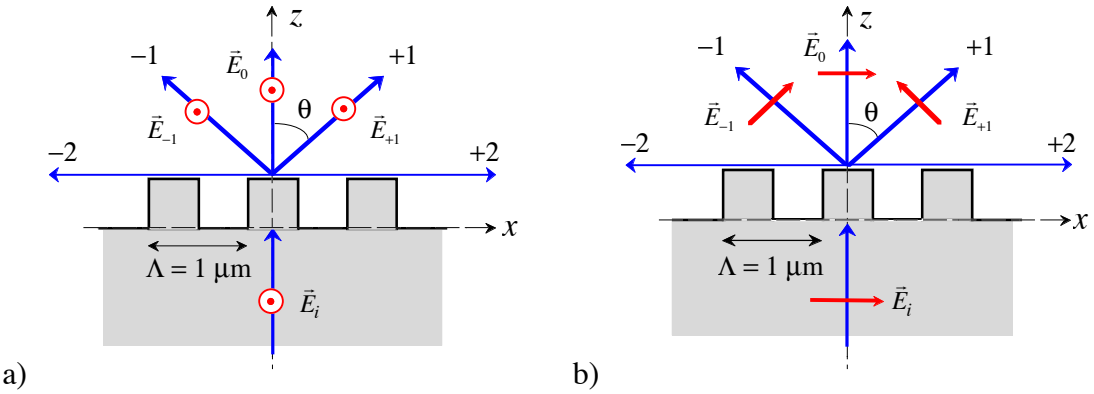

***Figure 6.3**: Diffraction by a 1 µm pitch grating at normal incidence for **a)** TE-mode and **b)** TM-mode. Zero and first orders are propagating; the higher diffraction orders are evanescent.*

As the wavelength is smaller than the period of the grating, we will always get at least one propagating non-zero order. In this case, the evanescent orders are "hidden" by the diffracted orders in the far-field (at distances larger than λ). As evanescent orders do not contribute to the far-field [61], the situation here can be assimilated to three-wave interference. We have to distinguish two polarization states. If the incident wave is linearly polarized and the electric field vector is perpendicular to the plane of incidence (X-Z plane), all diffracted orders have the same polarization, called *s*- or *TE*-polarization (Fig. 6.3a). The other case, where the electric wavevector is parallel to the incident plane, is called *p*- or *TM*-polarization (Fig. 6.3b). Any other polarization state can be expressed by a linear combination of these two fundamental states. In the *TE* case, only one component E_y of the electric vector is present, whereas in the *TM* case two components E_x and E_z have to be considered.

For *TE*-mode illumination, the total electric field of the –1, 0 and +1 diffraction orders is given by

$$E_y^{tot}(x,z) = a_{-1}\exp\{-ik(-x\sin\theta + z\cos\theta)\} + a_0\exp(-ikz) + a_{+1}\exp\{-ik(x\sin\theta + z\cos\theta)\} \quad (6.8)$$

where a_0 and $a_{\pm1}$ are the (complex) amplitudes of the three propagating plane waves, θ is the diffraction angle of the –1 and +1 orders and $k = 2\pi/\lambda$ is the wavenumber. By assuming that $a_{-1} = a_{+1} = a_1$, we get the symmetric case

$$\begin{aligned} E_y^{tot}(x,z) &= a_1 \exp(-ikz\cos\theta)\{\exp(ikx\sin\theta)+\exp(-ikx\sin\theta)\} + a_0\exp(-ikz) \\ &= 2a_1\cos(kx\sin\theta)\ \exp(-ikz\cos\theta) + a_0\exp(-ikz) \end{aligned} \tag{6.9}$$

and thus the amplitude of the electric field is

$$A_y^{tot}(x,z) = \sqrt{a_0^2 + 4a_1^2\cos^2(kx\sin\theta) + 4a_1a_0\cos(kx\sin\theta)\ \cos[kz(1-\cos\theta)]} \tag{6.10}$$

and the phase is

$$\Phi_y^{tot}(x,z) = \tan^{-1}\left\{\frac{-2a_1\cos(kx\sin\theta)\ \sin[kz(1-\cos\theta)] - a_0\sin(kz)}{2a_1\cos(kx\sin\theta)\ \cos[kz(1-\cos\theta)] + a_0\cos(kz)}\right\}. \tag{6.11}$$

The pitches of the interference pattern in the x- and z-direction are given by

$$\Lambda_x = \frac{\lambda}{\sin\theta} \text{ and } \Lambda_z = \frac{\lambda}{1-\cos\theta}. \tag{6.12}$$

The resulting amplitude and phase of the interference of the three plane waves is shown in Fig. 6.4. Depending on the position in z, we get a modulation in the x-direction (z constant) either of $\Lambda = \Lambda_x = 1\ \mu$m or $\Lambda = \Lambda_x/2 = 0.5\ \mu$m. In the z-direction, the periodicity of the optical feature is $\Lambda_z = 3.48\ \mu$m (Fig. 6.4a). In Fig. 6.4b a phase singularity is shown inside the circle. Phase singularities are isolated points where the intensity of the optical field is zero. Interference of at least three plane waves is needed to give birth to phase singularities. Properties of these special phase-points are presented in section 6.4.

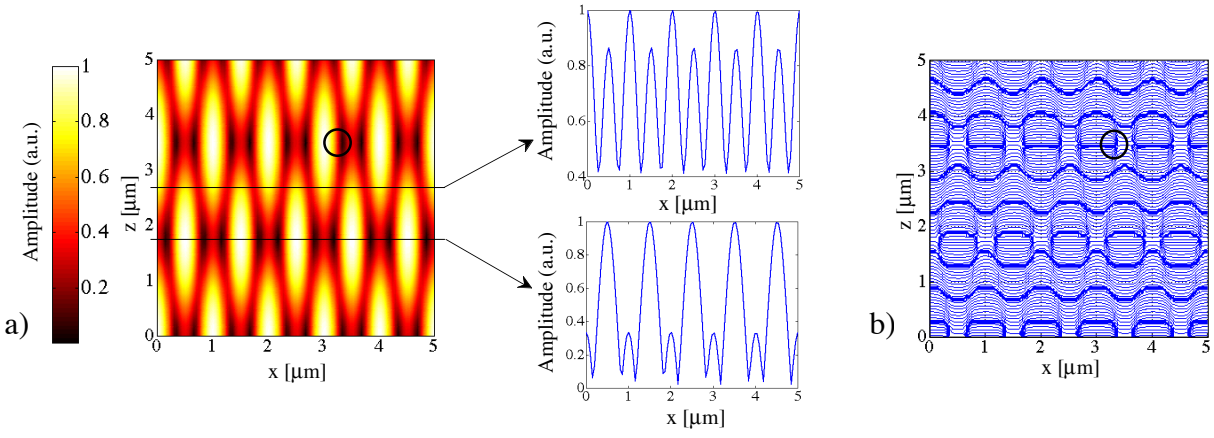

***Figure 6.4**: Calculated interference of three plane waves for the TE-mode. The factors a_0 and a_1 are chosen to be equal to 1. The circle shows the position of a phase singularity. **a)** (Normalized) amplitude distribution with two cross-sections at different heights (z constant). **b)** Contour plot of the phase (iso-phase lines).*

For the *TM*-mode illumination (Fig. 6.3b), the total electric field vector of the –1, 0 and +1 diffraction orders is given by

$$\vec{E}_{tot}(x,z) = \vec{E}_0 + \vec{E}_{-1} + \vec{E}_{+1} = \begin{pmatrix} E_x \\ 0 \\ E_z \end{pmatrix} = \begin{pmatrix} E_0 + E_{-1}\cos\theta - E_{+1}\cos\theta \\ 0 \\ E_{-1}\sin\theta + E_{+1}\sin\theta \end{pmatrix}. \qquad (6.13)$$

By assuming again that $a_{-1} = a_{+1} = a_1$, we get for the x-component of the total electric field vector

$$E_x = a_0\ e^{-ikz} + 2i\ a_1\cos\theta\ \sin(kx\sin\theta)\ e^{-ikz\cos\theta} \qquad (6.14)$$

and for the z-component of the total electric field vector

$$E_z = 2a_1\sin\theta\ \cos(kx\sin\theta)\ e^{-ikz\cos\theta}. \qquad (6.15)$$

Amplitude and phase of E_x and E_z following Eqs. (6.14) and (6.15) are presented in Fig. 6.5.

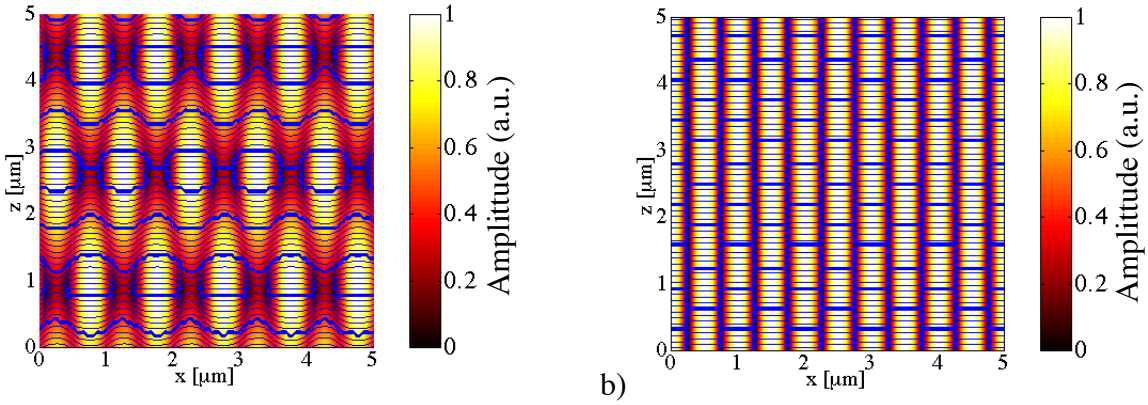

Figure 6.5*: Calculated interference of three plane waves for the TM-mode. The factors a_0 and a_1 are chosen to be equal to 1.* ***a)*** *Normalized amplitude (gray scale) and phase (iso-phase lines) distributions of the E_x component and* ***b)*** *of the E_z component of the total electric field vector.*

We see that the x-component is very similar to the case of the *TE*-mode, but that the z-component is totally different. Since E_x is perpendicular, but E_z parallel to the tip, the problem will be to know what is really detected by the SNOM tip: only E_x, or a combination of E_x and E_z? This is a crucial question, because the answer explains the behavior of the tip probe and might lead to know its transfer function [62, 63] for the electrical field vector.

6.1.3 Rigorousely calculated field diffracted by gratings

In the previous sub-section, we have studied the propagation of the light diffracted by a grating of 1 μm pitch assuming a superposition of 3 plane waves of identical amplitude and polarization, interfering in free space. Analysis of the diffraction problem has to consider the exact shape of the grating that diffracts the incoming light. However, the distribution of the amplitude and the phase behind a grating depends strongly on the relief of the grating (shape, height, fillfactor, period). Moreover, the near-field close to the surface (less than one wavelength) is quite different from the far-field, because of the contribution from the evanescent waves.

For a correct analysis, rigorous diffraction theory has to be employed. Thanks to computation time improvement, rigorous methods have been developed to calculate exact solutions of Maxwell's equations. Rigorous methods take into account the state of polarization of the light whereas it is neglected in approximation methods such as thin-element. In this section, we will give a very short description of the Fourier Modal Method [64], which is a differential method based on mode expansion of the field inside the grating structure.

The Fourier Modal Method (FMM) is based on variable separation of the Helmholtz equation in homogenous media. A 2-D software based on FMM calculations has been developed [65] for periodic optical structures in *TE*- and *TM*-mode. The elementary structure, which is then repeated periodically, is approximated by a number of different homogenous layers (Fig. 6.6).

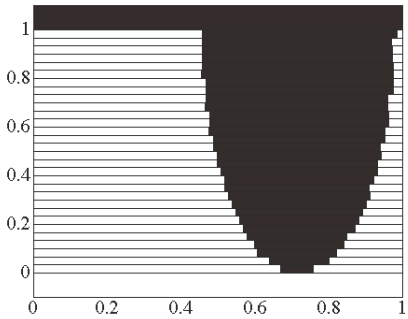

***Figure 6.6**: Homogenous layers approximation of the elementary structure of a grating.*

The larger the number of layers, the better the approximation of the shape of the structure, but this demands more computer time. The input parameters are the shape of the grating, the incident monochromatic wave (wavelength, incident angle and polarization), the number of diffraction orders and the refractive indices (at the different interfaces). The result of a rigorous calculation of gratings will be shown in sections 6.4 and 6.5.

6.2 Experimental set-up

The main set-up is the same as described in chapter 3. The illumination system for the sample is shown in Fig. 6.7a (scheme of Fig. 3.4 (top)). The light comes from a single-mode fiber and is collimated to get a plane wave. A half-wavelength plate rotates the polarization in order to get *TE*- or *TM*- polarization illumination. Then, the polarization is optimized with a Glan-Thomson polarizer. A 45°-mirror sends the light trough the sample at normal incidence. The illumination system and the sample are mounted on a *x*-*y*-*z* piezo-electric translation stage ($100\times100\times20$ µm range) which allows accurate translation steps (2 nm resolution in *z*-direction). The fiber tip is mounted independently from this translation system. The bent tip is used as a conventional AFM (Atomic Force Microscope) cantilever and is brought close to the surface. Once the tip approach is done, the AFM feedback is switched off and the scan (in XY or XZ planes) is accomplished by the *x*-*y*-*z* stage. Phase measurements performed with this system require a high mechanical stability. For this purpose, mechanical vibrations are avoided by an air-cushion optical table and thermal fluctuations are limited due to a Plexiglas box surrounding the system (Fig. 3.3). The reduction of humidity can also be important. The humidity is reduced by silica gel placed inside the box.

An image is acquired by scanning in the *x*-direction at constant height and with a scan rate according to the number of pixels and the integration time (see section 3.2.4). Then, the tip returns to the initial *x*-position and moves down by one *z*-step for the next *x*-line scan (Fig. 6.7b).

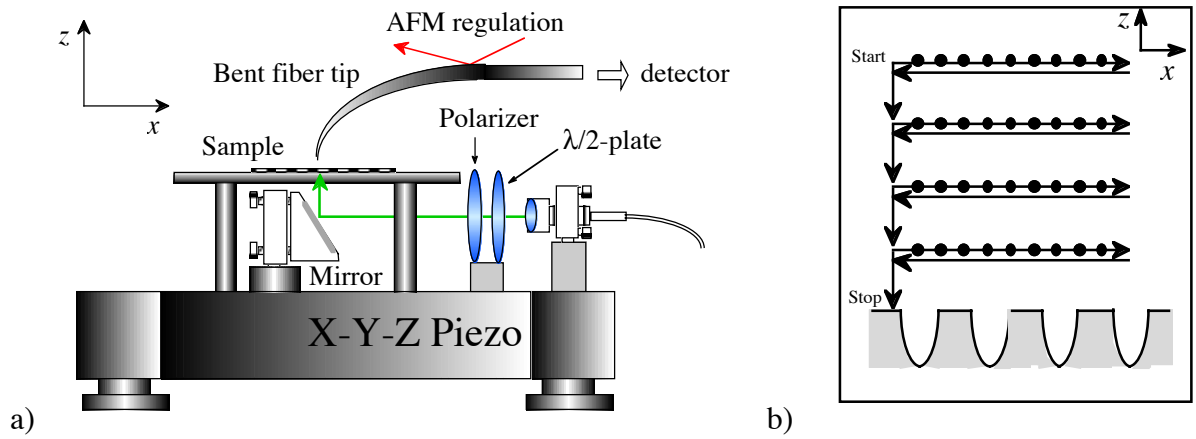

***Figure 6.7**: **a)** Experimental set-up for the illumination of the sample and the fiber tip probe. **b)** Movement of the sample compared to the tip position during the scanning in the X-Z plane above the grating and acquisition of data points for image formation.*

We use a dielectric fiber tip to collect the field information. The small coupling between the dielectric tip and the dielectric grating gives a negligible contribution to the total electric field [66]. Thus, the measured field should not be perturbed by the presence of the tip.

The sample is a 1 μm pitch quasi-binary shape grating, as described in Fig. 6.6, recorded holographically in photo-resist. A SEM (Scanning Electron Microscopy) picture of the grating is shown in Fig. 6.8.

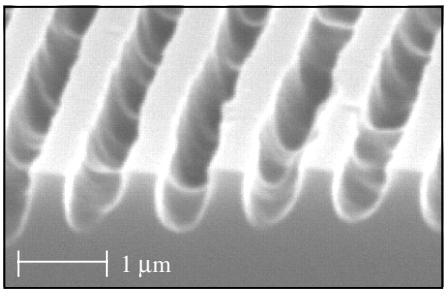

Figure 6.8*: SEM image of the holographically recorded 1 μm pitch grating in photo-resist. The depth is about 0.7 μm.*

6.3 *TE*-mode amplitude and phase measurement behind the grating

Usually SNOM images are acquired in constant intensity or constant height mode (in the XY-plane) above the sample. However, in all SPM techniques, the absolute distance between the tip and the surface is not really known. Equation (6.10) in *TE*-mode predicts periodic variations of the propagating field in the *z*-direction. Indeed, the optical field depends strongly on the tip-surface distance. Therefore, we performed scans in the plane of incidence (X-Z) in order to see how the field develops behind the sample [54]. According to the set-up of Fig. 6.7a, measurements of the *TE*-mode amplitude (Fig. 6.9a) and phase (Fig. 6.9b) from a 1 μm pitch grating in the X-Z plane have been performed. The phase in Fig. 6.9b is represented by a contour plot (iso-phase lines). The distance between two "bold" lines is λ (and thus corresponds to 2π). The image has been acquired by scanning in the *x*-direction at constant height with a step of $\Delta x = 25$ nm, starting at $z = 10$ μm and moving down in $\Delta z = 50$ nm steps for further x-line scans. The total scan size is x = 5 μm by z = 10 μm and the number of pixels is 200×200. With a integration time of $\tau = 30$ ms, the global image is acquired in 20 minutes. The zero in the *z*-direction is arbitrary. The scan is executed until the tip touches the surface. There is excellent agreement with the theoretical expectations show$_n$ in Fig. 6.4. In Fig. 6.9a, a discontinuity appears at the height z = 0.4 μm. At this position the tip touches the surface and damages the photo-resist structure. In the next section, this situation will be discussed in more detail.

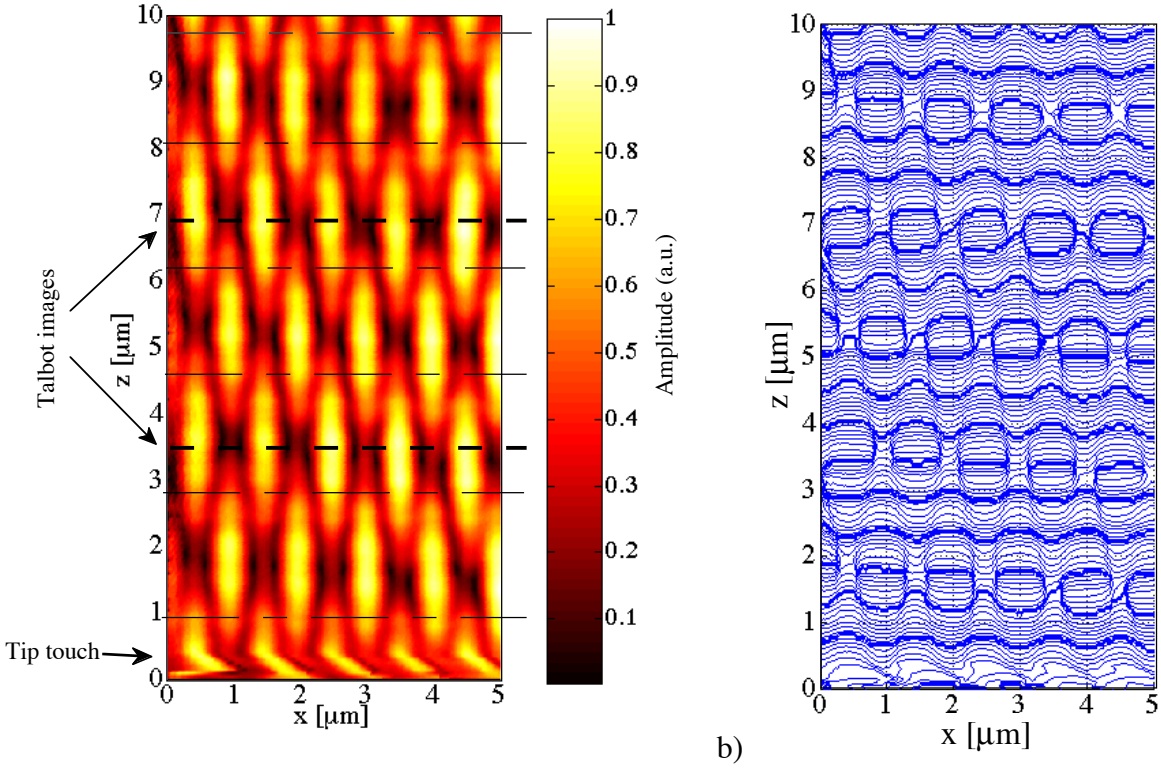

***Figure 6.9**: Measured TE-mode optical field emerging from a 1 µm pitch grating (0.55 µm height): **a)** normalized amplitude and **b)** contour plot of the phase (iso-phase lines). The scan size in the XZ plane is 5 µm in x-direction and 10 µm in z-direction (200x200 pixels). At z = 0.4 µm the tip touches the surface. The bold dashed lines are the Talbot images and the thin dashed lines are the Talbot subimages.*

In Fig. 6.9 we can see a periodic feature in the *z*-direction. A Fourier analysis of the diffracted field distribution explains this phenomenon, known as *Talbot effect* [67]. The intensity observed behind the grating at distances $z_m = 2m\Lambda^2/\lambda$, where *m* is an integer, is a perfect reproduction of the intensity that would be observed just behind the grating [68]. Such images are called *Talbot images*. In our case, where $\Lambda_x = 1\ \mu m$ and $\lambda = 0.532\ \mu m$, the Talbot planes are situated at $z_m = m \cdot 3.76\ \mu m$ (Fig. 6.9a, with $m = 1, 2$). *Talbot subimages* with twice the frequency of the original grating ($\Lambda_x = 0.5\ \mu m$) and reduced contrast are situated at distances $z_m = (m-1/2)\Lambda^2\lambda^{-1}$, or $z_m = (m-1/2)\cdot 1.88\ \mu m$ (thin dashed lines in Fig. 6.9a). The Talbot effect can be observed for any periodic structure.

6.4 Phase singularities produced by microstructures

A phase singularity, or a dislocation is an isolated point where the amplitude is zero [69]. At this point, the phase is not determined. The time-averaged Poynting vector is zero and the energy flows around the phase singularity. Phase dislocations can be observed in the near- and far-field

of optical microstructures, such as gratings [70]. The position of phase dislocations depends essentially on the period, the height, the shape and the fill-factor of the grating. Therefore, according to the position of the phase singularity, the structure of the grating can be recovered [71] by comparing the measured positions with rigorous calculations of the diffraction. However, the relationship between the position of the phase dislocation and the structure is not straightforward.

By zooming into a region of Fig. 6.9b (Fig. 6.10b), we can compare the measured phase distribution with the calculated one (Fig. 6.10a). Comparison with theoretical calculations using Fourier Modal Method leads us to the following observations [55]: from 0.5 µm above the grating, the measured phase agrees very well with the theory.

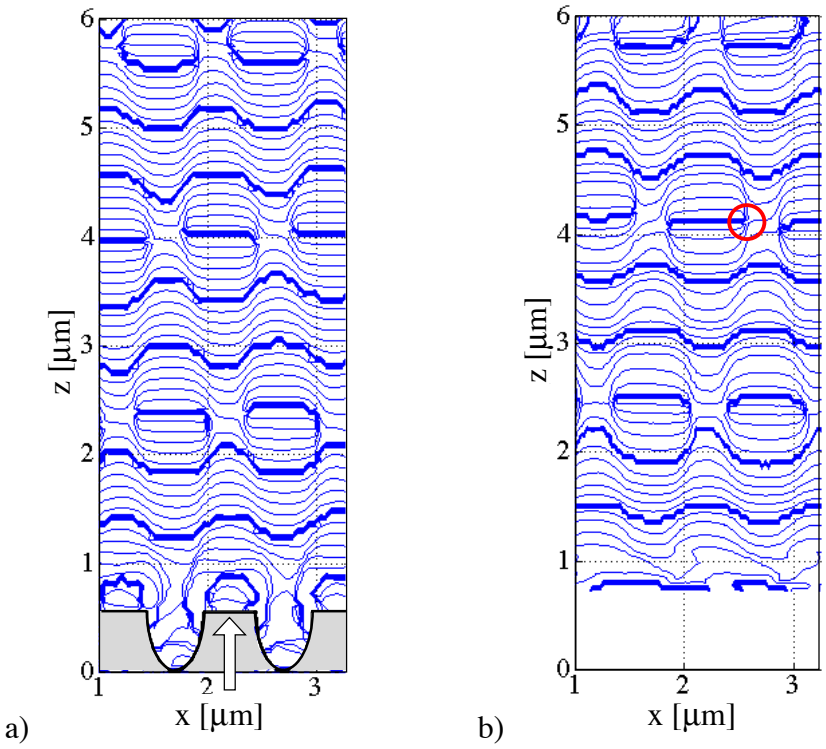

***Figure 6.10**: Comparison of calculated and measured phase distribution for the grating shown in Fig. 6.8. **a)** Calculated phase distribution with the Fourier Modal Method. **b)** Measured phase (zoom from Fig. 6.9b). The circle encloses one phase singularity. The field within the first 500 nm from the top of the structure could not be measured, because the tip apex touched and damaged the grating. The zero of the z-position has been adapted to the absolute scale of the calculation.*

Within the first 500 nm from the top of the structure, the field (amplitude and phase) is not correctly measured. Indeed, the tip apex touched the photo-resist surface before measuring the field closer to the structure. In fact, simulations for uncoated dielectric fiber tips show that the light is not captured at the apex of the tip, but rather at a distance of about 400-500 nm inside the tip. Measurements with coated tips give comparable results.

The evolution of the optical phase in time can be simulated by an additional linearly increasing phase of the reference wave. In Fig. 6.11 we present another measurement of the phase around a phase singularity using the following approach: the reference phase increases from Figs. 6.11a to 6.11f in steps of 60°. The spatial resolution of the measurments is 10 nm in the *x*-direction and 20 nm in the *z*-direction. We observe that the measured phase distribution changes its shape, but the phase singularity does not change its position. The phase distribution turns around the phase dislocation (which remains at a fixed position) as the wave propagates in z-direction.

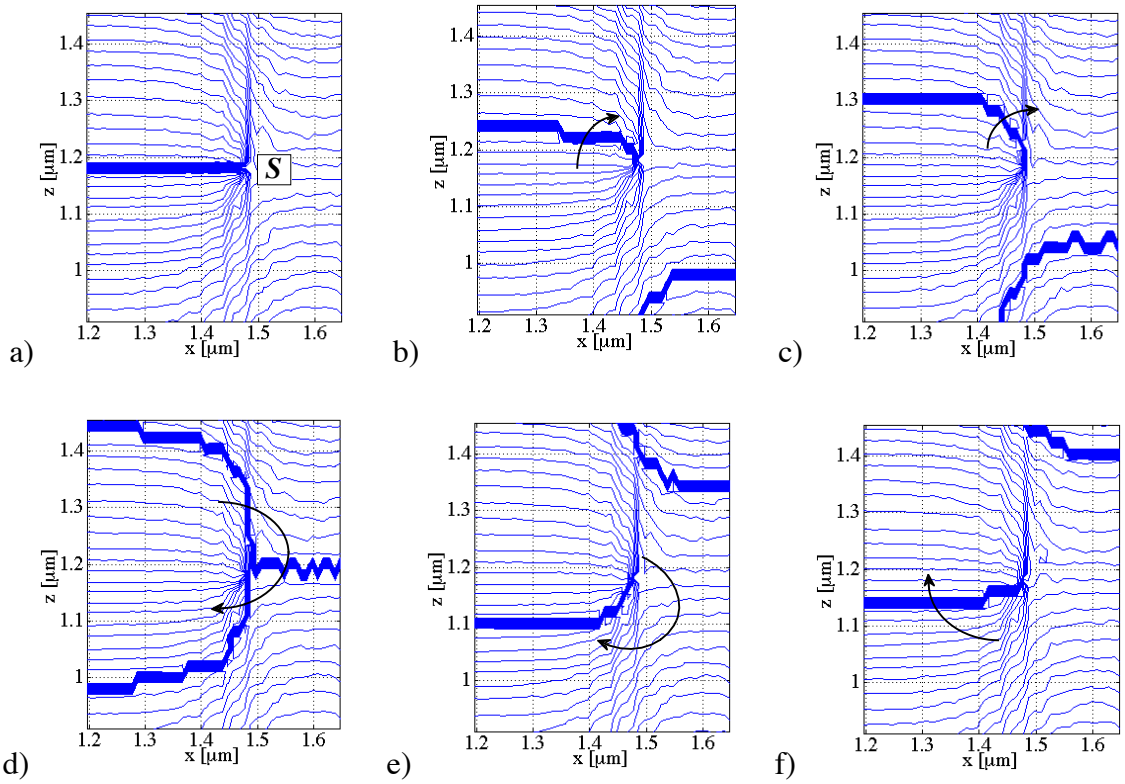

Figure 6.11*: Phase measurement around an isolated phase singularity ("S") located at x = 1.48 µm and z = 1.18 µm. The scan step is 10 nm in x-direction and 20 nm in the z-direction. The additional reference phase increases from* ***a)*** *to* ***f)*** *in steps of 60°. Two consecutives lines are separated by π/10.*

Figure 6.12 shows another measurement, but similar to a crossection of Fig. 6.11a at z = 1.18 µm. By crossing the phase singularity, the amplitude makes a transition through zero (Fig. 6.12a) and the phase jump is always π (Fig. 6.12b). In this figure, we demonstrate that, at a phase singularity, the phase is not defined (because the signal vanishes in the noise) and the amplitude is really zero. In fact, we measured the zero amplitude, or more precisely, the zero optical power, down to $P_o = 10^{-16}$ W (Fig. 6.12a, with the marker "*S*"). From Eq. (2.22), the minimum detectable power is $P_o^{\min} = 2.7 \cdot 10^{-17}$ W at $B = 50$ Hz (with $\lambda = 532$ nm and $\eta = 0.7$). Thus the detected point is very close to the shot noise. The transition of the phase in

Fig. 6.12b is measured within one step of ±10 nm. The measured phase jump is as sharp as one step (with a slope of 18°/nm).

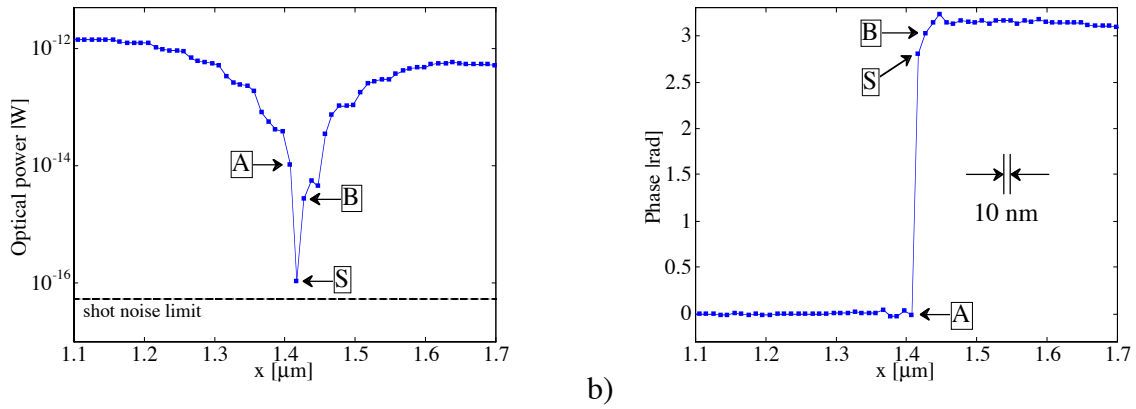

***Figure 6.12**: Measured optical power and phase by crossing a phase singularity (S). The phase singularity is the special point where **a)** the amplitude is zero ($P_{min} \approx P_{noise}$) and where **b)** the phase jumps by π (quasi-infinite slope).*

From these measurements we see that although the amplitude falls practically down to zero at the singularity, the signal to noise ratio around the phase singularity (Fig. 6.12b, markers A and B, separated by 20 nm) is sufficiently large to locate the phase jump with high accuracy. In fact, in Fig. 6.12b, from Eq. (2.18), the signal to noise ratios at the points A, S and B are $SNR_A = 26$ dB, $SNR_S = 6$ dB and $SNR_B = 21$ dB, respectively, corresponding to the optical powers of $P_A = 10^{-14}$ W, $P_S = 10^{-16}$ W and $P_B = 3 \cdot 10^{-15}$ W with $B = 50$ Hz. The resulting standard deviations for the phase measurement are obtained from Eq. (2.21) as $\delta\varphi_A = 3°$, $\delta\varphi_S = 30°$ and $\delta\varphi_B = 5°$. Although the phase is not well measured at S, the transition is very well localized (within 10-20 nm) by the measurements at marks A and B in Fig. 6.12b.

In general, dislocations are curved lines in space. At any given point on such a line, the sense of a small closed path around the phase singularity is chosen so that the total phase change, at a fixed time, is $+2\pi$. By integrating the phase change on a closed path around the singularity (shown by two circles in Fig. 6.13b) we get

$$\oint d\Phi = \pm 2\pi . \tag{6.16}$$

which is an essential property of a phase dislocation [72] and the value is unchanged as the path is varied. By using a right-hand rule, we can assign a direction to the dislocation, with unit vector **d** (Fig. 6.13a). A topological index is associated with dislocations. The index s is defined by the integral of the phase on a positive (anticlockwise) circle around the point:

$$s = \frac{1}{2\pi} \oint d\Phi . \tag{6.17}$$

In our case, at phase singularities shown in Fig. 6.13b, $s = \pm 1$. The case where the vector **d** is momentarily parallel to the surface corresponds to a mutual annihilation or creation of two topological points of opposite sign. Thus, $s = 0$ for a closed path surrounding both of them.

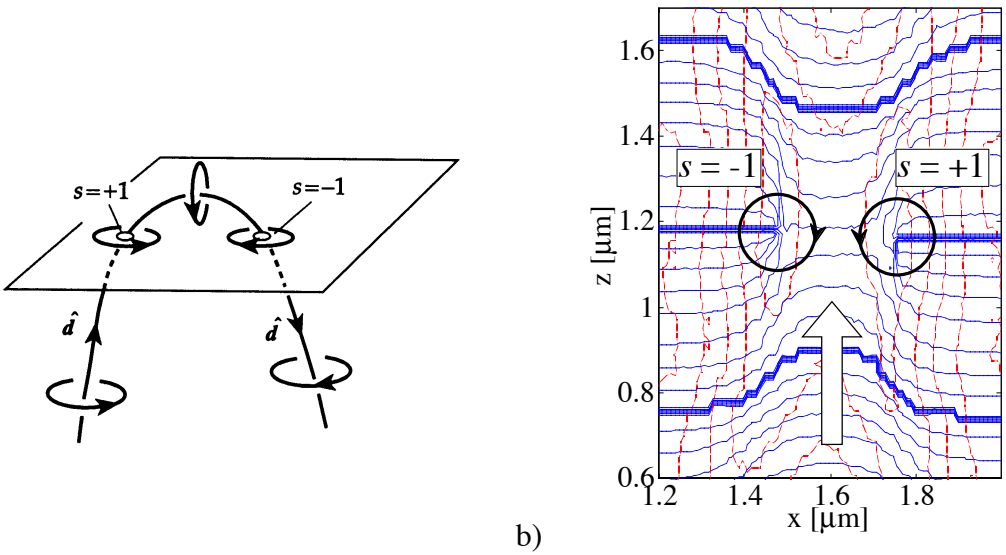

a) b)

***Figure 6.13**: **a)** The circulation sense of two edge dislocations with opposite topological index ($s = \pm 1$) (from [72]). **b)** Two measured edge dislocations (zoom out of Fig. 6.11a). As the propagation travels from down to up (white arrow), the phase turns around the edge dislocations (circles) with opposite sign. Contours of equal phase (solid lines) are drawn at intervals of $\pi/4$. A 2π range of phase lines comes into each dislocation. The contours of equal amplitude (broken lines) are shown. The minimum amplitude contour lines enclose the two phase singularities.*

6.5 Polarization effects in *TM*-mode

In section 6.3 we discussed the case of *TE*-mode diffraction by a grating. For the *TM*-mode the situation is more complicated, because the electric field has two components E_x and E_z. Therefore, the crucial question arises: what does the tip "see" and which field does it really capture? We will try to answer this fundamental question by analyzing the components of the diffracted field and by comparing the experimental results with the theoretical expectations. The measurements in the *TM*-mode have been performed with the same set-up and under identical conditions as for the *TE*-mode. The results are shown in Fig. 6.14. Although the amplitude field may look quite similar to the *TE*-mode, we see that the phase is totally different.

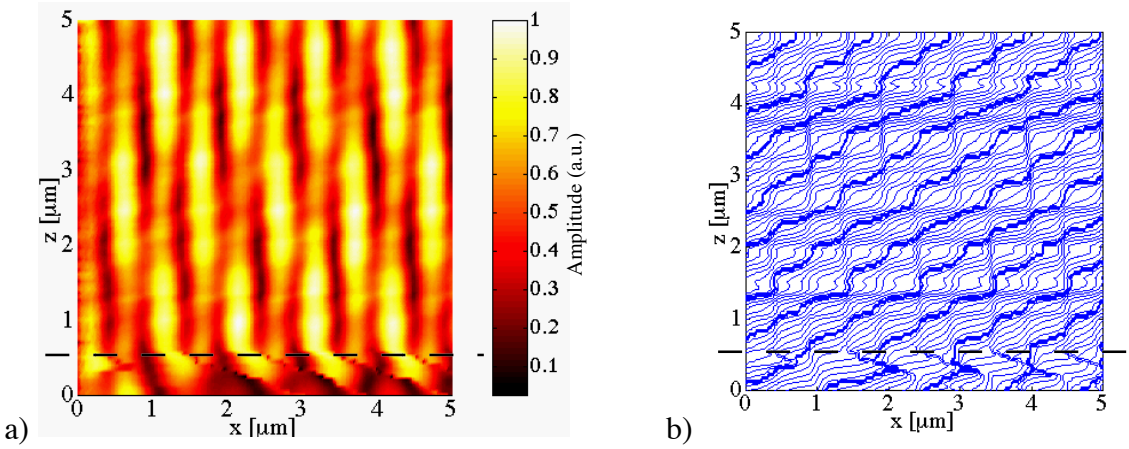

***Figure 6.14**: Measured TM-mode diffraction of a 1 µm pitch grating (700 nm height): **a)** amplitude and **b)** phase. At the position of $z = 0.58$ µm (dashed lines), the tip touches and damages the photo-resist structure.*

For the *TM*-mode, the coupling of the two components of the diffracted total electric field E_x and E_z to the scanning probe has to be considered. For a single mode 0°-cleaved fiber, only E_x would contribute to the fiber mode excitation. For a sharp fiber tip, the polarization coupling behavior is quite different and still not well established.

The vector $\vec{E}$ is composed of the two orthogonal components E_x and E_z (Eqs. (6.14) and (6.15)). Since they are orthogonal, they do not interfere. By introducing a fiber tip, the two components are coupled to the same propagating mode in the fiber and can therefore interfere with each another. This effect is similar to the interference of two orthogonal polarizations observed behind an analyzer, as explained in Fig. 6.15. By introducing the coupling coefficients [63] c_x and c_z for the E_x and the E_z component, respectively, we can express the total collected electric field by

$$E_{coll} = c_x E_x + c_z E_z. \tag{6.18}$$

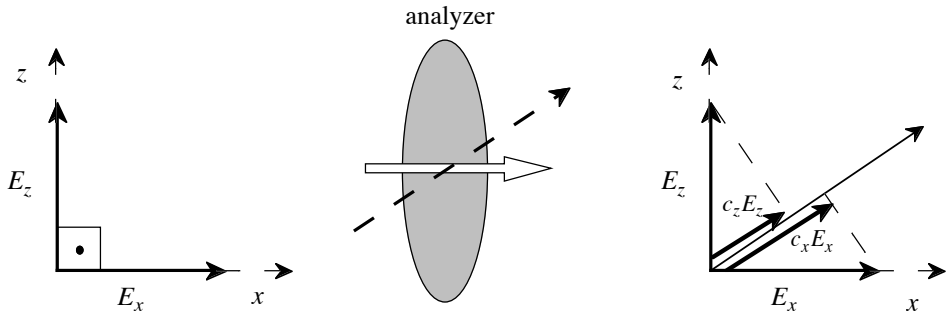

***Figure 6.15**: Analyzer (with arbitrary orientation) analogy of electric vector components coupling.*

In Fig. 6.16, we present the rigorous calculation of the diffracted field for each component E_x and E_z in the *TM*-mode, using the FMM. For E_x, the diffracted field can be assimilated to the *TE*-mode by symmetry and agrees with the results of Eq. (6.14). For E_z, however, the behavior is completely different Eq. (6.15). Although the amplitude distribution (Fig. 6.14a) for the E_x component looks similar to the measured one in Fig. 6.9a, the phase distribution (Fig. 6.14b) for both E_x and E_z is completely different from the measured one (Fig. 6.9b).

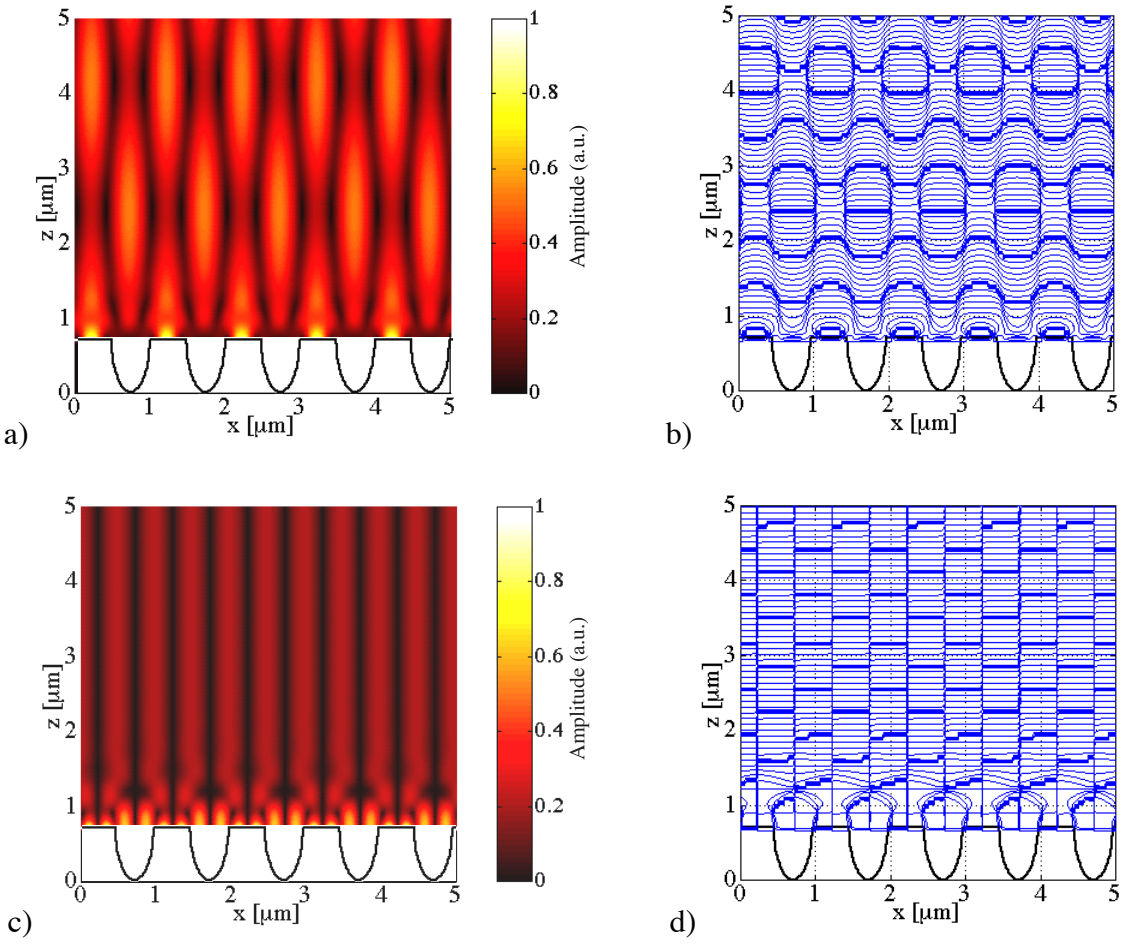

***Figure 6.16**: Rigorously calculated field diffracted by a grating in the TM-mode. The field inside the structure is not presented. **a)** Amplitude and **b)** phase of the E_x component. **c)** Amplitude and **d)** phase of the E_z component.*

If we assume now that the coupling coefficients for E_x and E_z are the same ($c_x = c_z$), we get the amplitude and phase distribution of the collected field shown in Fig. 6.17. This result corresponds quite well with the measured distribution in Fig. 6.14. The analogy with the analyzer would correspond to a 45°-orientation. It is interesting to note that the phase singularities have completely disappeared. It is important to be aware of this influence of the vector coupling behavior of the probe for image interpretation with scanning probe optical microscopes. The presented results demonstrate clearly that the phase distribution is more significant than the intensity (or amplitude squared) to establish the vector coupling properties of the probe and to avoid that artifacts are measured.

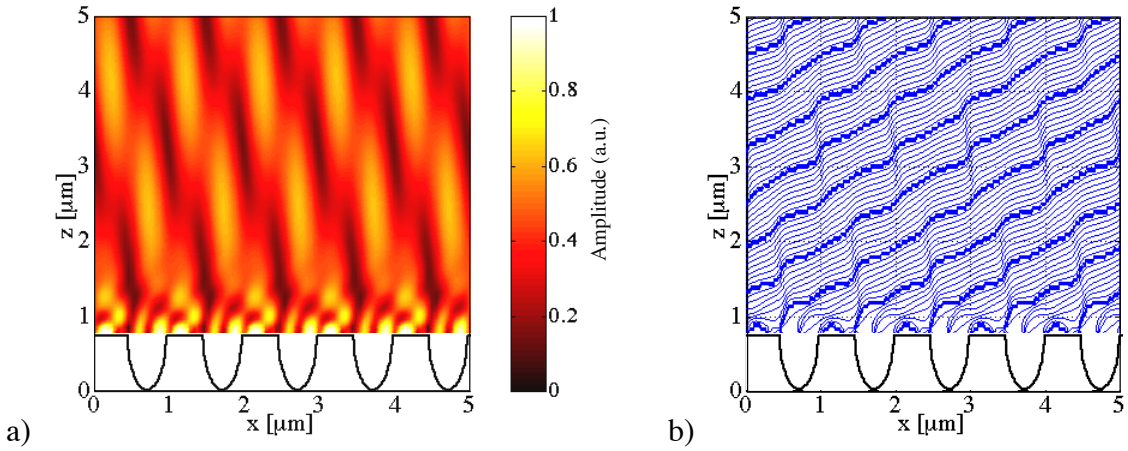

***Figure 6.17**: Rigorously calculated **a)** amplitude and **b)** phase of the collected electric field for* $c_x = c_z$ *(*$E_{coll} = E_x + E_z$*).*

6.6 Comparison with a high resolution interference microscope (HRIM)

For comparison, we also measured the phase distribution of the optical field behind the same grating with a high-resolution interference microscope [71, 73]. This instrument is based on a Mach-Zender interference microscope which has been modified in order to obtain a large magnification of about 1:1000 on a CCD camera, corresponding to 10 nm per pixel, and phase measurements in the z-direction, thanks to a scanning translation stage. The resulting phase measurements for a 1 µm grating illuminated in the *TM*-mode with $\lambda = 633$ nm is shown in Fig 6.18. The measured phase distribution is similar to the one calculated for the E_x component in Fig. 6.16b. In fact, in the case of the HRIM the total electric field (composed of E_x and E_z components) interferes with the reference plane wave, which has only a E_x component. Thus, E_z is not detected and the measured phase is given by the E_x component alone. The result is completely different from the measurement with the scanning fiber tip probe.

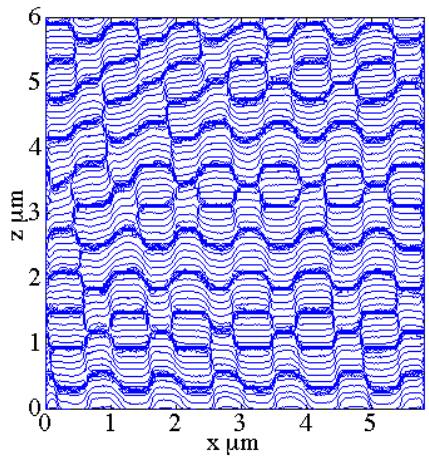

***Figure 6.18**: Measured phase with the high-resolution interference microscope (HRIM) behind a 1 µm grating illuminated in the TM-mode with* $\lambda = 633$ *nm.*

6.7 Conclusion

We have presented amplitude and phase measurements emerging from microstructures, in particular from gratings. The measurements have been made with a coherent heterodyne scanning probe optical microscope. Interaction with micro-optical structures changes the amplitude and phase of the incoming light field. Measuring the amplitude and the phase gives information about the structure, but the relationship is not trivial.

The properties of optical structures can be studied on the basis of phase singularities produced by the diffracted field. As the variation of the phase at these positions is very sharp (18°/nm), sub-wavelength resolution of phase measurements in the range of 10 nm has been achieved. The amplitude at phase dislocations is really zero (close to the shot noise limit) and thus the signal to noise ratio vanishes, leaving the phase undefined. However, the measured points before and after the phase transition (Fig. 6.12) are well-defined, allowing the phase singularity to be localized with sub-wavelength resolution. Phase measurements obtained with a high-resolution interference microscope show similar spatial resolution for phase singularities. However, in this case only the transverse (x,y) components of the electric field vector contribute to the measured amplitude and phase.

The field conversion by a SNOM probe is not yet well understood. We tried to provide some answers to this mechanism by an analysis of the measured components of the electric field vector in *TM*-mode. Interesting polarization effects have been observed. Our conclusion is that the *z*-component of the diffracted field contributes nearly as much as the transverse *x*-component to the excitation of the propagating mode in the fiber probe. In the future, we hope that such studies will help to understand the field conversion, and thus to establish the vectorial transfer function of the tip.

7 Conclusions

The main goal of this work was to understand optical fields with sub-wavelength features. To exactly know the characteristics of an optical field, intensity is not always sufficient. It is therefore essential to measure the amplitude and the phase. For this purpose, we have developed, within the framework of this thesis, a coherent probe system based on the combination of a heterodyne interferometer with a scanning near-field optical microscope (SNOM), allowing amplitude and phase measurement of propagating and non-propagating optical fields with sub-wavelength resolution. Thanks to heterodyne detection, we gain a factor 2 for the sensitivity with respect to direct detection. Low optical signals have been detected down to $10^{-16} - 10^{-17}$ W and the optical phase has been measured with high accuracy (down to 0.33° for an optical power $P_o = 1$ pW). A second goal was to understand the mechanism of the scanning near-field optical microscope itself, via to basic approaches. In fact, the coupling of the light into a probe is not yet well understood. We have also demonstrated that a physical hole is not necessary to build working near-field probes. The light can tunnel through a thin (about 20-50 nm) metallic coating at the tip.

In order to characterize our novel instrument, we have performed different measurements on simple optical fields. As a first test, we have measured the amplitude and the phase of a plane wave, showing the wavefronts of the propagation. Then, we have been interested in evanescent optical fields produced by total internal reflection at the interface of a prism. By frustrating the total internal reflection, we coupled the light into a fiber probe. The evanescent wave measurements also a allowed demonstration of the large dynamic range of heterodyne detection. In fact, the ratio between the maximum and the minimum detected optical power was in the presented measurements about 10^4. Moreover, it has been shown that the detection of evanescent fields may be corrupted by light scattered at the surface from defects or dust. 2-D scans allowed better observation of this phenomenon and to determine the position of the sources of the scatters. It has also been shown that humidity may cause the formation of a water meniscus between the tip and the surface, which perturbs the measurements of evanescent fields drastically.

We have presented amplitude and phase measurements of a standing evanescent wave. Changes of amplitude and phase around transition points (with a slope of 7.5°/nm) have been observed with high resolution (1.6 nm between sample points), even though the width of the fiber tip (larger than 30 nm) is significant. Although the intensity is low at the nodes of the evanescent standing wave, the resolution of the phase is high (0.4°) because the SNR is still good (43 dB).

An important part of our work was the study of the amplitude and phase emerging from microstructures, in particular from gratings. Interaction with micro-optical structures modifies the amplitude and phase of the incoming light field. Measuring the amplitude and the phase can lead to information about the structure, but the relationship is not trivial. The properties of optical structures can be studied on the basis of phase singularities produced by the diffracted field. As the variation of the phase at these positions is very sharp (18°/nm), sub-wavelength resolution of phase measurements in the range of 10 nm has been achieved. The amplitude at phase dislocations is zero and thus the signal to noise ratio (close to the shot noise limit) vanishes, leaving the phase undefined. However, the measured points before and after the phase transition are well-defined, allowing the phase singularity to be localized with sub-wavelength resolution. The field conversion by a SNOM probe is not yet well understood. We tried to provide some answers to this mechanism by an analysis of the measured components of the electric field vector in *TM*-mode. Interesting polarization effects have been observed. Our conclusion is that the z-component of the diffracted field contributes nearly as much as the transverse x-component to the excitation of the propagating mode in the fiber probe. In the future, we hope that such studies will help to understand the field conversion, and thus to establish the vectorial transfer function of the tip.

The main aims of this work have been achieved. The measurement of the amplitude and phase in optical fields with sub-wavelength features has been demonstrated, opening a new area of research in nano-optics. In fact, such an instrument can be utilized in different domains. In future, we hope that coherent scanning probes can aid us in the understanding and the fabrication of optical nano-structures, such as photonic bandgap waveguides used in telecommunication devices.

8 Appendix

8.1 Scanning software

The raster scan, as well as the image acquisition, explained in section 3.2.4, are performed by software written in Labview (Fig. 8.1). In this appendix, we will briefly explain its functioning. As the commercial software of the AFM does not allow any changes for specific applications, in particular for XZ-scans, another solution has been found. Thanks to the external *x-y-z* translation stage, driven by our software, we are able to fulfill all the 3-D movements in free space.

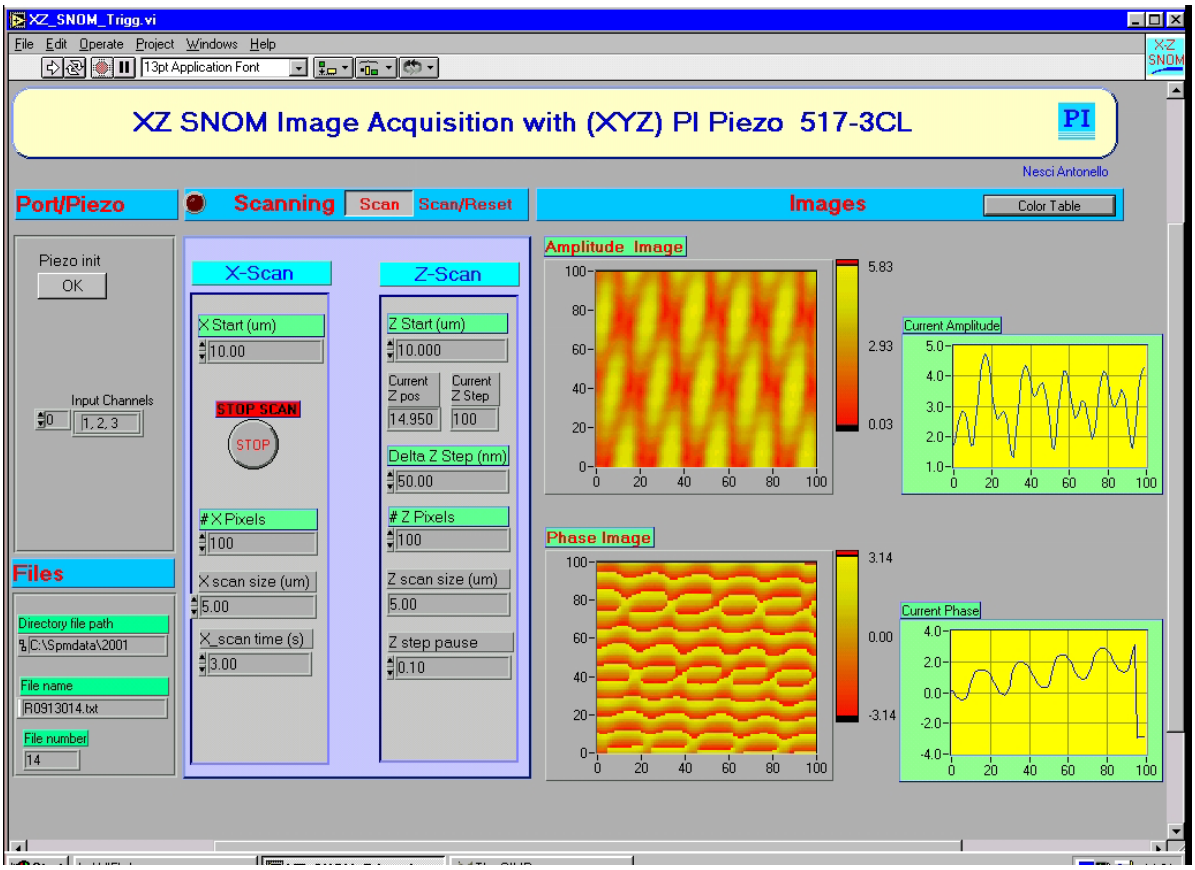

***Figure 8.1**: Picture of the scanning and acquisition software interface, written in Labview.*

The task of this computer program is the following: the sample, mounted on a *x*-*y*-*z* translation stage (Fig. 6.7a), moves with respect to the SNOM probe in a plane above the sample (XY, XZ or YZ). In this section, we will show an example for XZ-scans (Fig. 6.7b). A certain number of data points (pixels) is acquired simultaneously in order to build an image.

The flow chart showing the different steps of the software is presented in Fig. 8.2.

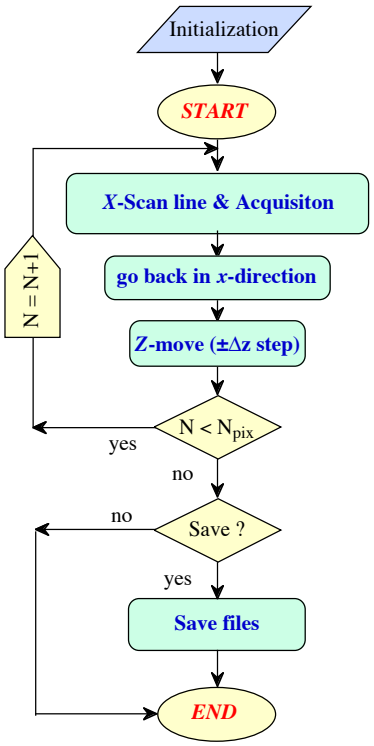

***Figure 8.2**: Flowchart of the X-Z scanning and data acquisition software. After the initialization of all the parameters, the scan starts in the x-direction. The acquisition is accomplished simultaneously. Each x-scan amplitude and phase are directly displayed. Then, we come back to the zero x-position and move up or down in the z-direction to begin a further x-scan. The loop ends when all the number of N_{pix} lines in z are fulfilled. The complete X-Z images of the amplitude and phase are displayed. If we want to save the images, the data are stored in simple text format files.*

In section 3.2.4, we have introduced the time T of the acquisition, depending on the integration time τ and on the number of pixels N_s (Eq. 3.7). The sample, with respect to the tip, is moved by a linear voltage ramp applied to the translation piezo-stage and scans one line of length D_s in a certain direction during the time T. Simultaneously, N_s data points are acquired. For each data point, the acquisition of the optical signal is performed during a time τ, determined by the integration time of the lock-in amplifier. The output signals of the lock-in amplifier $R\cos\phi$ and $R\sin\phi$ are saved in the input channels 2 and 3 (Fig. 8.1), respectively. The movement of the tip, during a scan in the XZ-plane, for instance, is showed in Fig. 6.7b.

Before starting the scan, several parameters are initialized. These parameters are the starting positions (in x and z) of the piezo-stage, the number of pixels for each direction, the scan time, the size of the x-scan length and the z-step (up with a positive sign and down with a negative sign). The number of pixels in the z–direction and the z-step gives the displacement size in z. A pause time can be introduced before starting each new scan line in order to make the movement

more stable. The text format files are numbered automatically in a new folder as follows: “R”+month+day+file_number.

The data acquisition is accomplished simultaneously during the scanning in the *x*-direction. A digital trigger ensures that the data acquisition and the ramp voltage in the *x*-direction start at the same time. Each *x*-scan amplitude and phase are directly displayed (in the windows “Current Amplitude” and “Current Phase” respectively in Fig. 8.1). Then, we come back to the zero *x*-position and move up or down in the *z*-direction to begin a further *x*-scan. The loop ends when all the number of N_{pix} lines in *z* are accomplished. The complete X-Z image of the amplitude and the phase is then displayed. If the image is satisfactory, we can save the data into simple text format files (corresponding to the signals $R\cos\phi$ and $R\sin\phi$). We can then rebuild the images with mathematical operation in Matlab (section 3.4).

8.2 Publications and conferences

Most of this work has been published as regular papers or at conferences, listed below:

A) A. Nesci, P. Blattner, H. P. Herzig and R. Dändliker, "*Heterodyne optical near-field measurements*", Nanoscale Optics, EOS topical meetings digests series Proc., **25**, p. 52-53, Engelberg, Switzerland, 2000.

B) A. Nesci, P. Blattner, H. P. Herzig and R. Dändliker, "*Heterodyne measurements of the optical near-field close to gratings*", 6th International Conference on Near-Field Optics and Related Techniques, Proc., p. 62, Enschede, The Netherlands, 2000.

C) A. Nesci, R. Dändliker and H. P. Herzig, "*Quantitative amplitude and phase measurement by use of a heterodyne scanning near-field optical microscope*", Opt. Lett., **26**, p. 208-210, 2001.

D) A. Nesci, M. Salt, R. Dändliker and H. P. Herzig, "*Optical near-field phase singularities produced by microstructures*", SPIE’s Annual Meeting 2001 Symposium, SPIE Proc., **4456**, p. 68-77, San Diego, USA, 2001.

E) A. Nesci, R. Dändliker, M. Salt and H. P. Herzig, "*Measuring amplitude and phase distribution of fields generated by gratings with sub-wavelength resolution*", *submitted to* Opt. Comm., 2002.

9 Acknowledgments

A thesis work requires important and personal efforts as well as obstinacy. Successful accomplishment cannot be achieved without helpful discussions and advice from different people, even if they are not directly related to your work domain. Therefore, I would like to express my gratitude to those who helped me during these last four years.

First of all, I wish to thank my thesis advisor, Prof. *René Dändliker*. He was the principal help for this work. He supervised and helped me throughout my PhD. I had the opportunity to benefit from his enormous knowledge in optics in particular and in physics in general. I am very grateful for his advice and especially to have believed in me during a difficult period of non-results. I thank him very much for his time (even on Sundays) spent for the precise, rigorous and detailed correction of my manuscript, without missing a single comma.

The other members of my thesis jury are gratefully acknowledged for accepting the correction of my manuscript during their precious time. Thank you to Prof. *Niek van Hulst*, from The Netherlands and to *Daniel Courjon* from France. Thank you also to the other thesis examiner, Prof. Hans Peter Herzig, who always was open to interesting discussions.

I would like to express my thanks to *Peter Blattner* who started this project as a post-doc and supervised me during the my first two years. He taught me the ropes of SNOM theory and of rigorous diffraction for the simulation of light-microstructure interaction.

Martin Salt was the second post-doc supervisor of the two last years. I thank him for his discussions and advice. He also helped me for the fiber probe simulations with MAFIA4. I am sorry for disturbing him with corrections of the different papers and of the thesis, especially for my English.

My thanks goes also to *Yves Salvadé* for initiating me in heterodyne interferometry. His help was essential in the good understanding of this technique. He also gave me a hand in the realization of the scanning/acquisition software in LabVIEW.

I would like to give thanks to *Marcel Groccia*, who helped me with the electronics in general, and especially for the realization of the photodetector (better than commercial ones). Thank you very much also for all the interesting discussions during the convivial lunches at the cafeteria.

Etienne Rochat and *Karim Haroud* gave me a hand in fiber handling, such as cleaving and welding. I thank them both for their general advice in fibers.

Special thanks to *Yves-Alain Peter, Silke Traut and Olivier Ripoll* who shared my office during these last four years. A convivial environment in the office is important for good work. Thanks also to Olivier for his help with Matlab.

I acknowledge *Luciana Vaccaro* for her discussions in SNOM and also during lunch at the cafeteria.

I am also grateful to *Christoph Weiteneder, Silke Traut, Irène Philippoussis and Philippe Nussbaum* for grating fabrication.

I wish to thank Prof. *Goudonnet's group* from Dijon for their advice as PSTM specialists and specially to *Yvon Lacroûte* who fabricated the excellent fiber probes.

Thanks to all other, former and present, *members* of the Applied Optics group for the pleasant atmosphere and also to the administrative staff of the institute of Microtechnology for their kindness.

Such a project also requires a lot of money for its realization. I would like therefore to acknowledge the *Swiss National Science Foundation* which supported this work financially.

In the end, I wish to thank particularly my *parents* and all my family who have always believed in me. They supported me through all my studies and have always helped me to take the right decisions. Thank you for having contributed totally the achievement of my scientific dreams.

Finally I dedicate this thesis to my wife *Cynthia*, who has been sharing my life for many years. She always encouraged me during my PhD, especially during the critical periods. She always pushed me forward. I thank her for her patience and her constant optimism.

10 References

[1] M. A. Paesler and P. J. Moyer, "*Near-field optics: Theory, Instrumentation and Applications*", ch.1, Wiley & Sons, New York, USA, 1996.

[2] J. M. Vigoureux and D. Courjon, "*Detection of nonradiative fields in light of the Heisenberg uncertainty principle and the Rayleigh criterion*", Appl. Opt., **31**, p.3170-3177, 1992.

[3] G. Binnig, H. Rohrer, C. Gerber and E. Weibel, "*Surface studies by scanning tunneling microscopy*", Phys. Rev. Lett., **49**, p.57-61, 1982.

[4] G. Binnig, C.F. Quate and C. Gerber, "*Atomic Force Microscope*", Phys. Rev. Lett., **56**, p.930-933, 1986.

[5] U. Dürig, D. W. Pohl and F. Rohner, "*Near-Field optical-scanning microscopy*", J. Appl. Phys., **59**, p.3318-3327, 1986.

[6] D. W. Pohl, W. Denk and M. Lanz, "*Optical stethoscopy: Image recording with resolution*", Appl. Phys. Lett., **44**, p.651-653, 1984.

[7] D. W. Pohl, *"Optical near-field scanning microscope"*, United States patent 4604520, Switzerland, 1986.

[8] H. Heinzelmann and D. W. Pohl, "*Scanning near-field optical microscopy*", Appl. Phys. A, **59**, p.89-101, 1994.

[9] R. Dändliker, "*Les lasers, principe et fonctionnement*", ch.1, presses polytechniques romandes, Lausanne, Switzerland, 1982.

[10] E. Zimmermann, "*Signal processing for optical phase detection*", Thesis, ch.3, University of Neuchâtel, Switzerland, 1997.

[11] J.-F. Willemin, "*Interférométrie hétérodyne de speckles: application à la mesure de vibrations mécaniques microscopiques*", Thesis, ch.2 and 3, University of Neuchâtel, Switzerland, 1984.

[12] A. Yariv, "*Optical Electronics*", ch.11, Holt-Saunders Ed., New York, USA, 1985.

[13] J.-F. Willemin and R. Dändliker, "*Heterodyne interferometer for submicroscopic vibration measurements in the inner ear*", J. Acoust. Soc. Am., **83**, p.787-795, 1988.

[14] E. Zimmermann, R. Dändliker and J.-F. Willemin, "*Full-dynamic phase demodulator for heterodyne interferometric vibration measurement*", vibration measurements by laser techniques, SPIE Proc., **2868**, p.488-499, Ancona, Italy, 1996.

[15] B. E. A. Saleh and M. C. Teich, "*Fundamentals of photonics*", ch.22, J. Wiley & Sons, New York, USA, 1991.

[16] R. Dändliker, "*Heterodyne holographic interferometry*", in Progress in Optics, E. Wolf, ch.1, North-Holland Ed., Amsterdam, The Netherlands, 1980.

[17] M. Vaez-Iravani and R. Toledo-Crow, "*Phase contrast and amplitude pseudoheterodyne interference near field scanning optical microscopy*", Appl. Phys. Lett., **62**, p.1044-1046, 1993.

[18] H. Masuda *et al.*, "*Development of heterodyne photon scanning tunneling microscope*", International workshop on interferometry, ICO Proc., p.141-142, Wako, Japan, 1996.

[19] A. Nesci, P. Blattner, H. P. Herzig and R. Dändliker, "*Heterodyne optical near-field measurements*", Nanoscale Optics, EOS topical meetings digests series Proc., **25**, p.52-53, Engelberg, Switzerland, 2000.

[20] M. L. M. Balistreri, J. P. Korterik, L. Kuipers and N. F. van Hulst, "*Local observations of phase singularities in optical fields in waveguide structures*", Phys. Rev. Lett., **85**, p.294-297, 2000.

[21] R. Hillenbrand and F. Keilmann, "*Complex Optical Constants on a Subwavelength Scale*", Phys. Rev. Lett., **85**, p.3029-3032, 2000.

[22] D. Charraut, C. Bainier, D. Courjon and C. Girard, "*Near-field phase measurement by Fourier analysis of the fringe pattern*", Pure Appl. Opt., **6**, p.491-502, 1997.

[23] J. N. Walford *et al.*, "*Three dimensional phase imaging with a scanning optical-fiber interferometer*", Appl. Opt., **38**, p.3508-3518, 1999.

[24] P. L. Phillips, J. C. Knight *et al.*, "*Direct measurement of optical phase in the near field*", Appl. Phys. Lett., **76**, p.541-543, 2000.

[25] K. Lieberman, A. Lewis *et al.*, "*Multifunctional, micropipette based force cantilevers for scanned probe microscopy*", Appl. Phys. Lett., **65**, p.648-650, 1994.

[26] R. C. Reddick, R. J. Warmack and T. L. Ferrell, "*New form of scanning optical microscopy*", Phys. Rev. B, **39**, p.767-770, 1989.

[27] R. C. Reddick *et al.*, "*Photon Scanning tunneling microscopy*", Rev. Sci. Instrum., **61**, p.3669-3677, 1990.

[28] D. Courjon, K. Sarayeddine and M. Spajer, "*Scanning tunneling optical microscopy*", Opt. Comm., **71**, p.23-28, 1989.

[29] M. Paesler *et al.*, "*Analytical photon scanning tunneling microscopy (surface topography and stresses)*", Phys. Rev. B, **42**, p.6750-5, 1990.

[30] N. F. van Hulst, N. P. de Boer and B. Bölger, "*An evanescent-field optical microscope*", J. of Microscopy, **163**, p.117-130, 1991.

[31] N. F. van Hulst, F. B. Segerink and B. Bölger, "*High resolution imaging of dielectric surfaces with an evanescent field optical microscope*", Opt. Comm., **87**, p.212-217, 1992.

[32] D. Courjon and D. W. Pohl, *"Scanning near-field optical microscope"*, European patent EP 0 593 835 B1, France, 1994.

[33] J. N. Israelachvili, "*Intermolecular and surface forces*", ch.11, Academic press, London, United Kingdom, 1991.

[34] N. F. van Hulst, M. H. P. Moers and B. Bölger, "*Near-field optical microscopy in transmission and reflection modes in combination with force microscopy*", J. of Microscopy, **171**, p.95-105, 1993.

[35] M. H. P. Moers, R. G. Tack, N. F. van Hulst and B. Bölger, "*Photon scanning tunneling microscope in combination with force microscope*", J. Appl. Phys., **75**, p.1254-1257, 1994.

[36] J. C. Weeber, "*Diffraction en champ proche optique. Analyse des images de microscopie à effet tunnel photonique*", Thesis, ch.6, University of Burgundy, Dijon, France, 1996.

[37] made by Y. Lacroûte in University of Burgundy, Laboratory of Physics, Dijon, France.

[38] *"MAFIA 4"*, written by T. Weiland, Users Guides, CST GmbH, www.cst.de, Darmstadt, Germany.

[39] M. Clemens *et al.*, "*The electromagnetic simulation software package MAFIA 4*", International Conference on Computational Electromagnetics and its Applications, Publising House of Electron. Ind. , IEEE Proc., p.565-568, Bejing, China, 1999.

[40] D. Lide, "*CRC Handbook of Chemistry and Physics*", ch.12, CRC press LLC, Boca Raton, USA, 1999.

[41] G. S. Agarwal, "*Subwavelength resolution using evanescent waves*", Pure Appl. Opt. A, **7**, p.1143-1149, 1998.

[42] F. S. Crawford, "*Waves*", ch.4, Berkeley Physics Course, McGraw-Hill Book Company, Newton, USA, 1968.

[43] M. Born and E. Wolf, "*Principles of Optics, Electromagnetic theory of propagation, interference and diffraction of light*", ch.1, Cambridge university press, Cambridge, United Kingdom, 1980.

[44] R. D. Guenther, "*Modern optics*", ch.3, J. Wiley & Sons, New York, USA, 1990.

[45] D. Axelrod, E. H. Hellen and R. M. Fullbright, "*Total internal reflection fluorescence*", in in Topics in Fluorescence Spectroscopy, ch.7, J.Lakowicz, Plenum Press, New York, USA, 1992.

[46] F. de Fornel, "*Les ondes évanescentes en optique et en optoélectronique*", ch.1, Eyrolles Ed., Paris, France, 1998.

[47] L. Salomon, F. de Fornel and J. P. Goudonnet, "*Sample-tip coupling efficiencies of the photon-scanning tunneling microscope*", J. Opt. Soc. Am. A, **8**, p.2009-2015, 1991.

[48] L. Salomon, "*Etude théorique et expérimentale de la profondeur de pénétration du champ frustré dans un microscope à effet tunnel photonique*", J. Optics, **23**, p.49-55, 1992.

[49] M. L. M. Balistreri *et al.*, "*Photon scanning tunneling optical microscopy with a three-dimensional multiheight imaging mode*", Appl. Phys. Lett., **77**, p.4092-4094, 2000.

[50] S. Davy, M. Spajer and D. Courjon, "*Influence of the water layer on the shear force damping in near-field microscopy*", Appl. Phys. Lett., **73**, p.2594-2596, 1998.

[51] L. Vaccaro, "*Local probe microscopy on lipid membranes: near field optical imaging and shear force studies*", Thesis, ch.4, EPFL, Lausanne, 2000.

[52] A. J. Meixner *et al.*, "*Direct measurement of standing evanescent waves with a photon-scanning tunneling microscope*", Appl. Opt., **33**, p.7995-8000, 1994.

[53] A. Nesci, R. Dändliker and H. P. Herzig, "*Quantitative amplitude and phase measurement by use of a heterodyne scanning near-field optical microscope*", Opt. Lett., **26**, p.208-210, 2001.

[54] A. Nesci, P. Blattner, H. P. Herzig and R. Dändliker, "*Heterodyne measurements of the optical near-field close to gratings*", 6th International Conference on Near-Field Optics and Related Techniques, Proc., p.62, Enschede, The Netherlands, 2000.

[55] A. Nesci, M. Salt, R. Dändliker and H. P. Herzig, "*Optical near-field phase singularities produced by microstructures*", SPIE's Annual Meeting 2001 Symposium, SPIE Proc., **4456**, p.68-77, San Diego, USA, 2001.

[56] H. F. Talbot, "*Facts relating to Optical Science*", Phil. Mag., **9**, p.401-407, 1836.

[57] M. V. Berry and S. Klein, "*Integer, fractional and fractal Talbot effects*", J. Mod. Opt., **43**, p.2139-2164, 1996.

[58] R. Petit, "*Electromagnetic theory of grating*", ch.1, Springer-Verlag, Berlin, Germany, 1980.

[59] E. G. Loewen and E. Popov, "*Diffraction grating and applications.*", ch.2, M. Dekker Inc., New York, USA, 1997.

[60] N. W. Ashcroft and N. D. Mermin, "*Solid state Physics*", ch.6, Saunders college, Orlando, USA, 1976.

[61] E. Wolf and J. T. Foley, "*Do evanescent waves contribute to the far field?*", Opt. Lett., **23**, p.16-18, 1998.

[62] P. Blattner, H. P. Herzig and R. Dändliker, "*Scanning near-field optical microscopy: transfer function and resolution limit*", Opt. Comm., **155**, p.245-50, 1998.

[63] S. I. Bozhevolnyi, B. Vohnsen and E. A. Bozhevolnaya, "*Transfer function in collection scanning near-field optical microscopy*", Opt. Comm., **172**, p.171-179, 1999.

[64] J. Turunen, "*Diffraction Theory of Microrelief Gratings*", in Micro-optics, elements, systems and applications, H.P. Herzig, Taylor & Francis, Inst. of Microtechnology, University of Neuchâtel, Switzerland, 1997.

[65] P. Blattner, "*Light field emerging from periodic optical microstructures*", Thesis, ch.3, University of Neuchâtel, Switzerland, 1999.

[66] J.-C. Weeber, F. de Fornel and J. P. Goudonnet, "*Numerical study of the tip-sample interaction in the photon scanning tunneling microscope*", Opt. Comm., **126**, p.285-292, 1996.

[67] J. W. Goodman, "*Introduction to Fourier optics*", ch.4, McGraw-Hill, New York, USA, 1996.

[68] I. I. Smolyaninov and C. Davis, "*Apparent superresolution in near-field optical imaging of periodic gratings*", Opt. Lett., **23**, p.1346-1347, 1998.

[69] J. F. Nye and M. V. Berry, "*Dislocations in wave trains*", Proc. R. Soc. London A, p.165-190, 1974.

[70] P. Blattner, "*Light field emerging from periodic optical microstructures*", Thesis, ch.5, University of Neuchâtel, Switzerland, 1999.

[71] R. Dändliker, P. Blattner, C. Rockstuhl and H. P. Herzig, "*Phase singularities generated by optical microstructures: Theory and experimental results*", Singular optics (optical vortices): fundamentals and applications, SPIE Proc., **4403**, p.257-262, Crimea, Ukraine, 2000.

[72] J. F. Nye, "*Natural focusing and fine structure of light, caustics and wave dislocations*", ch.5, Inst. of Physics Publishing, London, United Kingdom, 1999.

[73] P. Blattner and R. Dändliker, "*High resolution far-field measurements of optical microstructures*", Nanoscale Optics, EOS topical meetings digests series Proc., **25**, p.68-69, Engelberg, Switzerland, 2000.